2016-05-01

Automatic Dependent Surveillance-Broadcast for Detect and Avoid on Small Unmanned Aircraft

Matthew Owen Duffield
Brigham Young University

Automatic Dependent Surveillance-Broadcast for Detect and Avoid on Small Unmanned Aircraft

Matthew Owen Duffield

A thesis submitted to the faculty of
Brigham Young University
in partial fulfillment of the requirements for the degree of

Master of Science

Timothy W. McLain, Chair
Randal W. Beard
S. Andrew Ning

Department of Mechanical Engineering

Brigham Young University

May 2016

ABSTRACT

Automatic Dependent Surveillance-Broadcast
for Detect and Avoid on Small
Unmanned Aircraft

Matthew Owen Duffield
Department of Mechanical Engineering, BYU
Master of Science

Small unmanned aircraft systems (UAS) are rapidly gaining popularity. As the excitement surrounding small UAS has grown, the Federal Aviation Administration (FAA) has repeatedly stated that UAS must be capable of detecting and avoiding manned and unmanned aircraft. In developing detect-and-avoid (DAA) technology, one of the key challenges is identifying a suitable sensor. Automatic Dependent Surveillance-Broadcast (ADS-B) has gained much attention in both the research and consumer sectors as a promising solution. While ADS-B has many positive characteristics, further analysis is necessary to determine if it is suitable as a DAA sensor in environments with high-density small UAS operations.

To further the understanding of ADS-B, we present a characterization of ADS-B measurement error that is derived from FAA regulations. Additionally, we analyze ADS-B by examining its strengths and weaknesses from the perspective of DAA on small UAS. To demonstrate the need and method for estimation of ADS-B measurements, we compare four dynamic filters for accuracy and computational speed. The result of the comparison is a recommendation for the best filter for ADS-B estimation. We then demonstrate this filter by estimating ADS-B measurements that have been recorded from the National Airspace System (NAS). We also present a novel long-range, convex optimization-based path planner for ADS-B-equipped small UAS in the presence of intruder aircraft. This optimizer is tested using a twelve-state simulation of the ownship and intruders.

We also consider the effectiveness of ADS-B in high-density airspace. To do this we present a novel derivation of the probability of interference for ADS-B based on the number of transmitting aircraft. We then use this probability to document the need for limited transmit range for ADS-B on small UAS. We further leverage the probability of interference for ADS-B, by creating a tool that can be used to analyze self-separation threshold (SST) and well clear (WC) definitions based on ADS-B bandwidth limitations. This tool is then demonstrated by evaluating current SST and WC definitions and making regulations recommendations based on the analysis. Coupling this tool with minimum detection range equations, we make a recommendation for well clear for small UAS in ADS-B congested airspace. Overall these contributions expand the understanding of ADS-B as a DAA sensor, provide viable solutions for known and previously unknown ADS-B challenges, and advance the state of the art for small UAS.

Keywords: ADS-B, Automatic Dependent Surveillance-Broadcast, unmanned aircraft systems, UAS, UAV, detect and avoid, sense and avoid

ACKNOWLEDGMENTS

I would like to thank those who have helped and supported me through out my research and graduate studies. Dr. McLain, my advisor, has been very willing to review and discuss my research during my time in the MAGICC Lab. On many occasions he has made himself available for meetings to help me push my thesis along. Dr. Beard and Dr. Ning have also been very open with their time to discuss my research plans and progress. All of the members of my committee have been an example of diligent, careful research. This example has provided great direction throughout the course of my graduate studies. Additionally I am grateful to the Center for Unmanned Aircraft Systems (C-UAS) and its participants for the resources to fund this project.

My fellow students in the MAGICC Lab have been supportive as I have collaborated with them on my project. Laith Sahawneh and Jared Wikle have worked with me on the Detect and Avoid project and have been very willing to discuss my research plans and provide feedback on my results. It is important to note that part of the closest point of approach work in Section 6.1.4 and the minimum detection range formulations in Section 6.2 are the work of Jared Wikle. It is with his permission that I have applied his developments. Ultimately every member of the MAGICC Lab has been instrumental in the success of this project as they have provided feedback and encouragement. I appreciate their willingness to offer their time and expertise to discuss and illuminate various aspects of my project.

I am grateful to my brother, my parents, and my wife. Luke, my brother, has been willing to impart his experience and wisdom in pursing a graduate degree in mechanical engineering at BYU. He has provided prospective and encouragement through out my research. In many ways he paved an excellent path which I could follow. My parents, Mike and Joan, have always provided encouragement for my education. I am grateful to them for their foresight to instill in me the importance of education and for their dedication and love that has supported me as I pursue that education. They taught me invaluable principles of hard work, determination, and curiosity. Their confidence in me has pushed me to strive for my best. My wife, Kasey, has been ever willing

to listen as I shared my research successes and challenges. She has been amazingly supportive in managing many of the day-to-day demands of our family, all the while working towards her degree. Her devoted support and love has made my success possible, meaningful, and joyful.

TABLE OF CONTENTS

LIST OF TABLES

LIST OF FIGURES

NOMENCLATURE

Acronyms

ACAS-X	Airborne Collision Avoidance System X
ADS-B	Automatic Dependent Surveillance-Broadcast
ADS-R	Automatic Dependent Surveillance-Rebroadcast
Alt	Altitude
ATC	Air Traffic Control
CAT	Collision Avoidance Threshold
C-UAS	Center for Unmanned Aircraft Systems
DAA	Detect and Avoid
ELOS	Equivalent Level of Safety
EPU	Estimated Position Uncertainty
ES	Extended Squitter
FAA	Federal Aviation Administration
FIS-B	Flight Information System-Broadcast
GBT	Ground-Based Transceiver
GPS	Global Positioning System
HMD	Horizontal Miss Distance
ICAO	International Civil Aviation Administration
IMM	Interacting Multiple Models
JOCA	Jointly Optimal Collision Avoidance
KF-CJ	Kalman Filter-Constant-Jerk
KF-NCV	Kalman Filter-Nearly-Constant-Velocity
LTE	Long-Term Evolution
LTV	Limiting Tracking Variable
MAGICC	Multiple Agent Intelligent Coordination and Control
MDW	Chicago Midway Airport
MSO	Message Start Opportunity
MSR	Message Success Rate
NACp	Navigation Accuracy Category for Position
NACv	Navigation Accuracy Category for Velocity
NAS	National Airspace System
NIC	Navigational Integrity Category
NMAC	Near-Mid-Air Collision
NOTAM	Notice to Airmen
ORD	Chicago O'Hare International Airport
Pe	Position East
PF	Particle Filter
Pn	Position North
RMS	Root Mean Square
SARP	Sense and Avoid Science and Research Panel
SBAS	Satellite-Based Augementation System
SDA	System Design Assurance
SDK	Software Development Kit

SIL	Source Integrity Level
SSR	Secondary Surveillance Radar
SST	Self-Separation Threshold
SWaP	Size, Weight, and Power
TCAS	Traffic Collision and Avoidance System
TDMA	Time Division Multiple Access
TIS-B	Traffic Information System-Broadcast
TLOS	Time to Loss of Separation
UAS	Unmanned Aircraft System
UAT	Universal Access Transceiver
UL	Uncompensated Latency
USD	United States Dollar
UTM	UAS Traffic Management
Ve	Velocity East
VFR	Visual Flight Rules
Vn	Velocity North
WAAS	Wide Area Augmentation System
WC	Well Clear

CHAPTER 1. INTRODUCTION

1.1 Motivation

The number of applications of unmanned aircraft systems (UAS) is growing at a significant pace. Consequently the need for UAS in the National Airspace System is compounding at a similar rate. Governmental institutions are increasingly adopting UAS to perform tasks such as weather research, search and rescue, wildlife surveillance, law enforcement, wildfire monitoring, and military training. A report compiled by the US Department of Transportation on UAS service demands estimates that by the year 2035 there will be approximately 70,000 UAS operated by federal, state, and local departments and agencies [2]. This number excludes commercial and hobbyist operations. In the private sector, the ever growing number of UAS applications includes a wide variety of industries and tasks ranging from smoke stack inspection to cinematography to crop dusting to oil exploration to news and traffic reporting. To fill this public and private demand for UAS operation, a vast number of companies continue to invest in, and build around, UAS technology. The demand for UAS operations is manifest by the hundreds petitions to allow UAS operations under Section 333 of the FAA Modernization and Reform Act of 2012 [3].

While UAS operations have increased as a result of the Section 333 exemptions approved since September of 2014, the overall realized benefit of UAS operations is still a small fraction of the demand. Additionally Section 333 exemptions are not a long-term solution to supporting UAS in the National Airspace System. In laying the foundation for a long-term solution for UAS in the NAS, the Federal Aviation Administration (FAA) has mandated that UAS be capable of an equivalent level of safety (ELOS) to the see-and-avoid mandate for manned aircraft [4, 5]. As a result, similar to a pilot's ability to visually scan the surrounding airspace for possible intruding aircraft and take action to avoid a collision, a UAS must be capable of monitoring and avoiding other manned or unmanned aircraft with which it may collide. This mandate has come to be known as detect and avoid (DAA).

As a result of the large number of potential UAS applications, the rapidly developing DAA capability on UAS, and the expected integration of UAS into the NAS, future NAS conditions will include high-volume UAS operations. Numerous logistics companies such as Amazon, UPS, and DHL have announced plans to use UAS to deliver packages. Several restaurants and bakeries have indicated that they plan to use UAS to provide rapid delivery to their customers. Considering the wide array of other potential UAS applications, it is likely that there may be hundreds, or even thousands, of small UAS operating over highly populated areas. Such a high volume of UAS presents a new and unique air traffic control (ATC) challenge. Current ATC definitions of safe speeds and separation distances between aircraft are based on manned aircraft characteristics, which are much larger, fly much faster, and operate at higher altitudes than small UAS. To ensure safe and efficient UAS operation, DAA capability must be capable of handling high-density UAS operations. Ultimately integrating the anticipated high volume of small UAS into the NAS is a challenging aspect of both DAA and ATC development.

1.2 Background

The goal of DAA is to ensure that UAS are able to avoid other manned and unmanned aircraft. This very broad definition can be broken down into two different levels: self-separation assurance and collision avoidance. In self-separation assurance the objective is to remain well clear of other aircraft. Well clear is a term used in FAA-defined visual flight rules (VFR) regulations, and it is a qualitatively-defined safe, comfortable distance from other aircraft [5]. Pilots flying under VFR regulations determine their own well clear distance for each encounter with another aircraft. To maintain self-separation, aircraft make small, gradual path adjustments well in advance of a collision. In the event that an intruder penetrates the well clear volume of an ownship, it is referred to as a conflict, or in other words an unsafe, but non-catastrophic encounter. In a collision avoidance scenario, on the other hand, a near-mid-air collision (NMAC) is imminent, and the goal is to rapidly and aggressively avoid the collision. A collision is typically, although not officially, defined as two aircraft being within 200 ft in altitude and 500 ft horizontally [6]. Should two aircraft fail to maintain at least this much distance between them it is referred to as a collision and is a serious event.

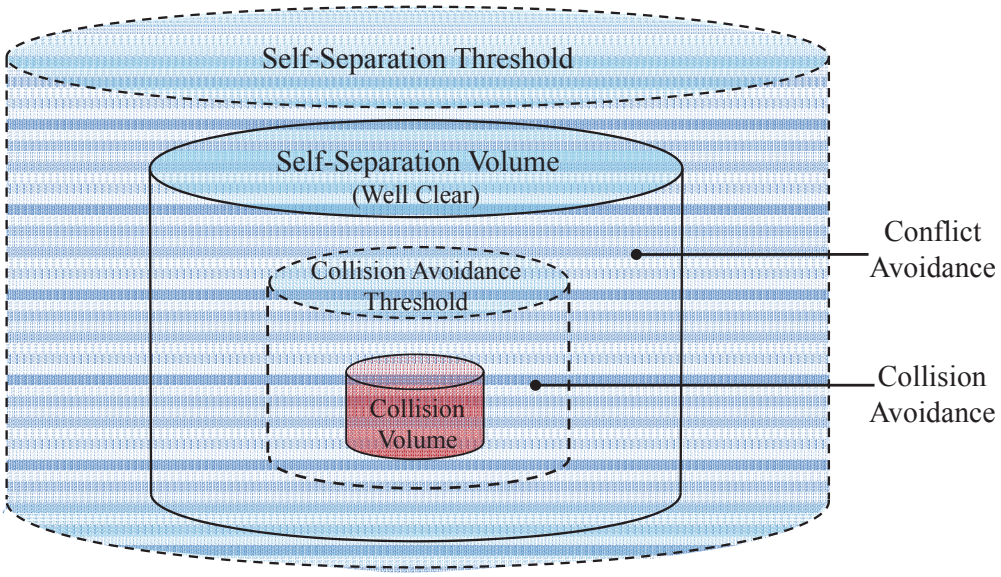

Figure 1.1: DAA volumes that indicate DAA levels.

Figure 1.1 shows the DAA volumes graphically. The figure is not drawn to scale, but it does show the relationship between the self-separation, or well clear, volume and the collision volume. Also Figure 1.1 shows the self-separation threshold and collision avoidance threshold. These thresholds are the point at which the ownship begins to maneuver to maintain the well clear or collision volume respectively. In other words, an aircraft is not considered to be an intruder until it crosses the self-separation threshold (SST). When the aircraft does cross the SST, then the ownship begins to maneuver to maintain well clear (WC). Similarly, an intruder is not considered to be a threat until it crosses the collision avoidance threshold (CAT). Once it crosses the CAT, the ownship begins to maneuver to prevent the intruder from entering the collision volume of the ownship. This set of volumes and thresholds creates an important framework for determining sensor requirements, collision prediction methods, and collision avoidance ability.

To allow UAS to successfully achieve an ELOS to manned aircraft operations, UAS must be capable of maintaining well clear from all other aircraft in a similar way to that of manned aircraft. By emphasizing self-separation and constantly maintaining well clear from other aircraft, the ability and probability of a UAS preventing collisions increases dramatically. Focusing exclusively on collision avoidance, results in the UAS having to make aggressive, reactive, and last-minute maneuvers. In many cases these types of maneuvers push the computational, and physical limits of

the UAS. By focusing on self-separation, there is a much longer reaction time available for a UAS to identify an intruder, predict its path, and execute an avoidance maneuver. This results in a much higher level of safety.

Focusing on self-separation highlights several challenges associated with maintaining well clear. The sensor capabilities necessary to detect intruders at long ranges can be difficult to achieve on board a small UAS. Long-range path planning can pose a significant computational challenge, especially for a power and space-limited small UAS. Finally autonomous self-separation capability requires that there be a quantitative definition of well clear, which does not currently exist. Each of these challenges poses an exciting opportunity in the development of small UAS.

1.2.1 Current Sensor Technologies

For small UAS, those weighing less than fifty-five pounds, the algorithms and hardware necessary for DAA make up a notable portion of the size, weight, and power (SWaP) resources available. Traditional aircraft-detecting sensors are designed for manned aircraft that offer a significantly larger payload and much more powerful electrical system than those available on small UAS. Scaling traditional sensors down to small UAS sizes often requires compromises in range, accuracy, field of view, or processing speed. Such compromises can reduce the overall capability of the DAA system and consequently decrease the assurance of collision prevention. Significant efforts have gone into overcoming these challenges and identifying sensors suitable for DAA on small UAS.

Radar

Radar is one sensor that is widely used for air-to-air detection in manned aircraft. One of the primary strengths of radar is the ability to detect all objects regardless of cooperative sensor equipage or functionality. Recent radar developments have resulted systems suitable for large UAS [7]. This is evidenced by recent testing of radar-based DAA systems on the General Atomics MQ-9 Predator B. In applying radar to small UAS, SWaP constraints impose restrictions on the hardware that result in significant trade offs between radar range, bearing accuracy, and field of view. At a set transmit power, improving the range requires a narrower beam, which also improves

the bearing accuracy. Narrowing the beam, however, reduces the field of view and consequently requires additional antennas or a method to steer the beam. Demonstrated hardware that falls within the SWaP limitations of small UAS is not currently suited to support a feasible set of range, bearing accuracy, and field of view requirements [8–10].

Cameras

Cameras are another set of candidate sensors for DAA on small UAS. A significant amount of development has gone into image processing methods and overall systems to make them suitable for small UAS. Similar to radar, vision-based intruder detection methods do not require cooperative communication from intruders. Flight testing of visual methods has achieved intruder detection at 0.54 nmi from a small UAS [11], and ground-based testing has resulted in detection up 4.3 nmi [12]. Several challenges still face visual methods in relation to DAA including range, range accuracy, and weather conditions. The flight tested range of 0.54 nmi is promising, but not sufficient to provide enough avoidance time for high-speed intruders. Even with sufficient range, visual methods inherently have low range accuracy. Adverse weather conditions such as fog, clouds, precipitation, and sun glare can reduce overall visibility and significantly limit visual intruder detection. Overall recent developments have improved visual intruder detection, but such methods are not yet suitable for DAA implementation on small UAS.

ADS-B

Automatic Dependent Surveillance-Broadcast (ADS-B) is a cooperative sensor that is a promising option for DAA on small UAS. It has been demonstrated in small UAS flight testing to have an omni-directional range of 20 nmi [13], and due to the fact that the cooperative information is shared over radio waves it is relatively unaffected by adverse weather conditions. An omni-directional antenna and low power requirements for both transponder and receiver hardware contribute to the promising characteristics of ADS-B. Two major drawbacks of ADS-B are its fundamentally cooperative nature and its bandwidth limitations. The cooperative aspect of ADS-B requires widespread adoption of ADS-B technology to ensure detect and avoid reliability. While the Federal Aviation Administration does not yet require all aircraft to be equipped with ADS-B

transponders, the 2020 mandate requiring all aircraft in A, B, C, and some E class airspace to equip with ADS-B [14] is a significant step. Due to the fact that ADS-B messages are sent using a finite-capacity multiple access protocol, there is limited bandwidth. If too many aircraft are transmitting on ADS-B at the same time, then the transmissions may interfere with each other and become unusable. While this is not likely to be a concern for current NAS conditions, a future environment with many small UAS operating in close proximity may encounter bandwidth limitations. Even with its cooperative nature and possible bandwidth limitations, ADS-B is a promising sensor for self-separation DAA efforts.

1.2.2 Long-Range Planning Methods

Long-range path planning is fundamental for UAS to maintain self-separation. It allows for the long-range intruder information available through ADS-B, or another long-range sensor, to inform the waypoint path of a UAS. This combination of intruder detection and planning essentially provides the UAS with the foresight necessary to plan a conflict/collision free path rather than reactively adjust its path to avoid encounters. UAS path planning methods such as rapidly-exploring random trees (RRT) and tree branching algorithms have been demonstrated in relatively short-range environments with great success [15, 16]. In long-range applications, however, the computational resources necessary to plan a long-range path with these methods grows exponentially. Jointly optimal collision avoidance (JOCA) is another proposed path planning method for DAA on UAS [17]. While it is capable of planning a path that maintains self-separation, it only plans 30 s into the future. In the case of a small UAS moving at approximately 20 kt, this may only be approximately 1000 ft or less than a sixth of a mile. Thus JOCA does not take advantage of the long-range information available through ADS-B. The method does have a way to increase the look ahead distance, but it comes with exponentially increasing cost. Airborne Collision Avoidance System X (ACAS-X) is an FAA-funded research effort to provide conflict/collision avoidance logic for manned aircraft [18]. The research will likely result in a system that can be modified for small UAS, but this system is not ready for implementation. Some estimates indicate that it will be approximately ten years before the system is fully implemented and operational.

Optimization-based paths can be formulated to achieve long-range path planning with limited computational resources. Foo, Knutzon, Oliver, and Winer presented a three-dimensional path

planning optimizer for UAS using a particle swarm algorithm [19]. This method used a hybrid objective function that had user-defined weights for fuel minimization and threat avoidance. While the work demonstrated avoidance of ground threats, it did not address dynamic aerial threats. Additionally, it relied on an operator to select the final weighting distribution between fuel minimization and threat avoidance.

A linear programming, three-dimensional path planning method for UAS is presented by Chen, Han, and Zhao [20]. This research is particularly applicable to the separation assurance path planning challenge. It presented a linear programming method to plan a path in the presence of dynamic obstacles. The reported execution time is suitable for real-time applications. The overall goal of the algorithm was to find the optimal path along which a UAS could pursue a moving target and avoid obstacles. This work is relevant to separation assurance path planning, but the goal and scenario are different. The scenarios demonstrated in the article have distances on the order of 7.5 nmi. This is significantly less than the 15-50 nmi range expected in a separation scenario. Ultimately, it is likely that Chen, Han, and Zhao's work could be transformed into a separation assurance path planning method, but further work is necessary to accomplish and demonstrate this.

Optimization-based path planning has been successfully demonstrated, but an opportunity remains to apply it to a self-separation DAA context. An optimization-based path planner that takes advantage of long-range ADS-B information, mitigates imperfect knowledge of intruder positions, and accounts for the time-varying nature of intruder positions is necessary.

1.2.3 The Need To Define Well Clear

To allow UAS to autonomously maintain self-separation, a quantitative well clear definition is necessary. In addition to a well clear definition, a quantitative self-separation threshold is also necessary to identify the point at which the ownship should initiate a maneuver to maintain self-separation.

SST and WC Metrics

Typically SST and WC definitions are defined in one of three ways: the distance between the ownship and intruder, the time to collision or closest point of approach, or a combination of both distance and time metrics. Joint definitions are the most common. The distance-based definitions are quite intuitive. Each aircraft is surrounded by a safety volume, typically a cylinder, such that any intruder that penetrates that volume is said to have lost self-separation. The time-based definitions are also intuitive, but more difficult to visualize. For each intruder, the ownship calculates a time metric, such as the time to closest point of approach. If this time is less than a given threshold then self-separation, or well clear, has been lost. The primary metrics that can be used to define SST and WC are relative range r, distance to closest point of approach d_{CPA}, time to closest point of approach t_{CPA}, time to collision τ, modified time to collision τ_{DMOD}, and time to entry point t_{ep} [21]. The first three metrics, r, d_{CPA}, and t_{CPA}, are intuitive. They indicate the norm of the relative position vector, the distance to the closest point of approach, and the time to the closest point of approach respectively. τ is calculated by dividing the range by the range rate. For aircraft that are on a collision course, this metric accurately indicates the time to collision, but for aircraft that will only approach each other without colliding, τ can become numerically unstable as the aircraft approach their closest point. At that instant the range rate is zero, and τ becomes infinite. τ_{DMOD} seeks to mitigate the numerical instability in τ by introducing a distance buffer. Essentially τ_{DMOD} serves as a numerically stable approximation of t_{CPA}. t_{ep} is the time to entry point. This is the time to loss of horizontal separation. All of these time metrics are similar in that they strive to estimate when two aircraft will collide. Thus values of each of the metrics are typically similar, especially for long-range targets. For a given self-separation assurance method, the metrics are selected based preference and the information available from the sensors.

Proposed SST and WC Definitions

Recent literature contains several proposed self-separation threshold and well clear definitions [22–26]. Many of these definitions are similar. Typically they are based on a combination of a time and a distance metric. For the SST, if the time metric is less than approximately 90 s or the distance metric is approximately 4000 ft and the altitude separation is less than approximately

500 ft, the ownship begins to maneuver. For WC, if the time metric is less than approximately 35 s or the distance metric is approximately 4000 ft and the altitude separation is less than approximately 500 ft, then self-separation has been lost. Many time-based SST and WC definitions include a horizontal miss distance (HMD) filter. This filter calculates the closest point of approach for the intruder aircraft. If the closest point of approach is larger than some threshold, then SST/WC are maintained even if the time-based metric drops below its threshold. Johnson, Mueller, and Santiago detail and compare several of these different definitions [22].

Johnson, Mueller, and Santiago also provide a valuable insight into the application of SST and WC definitions by using recorded VFR traffic and simulated UAS to map time-based well clear definitions onto a distance-from-ownship plot [22]. Such a mapping demonstrates the range at which the time-based SST and WC definitions are enacted. Interestingly in the majority of cases, the time-based definition was reached long before the distance-based definition. The result of their simulations led them to recommend that DAA sensors be capable of sensing intruders 12 nmi in front of and 5 nmi behind an ownship to achieve the proposed SST and WC definitions. This contribution is particularly valuable to small UAS in that the majority of their simulations were conducted below 6000 ft.

Currently, one of the primary small-UAS-suitable sensors capable of the recommended range is ADS-B. While ADS-B does offer a promising sensor for self-separation, it is susceptible to frequency congestion. In environments with a large number of ADS-B-equipped aircraft it is possible for transmitted information to interfere with other ADS-B transmissions. The development and validation efforts used to define the currently proposed SST and WC definitions do not take into account congestion of the ADS-B frequency. It is necessary to investigate the effects of ADS-B congestion on the self-separation threshold and well clear definitions and propose a well clear definition for small UAS in congested ADS-B airspace.

1.3 Contributions

Because of the many excellent characteristics of ADS-B, the approaching 2020 mandate for ADS-B, and the opportunity to explore and vet ADS-B as a DAA sensor beyond the current literature, this thesis will focus on challenges and opportunities associated with ADS-B-equipped small UAS. The primary contributions of this thesis include:

- A statistical characterization and model of ADS-B measurement error and a trade study of the viability of ADS-B as a DAA sensor.
- A comparison of three estimators to estimate both simulated and recorded ADS-B measurements and a recommendation for the most suitable one.
- An optimization-based path planner for self-separation assurance in the presences of dynamic obstacles given ADS-B as a sensor.
- An analysis of the bandwidth limitations of ADS-B.
- An analysis of current proposed SST and WC definitions based on ADS-B bandwidth limitations and the associated maximum achievable SST and WC thresholds.
- A recommendation for well clear for small UAS in congested ADS-B airspace with slow-moving manned aircraft.

1.4 Document Outline

The research presented in this thesis is organized into five major chapters beyond the introduction. Chapter 2 provides an explanation of the characteristics of ADS-B, a derivation of an ADS-B error characterization, and a discussion of the strengths and limitations of ADS-B as a DAA sensor. Next, Chapter 3 contains a comparison of a Kalman filter, particle filter, and interacting multiple models filter for estimating ADS-B measurements. Chapter 4 presents the formulation, implementation, and results of an optimization-based path planner for self-separation assurance. Chapter 5 provides an analysis of the bandwidth limitations of ADS-B and their impact on the visibility of intruders via ADS-B. Chapter 6 explores the viability of proposed SST and WC definitions for high-density, ADS-B-equipped small UAS operations. It also makes a well clear recommendation for small UAS. Finally Chapter 7 summarizes the presented work, details policy recommendations based on the presented work, and identifies opportunities to extend the research.

CHAPTER 2. ADS-B CHARACTERISTICS AND ERROR

ADS-B is rapidly becoming a major tool in the air traffic management system. In 2010 the FAA issued a final rule for the implementation of ADS-B on manned aircraft [14]. This ruling mandated ADS-B Out in key parts of the NAS. The FAA Modernization and Reform Act of 2012 further directed the FAA to make plans for the adoption of ADS-B In technology [3]. As a result of the level of adoption and capability of ADS-B technology, ADS-B is an attractive sensor for detect and avoid efforts on UAS.

This chapter provides a description of ADS-B and the associated regulations as they relate to detect and avoid on small UAS. A statistical characterization of ADS-B error and drop out is derived from the current FAA regulations. Further, we explore the capability of ADS-B as a DAA sensor by examining key characteristics and limitations of ADS-B.

2.1 Characteristics and Regulations of ADS-B

ADS-B is a cooperative sensor that supports the exchange of a wide variety of information over long ranges. Information that is typically exchanged includes aircraft state information, state error estimates, aircraft identifiers, and aircraft operating indicators. This exchange occurs approximately once per second [27]. To exchange this information, two sets of hardware are necessary, ADS-B In and ADS-B Out. As the names suggest, ADS-B In allows for information to be received, and ADS-B Out supports the broadcasting of information. The hardware performing these two functions can be sold separately or as a single unit. In addition to the In or Out capability of ADS-B hardware, ADS-B transmissions can occur over one of two different frequencies, 1090 MHz or 978 MHz [14]. The 1090 MHz Extended Squitter (ES) frequency is an internationally recognized ADS-B frequency. It is intended that this frequency be used for most commercial and high-performance aircraft. The 1090 MHz frequency is the same frequency used for current Mode S transmissions. The Extended Squitter designation indicates a message packet that is much

longer than the standard Mode S packet. This allows for the transmission of much more information than what is exchanged via secondary surveillance radar (SSR). The 978 MHz Universal Access Transceiver (UAT) frequency is unique to United States airspace. It is primarily intended for private and low-altitude aircraft. ADS-B Out hardware is specific to one of these two frequencies. The airspace class in which an aircraft will operate dictates the required frequency. ADS-B In hardware also is specific to a particular frequency, but dual-link hardware that is capable of receiving transmissions on both frequencies is becoming increasingly available.

FAA regulations set forth in the 2010 Final Rule dictate most aspects of ADS-B operation. The message elements, airspace class, transmit power, latency, and error characteristics are all among the aspects of ADS-B that are regulated by the FAA. While these regulations do add complexity to the implementation and operation of an ADS-B system, they also provide a consistent basis upon which ADS-B can be evaluated for DAA on small UAS.

Table 2.1: Required set of message elements for ADS-B Out.

State Elements	Identification Elements	Error Elements	Other Elements
Latitude	Mode 3/A Transponder Code	NACp	Emitter Category
Longitude	Call Sign	NACv	Emergency Code
Barometric Altitude	IDENT	NIC	TCAS II Equipped
Geometric Altitude	ICAO 24-bit address	SDA	TCAS II Advisory
Velocity	Length and Width	SIL	ADS-B In Equipped

2.1.1 Message Element Requirements

The message elements exchanged by ADS-B transmissions provide a view of the transmitting aircraft's status. Table 2.1 shows a list of these elements that is arranged by functional category. The state elements transmitted are the latitude and longitude, barometric altitude, geometric altitude, and velocity. A certified position source must be used for latitude and longitude information. Typically a Satellite Based Augmentation System (SBAS), otherwise known as a Wide Area Augmentation System (WAAS) in the US, source is used. The barometric altitude is provided as the primary altitude as it is typically more accurate than the GPS-derived geometric

altitude. The velocity transmitted is a ground reference velocity in knots and can be given as a combination of north and east velocity or speed and heading depending on whether the aircraft is on the ground or airborne [5] [28]. If the aircraft is airborne, then the vertical velocity is given in feet per minute. On the other hand if the aircraft is on the ground, then the length and width of the aircraft is given instead of the vertical velocity.

The identification information provided by ADS-B permits simple identification of the transmitting aircraft. While a detailed explanation of each of the identification elements listed in Table 2.1 is beyond the scope of this thesis, it is useful to note that each of these elements provides a unique identifier for the aircraft.

The message elements detailing the error in the state information are also shown in Table 2.1. Navigation Accuracy Category for Position (NACp) is a value that correlates to an Estimated Position Uncertainty (EPU) bound. The EPU bound used is defined as the "radius of a circle, centered on the reported position, such that the probability of the actual position being outside the circle is 0.05." [28] The FAA requires that the NACp must be greater than 8 which corresponds to an EPU $<$ 303.8 ft [28] [5]. The Navigation Accuracy Category for Velocity (NACv) is similar in that it is a value that corresponds to a error bound on the transmitted velocity. This bound is a 95% bound in that there is less than 0.05 probability that the error between the true velocity and the transmitted velocity exceeds the NACv bound. The FAA requires the NACv value to be greater than or equal to 1 which corresponds to the transmitted velocity error being less than 19.4 kt. Navigation Integrity Category (NIC) is a value that corresponds to an integrity containment radius, R_c. It signifies the maximum position error such that the probability that no integrity alert is indicated is less than the Source Integrity Level (SIL). In other words this radius is the value where there is an SIL probability that the measurement has been identified as a low integrity (possibly erroneous) measurement. This value must be greater than 7 which corresponds to $R_c < 1215.2$ ft. The SIL probability assumes no avionics faults, and the FAA mandates that SIL=3 which corresponds to probability $\leq 1 \times 10^{-7}$ per sample or per hour. The distinction between a per sample or per hour probability is made in an ADS-B message field known as SILsupp. To account for errors due to avionics faults, the System Design Assurance (SDA) is a value that corresponds to the "...probability of an ADS-B system fault causing false or misleading information to be transmitted." [28] "The ADS-B system includes the ADS-B transmission equipment, ADS-B processing equipment, posi-

tion source, and any other equipment that processes the position data transmitted by the ADS-B system." [28] This information includes latitude, longitude, velocity, accuracy metrics, or integrity metrics. The FAA mandates that the SDA value be 2 which corresponds to a probability $\leq 1 \times 10^{-5}$ per flight hour [28] [5]. While both the SDA and the SIL report a probability of exceeding the NIC, it is important to note that the SIL assumes no avionics fault, but the SDA is the probability that an avionics fault is the cause of the reported error.

Elements in the fourth column, labeled as Other Elements, provide information concerning the operational status of the aircraft. The first field specifies the emitter category of the transmitting aircraft. The emitter category indicates the type of aircraft and gives some indication of aircraft weight, size, and maneuverability. The emergency code is the second item in the fourth column. This code indicates if there is an emergency on-board the transmitting aircraft such as a medical emergency, minimum fuel, unlawful interference, or a downed aircraft. Such information is useful both to identify aircraft that need special attention from air traffic control services and for search and rescue efforts in a downed aircraft situation. The last three fields listed in column four of Table 2.1 indicate the equipage and activity of cooperative sensors. The third field indicates whether Traffic Collision Avoidance System (TCAS) is operable on the transmitting aircraft. Field four extends this and reports whether a traffic advisory or resolution advisory is in effect. The fifth field indicates whether the transmitting aircraft has ADS-B In capability.

2.1.2 Airspace and Power Requirements

The 2010 Final Rule on ADS-B mandated that by the year 2020 all aircraft in A, B, C, and some E class airspace be equipped with ADS-B Out. There is no mandate for ADS-B In. The FAA further mandated airspace where each of the two frequencies of ADS-B Out, 1090 MHz and 978 MHz, can be used. Class A airspace requires 1090 MHz. Where ADS-B is required below 18,000 ft, either 1090 MHz or 978 MHz is acceptable. Both B and C class airspace require ADS-B. ADS-B is also required within 30 nmi of a Class B airport reaching from the surface up to 10,000 ft mean sea level (MSL). Above B and C class airspace extending up to 10,000 ft MSL, ADS-B is required. E class airspace requires ADS-B from 10,000 ft MSL and above with the exception of the surface to 2,500 ft above ground level (AGL). In other words, if 0 ft AGL is above 10,000 ft MSL then there is a 2,500 ft region above ground level where ADS-B is not required. Finally ADS-B

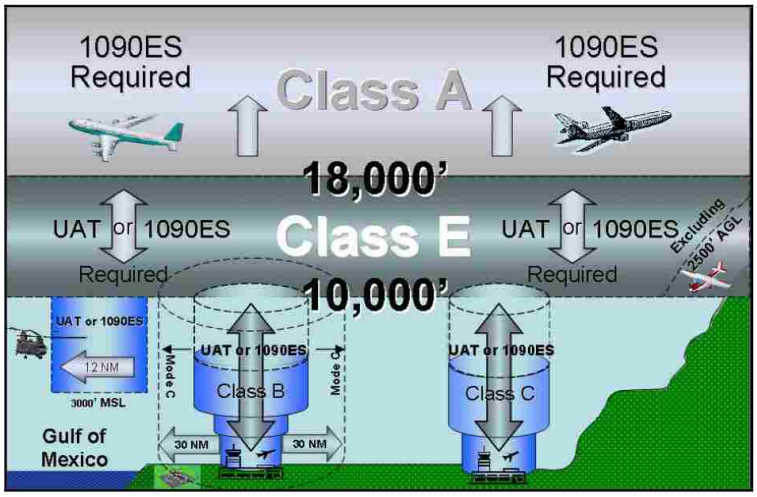

Figure 2.1: Airspace where ADS-B Out is required [1].

is required above 3,000 ft MSL over the Gulf of Mexico within 12 nmi of the coast of the United States [5]. Figure 2.1 summarizes the airspace requirements for ADS-B Out [1].

The range of ADS-B transmissions is largely dependent on the transmit power of the ADS-B transponder. FAA regulations mandate different levels of transmit power for 1090 MHz and 978 MHz. For the 978 MHz frequency, there are three transmit power levels. Each level corresponds to a minimum transmit power and consequently a transmission range. The 1090 MHz frequency also has three levels which correspond to a minimum transmit power and range. While transmit ranges vary as a result of frequency congestion, antenna differences, and other external factors, estimated, air-to-air ranges for the 978 MHz frequency extend from 10 nmi to 90 nmi and for the 1090 MHz frequency estimated ranges extend from 10 nmi to 140 nmi [28] [29]. Air-to-ground or ground-to-air transmissions have a much longer anticipated range as a result of more sensitive receivers and more powerful transponders that are available for ground-based equipment.

2.1.3 Supplementary ADS-B Transmissions

Due to the fact that ADS-B exchanges cooperative information over one of two possible frequencies, air-to-air ADS-B transmissions are supplemented by three additional transmissions from Ground Based Transceivers (GBT). The first, Automatic Dependent Surveillance-Rebroadcast (ADS-R), is a cross link between the 1090 MHz and 978 MHz frequency. Essentially the GBT receives ADS-B signals on one frequency and rebroadcasts that same signal on the other frequency.

This provides ADS-B In-equipped aircraft with visibility to all ADS-B Out-compliant aircraft regardless of transmission frequency. Second, Traffic Information Service-Broadcast (TIS-B) provides a more complete traffic picture by rebroadcasting radar-derived traffic over both ADS-B data links [30]. Current TIS-B relies on secondary surveillance radar to create a traffic picture. This means that only transponder equipped aircraft will be visible on TIS-B [27]. Also of note is that TIS-B and ADS-R are enabled by compliant ADS-B Out and are received by ADS-B In. Thus to receive TIS-B and ADS-R aircraft must be both ADS-B Out and In equipped [31]. Third, Flight Information Service-Broadcast (FIS-B) provides weather and flight information (i.e., NOTAMs) to 978 MHz UAT equipped aircraft. This broadcast is available to all ADS-B In 978 MHz UAT aircraft. There is no requirement for ADS-B Out [31]. These transmissions will help to create a more complete traffic picture for small UAS and manned aircraft that may be ADS-B-equipped on only one frequency.

2.2 Error Characterization

In addition to the error metrics outlined in Table 2.1, ADS-B is subject to several additional sources of error namely latency error, resolution error, and message success rate (MSR) error. These additional sources of error, along with those previously defined in Table 2.1, play a role in defining an error characterization of ADS-B.

Due to processing needs, data latency is inherent in the ADS-B system. This latency falls into two categories. Total latency is the time from measurement to transmission and must be less than 2.0 s. Of those 2.0 s, all but 0.6 s must be compensated for by the ownship. In compensating for latency the transmitting aircraft must "[extrapolate] the geometric position to the time of message transmission." [5] The uncompensated 0.6 s of the total latency is referred to as uncompensated latency (UL) [5]. It is the uncompensated latency that is the primary source of latency error.

Resolution error results from encoding state information into an ADS-B message where the information is represented by discrete bits. Table 2.2 shows the resolution limits for an ADS-B message [28].

ADS-B regulations require that receivers are capable of supporting a given message success rate. For messages on the 978 MHz frequency this is 10%, and for messages on 1090 MHz, this

Table 2.2: Resolution limits for ADS-B message information.

Message Element	Resolution
Latitude	0.5 deg
Longitude	0.5 deg
Barometric Altitude	25 ft
Geometric Altitude	45 ft
Horizontal Velocity	1 knot
Vertical Velocity	64 feet/min

is approximately 15%. These success rates imply that one out of every 10 or 3 out of every 20 messages is not received, thus resulting in message success rate error.

The NACp, NACv, NIC, SIL, SDA, latency error, resolution error, and MSR error provide a basis from which to derive an error characterization to model ADS-B. The error characterization presented here will focus on state information and will use statistical methods to model the error of the actual measurements rather than the accuracy of individual bits. Given the NACp and NACv, the horizontal position and velocity can be modeled as a Rayleigh random process. From the Rayleigh process, the 95% bound on both the position and velocity error can be used to derive the variance for a Gauss-Markov process with zero-mean Gaussian noise for the north and east position and velocity [32] [33]. For the derivation of the variation of a Gauss-Markov process in accordance with FAA requirements we use, NACp=303.8 ft and NACv=19.4 kt. Let X and Y each represent a Gauss-Markov process with zero-mean Gaussian noise such that $X \sim N(0,\sigma^2)$ and $Y \sim N(0,\sigma^2)$. R is a Rayleigh distributed variable such that $R \sim Rayleigh(\sigma)$ where σ is derived from the 95% NAC bound. The NAC variance is considered generally for both NACp and NACv. Thus it can be shown that the variance is given by

$$\sigma^2 = \frac{-NAC^2}{2\ln(0.05)}. \tag{2.1}$$

Substituting values for NACp and NACv respectively results in $\sigma_x = \sigma_y = 124$ ft and $\sigma_{vx} = \sigma_{vy} = 8$ kt. From this analysis, it is determined that the horizontal north and east position error can be modeled as a zero-mean Gaussian distribution with a standard deviation of 124 ft and the north

and east velocity can be modeled as a zero-mean Gaussian distribution with a standard deviation of 8 kt.

Correlation of errors in the position are accounted for by the Gauss-Markov model. Since the error correlation is a result of the correlation of GPS errors, the time constant used to simulate GPS errors is used to simulate ADS-B error correlation also. In the following equation, T_s =1 s and k_{GPS} =1/1100 s [16]. Using position north, X, as an example

$$X[n+1] = e^{-k_{GPS}T_s}X[n] + N(0,\sigma_u^2).$$

It is necessary to calculate σ_u^2 from the variance of X. Mohleji and Wang put forth a method to do this [32]. Given that T_c is the time of correlation,

$$\sigma_u^2 = (1-e^{-2/T_c})\sigma_x^2.$$

In the particular case of ADS-B where $\sigma_x = \sigma_y = 124$ ft and $T_c = 1100$ s, $\sigma_u = \sqrt{(1-e^{-2/1100})\sigma_x^2} =$ 5.28 ft. This is the variance of the Gaussian noise necessary for the zero-mean Gaussian random variable in the Gauss-Markov process with standard deviation $\sigma = 124$ ft.

FAA regulations require that ADS-B pressure altitude reporting equipment must report an altitude that is within 125 ft of the true altitude with 95% confidence [5] [34]. Let the pressure altitude error, A_{pres}, be a zero-mean Gaussian random variable such that $A_{pres} \sim N(0,\sigma_{Apres}^2)$. It can then be shown that $\sigma_{Apres} = 75.9$ ft. For geometric altitude reports the error is typically less than 147.6 ft with 95% certainty [28] [29]. Assuming that the geometric altitude error, A_{geo}, is a zero-mean Gaussian random variable such that $A_{geo} \sim N(0,\sigma_{Ageo}^2)$, it can be shown that $\sigma_{Ageo} = 89.8$ ft. In addition to the noise of the pressure reporting sensors, the encoding of barometric altitude information has a resolution of 25 ft and geometric altitude information has a resolution of 45 ft. This resolution introduces some additional error.

The error in the ADS-B reported vertical velocity varies with increasing vertical rate. For vertical rates between $\pm$500 ft/min the vertical rate tolerance is $\pm$46 ft/min. For rates outside that range, the tolerance is 5% of the vertical rate [35] [36]. Given the assumption that these tolerances are 95% bounds, it can be shown that the standard deviation of the climb rate is 27.96 ft/min for

vertical rates of $\pm$500 ft/min. Additionally the vertical rate error is effected by the resolution of the ADS-B message encoding which is 64 ft/min.

The loss of valid ADS-B signal can be modeled using SIL, SDA, and MSR error. FAA regulations stipulate that position measurements outside the reported NIC can only be transmitted once per 10^7 transmissions. The SDA requirements permit values outside the NIC with a probability of 10^{-5}. MSR error requirements allow for a 10% or 15% message loss rate. These probabilities of erroneous or lost messages provide a method with which to model ADS-B signal dropout.

The error characteristics detailed above make it possible to model the error in ADS-B reported horizontal position, altitude, horizontal velocity, and vertical velocity. This results in a method capable of simulating ADS-B messages. It also provides a basis for estimating ADS-B messages and developing conflict detection, collision detection, separation assurance and collision avoidance methods.

2.3 ADS-B as a DAA Sensor

The characteristics and requirements of ADS-B make it a capable sensor for DAA on small UAS in the National Airspace System. One key aspect of ADS-B that makes it feasible for use on small UAS is the availability of ADS-B receivers that meet the (SWaP) constraints of a small UAS. The Clarity ADS-B receiver provides a dual-link ADS-B receiver that is 2.5 in by 2.5 in by 1.5 in, weighs 0.344 lbs, and consumes 2.4 Watts of power. Freeflight Systems has also recently introduced the RANGR RXD which is a dual-link ADS-B receiver. While slightly larger at 5 in by 5.75 in by 1.7 in, it still weighs less than one pound and consumes approximately 2.4 Watts of power. These hardware options both provide a suitable ADS-B In solution for small UAS.

Another key advantage of ADS-B is the long range at which information is available. While there is a significant amount of variation in the range of ADS-B signals, the shortest expected range is 10 nmi. Flight tests of ADS-B units suitable for small UAS have demonstrated reliable ranges of up to 80 nmi [13]. Additionally the long range of ADS-B is advantageous in that the quality of information transmitted over ADS-B does not degrade with range. Thus the accuracy of ADS-B is not dependent on the size, power, or range of the transmitter and receiver units. This is a significant advantage over radar and optical sensors, and makes conflict detection and separation assurance path planning possible at long ranges.

Table 2.3: Time to loss of separation and time to collision for ADS-B given 10 nmi detection range.

Intruders			Ownship					
			RQ-11B Raven (43 kn)		ScanEagle (80 kn)		DJI Phantom 1 (19 kn)	
	Model	Max. Speed (kn)	Head-on Scenario	Over-Taking Scenario	Head-on Scenario	Over-Taking Scenario	Head-on Scenario	Over-Taking Scenario
	F-35	1042	31.0/32.3	33.2/34.6	30.0/32.2	34.3/35.7	31.7/33.0	32.8/34.2
	Boeing 747	533	58.4/60.9	66.8/69.6	54.9/57.2	71.2/74.2	60.9/63.5	65.3/68.0
	Cessna TTX	240	119.3/124.3	160.2/166.9	105.5/109.9	188.0/195.9	130.1/135.5	151.8/158.1
	Cessna SkyHawk	126	198.9/207.1	346.0/360.4	163.2/170.0	508.8/530.0	230.7/240.3	308.9/321.8
	Scan -Eagle	80	274.6/286.0	665.4/693.1	211.0/219.8	1730.1/1802.0	339.2/353.3	540.7/563.1
	RQ-11B Raven	43	393.2/409.5	2471.5/2574.3	274.6/286.0	-	540.7/563.1	1330.8/1386.2

Time to Loss of Separation (s) / Time to Collision (s)

A compelling result of the long range availability of ADS-B messages is the time to loss of separation (TLOS) and time to collision (TC). Table 2.3 shows the TLOS and TC for head-on and over-taking scenarios given different intruder aircraft and various small UAS ownships. The detection range is set to the FAA required minimum of 10 nmi, and the separation distance is 0.66 nmi [23]. For this table a collision is defined as a violation of a 500 ft collision radius. The speeds listed are the maximum speeds for each aircraft. To identify a true worst-case scenario in the over-taking intruder configuration, the speed used for the ownship is a cruising speed rather than a maximum speed. The figure demonstrates the value of the long-range detection available through ADS-B. Even for a worst-case scenario where an F-35 type aircraft is flying directly at a small UAS, the minimum TLOS is 30.0 s. This provides a sufficient amount of time for the UAS to perform an avoidance maneuver.

ADS-B is a very capable sensor for DAA on small UAS, but it is not without limitations. One notable limitation of ADS-B is that it is a cooperative technology. This means that to have visibility of other aircraft they also must be equipped with ADS-B. Given the FAA mandate that only some aircraft need to be ADS-B compliant, there certainly will be aircraft in lower altitudes that are not ADS-B equipped. While these lower altitudes are prime locations for small UAS operations, the capability of ADS-B presented in this paper provides motivation to implement an ADS-B equipage requirement for all aircraft. An additional technology that could be used to account for uncooperative aircraft, birds, and ground based obstacles is ADS-B radar. This technology is essentially a phase modulated ADS-B signal that is used as a radar and traditional ADS-B transmission simultaneously [37]. This would allow for visibility of uncooperative intruders. The method does require additional processing of the ADS-B signal and some additional hardware, but it could be practical for UAS. While an in-depth discussion of this technology is outside the scope of this thesis, it is promising.

It is interesting to note that the current air traffic control (ATC) system is built on cooperative secondary surveillance radar (SSR) technology. Unlike conventional radar, SSR transmits an interrogation from a ground station. Any aircraft with a transponder that hears that interrogation replies with its call sign and altitude. Over several interrogations the position of the responding aircraft can be determined. Thus current ATC methods are cooperative, and the cooperative aspect of ADS-B is not a new challenge.

Another limitation of ADS-B is that it is heavily dependent on line-of-sight availability of GPS and ADS-B transmissions. Without GPS information, ADS-B transponders are unable to transmit usable position information. Air-to-air ADS-B transmissions also require line-of-sight visibility for reliable exchange of information. One demonstrated solution to the line-of-sight limitation is the use of satellite-based ADS-B repeaters. This system uses ADS-B transceivers on satellites to gather and re-transmit ADS-B signals. This system allows for over-the-horizon visibility of other aircraft and could be particularly valuable in mountainous or heavily contoured terrain.

Bandwidth constraints of ADS-B may also be a limitation. Due to the fact that all ADS-B Out-capable aircraft must transmit a message at least once per second on the same nominal frequency, the ADS-B protocol specifies a multiple access scheme. While the scheme is different for

the 978 MHz frequency and 1090 MHz frequency, all multiple access schemes have a finite number of transmitters that they can support. Particularly applicable to small UAS are the limitations of the time-division multiple access (TDMA) scheme used for the 978 MHz frequency. A more in-depth analysis of this TDMA scheme is included in Chapter 5, but bandwidth congestion is a potential limitation of ADS-B. Recommendations presented in Chapters 5 and 6 suggest modifications to current NAS regulations that can largely mitigate the effects of ADS-B frequency congestion for small UAS on the 978 MHz frequency.

The cost of ADS-B equipage may pose a limitation. Certified ADS-B Out hardware costs typically range from $1,500 to $25,000 USD. ADS-B In hardware costs range from $400 to $3,000 USD. While these costs are not necessarily prohibitive, they are significant especially for many of the small-to-medium-sized companies that plan to use UAS for commercial purposes. For ADS-B to be a fully viable, accessible technology, hardware costs need to decrease. As the FAA 2020 mandate approaches an increasing number of companies are producing ADS-B hardware, and the cost of hardware is trending downward.

Ultimately the message elements, airspace and range requirements, hardware availability, and error characteristics of ADS-B make it a viable sensor for detect and avoid on small UAS in the NAS. While there are limitations to ADS-B sensors, development of promising solutions is reducing the impact of those limitations. As a DAA sensor, ADS-B offers all the information necessary to detect conflicts, maintain self-separation, and detect and prevent collisions.

CHAPTER 3. ADS-B ESTIMATION

Estimation of ADS-B messages is capable of mitigating much of the error in the transmitted measurements. This chapter details the estimation and processing of ADS-B measurements. Included in the chapter is a comparison of a two Kalman filters, an interacting multiple models filter, and a particle filter to identify the most suitable filter to estimate ADS-B messages on-board a small UAS. The chapter also includes a discussion of the methods and challenges associated with estimating real ADS-B measurements recorded from air traffic in the NAS.

3.1 The Need for ADS-B Estimation

The primary goal of ADS-B estimation is to account for missed measurements that result from signal dropout or frequency congestion. Additionally, by filtering and estimating ADS-B measurements, it is possible to account for grossly erroneous measurements, smooth measurement noise that is typical of any real sensor, and estimate the transmitting aircraft state at a rate greater than the 1 Hz measurement rate [38]. Due to the fact that ADS-B messages contain an aircraft identifier such as the call sign or International Civil Aviation Organization (ICAO) address, there is no need for data association methods. This greatly simplifies the tracking task.

3.2 An ADS-B Estimator Comparison on Simulated Measurements

To identify the most suitable estimator for ADS-B measurements, this section contains a comparison of four filters: a nearly-constant-velocity Kalman filter, a constant-jerk Kalman filter, an interacting multiple models filter, and a particle filter. One characteristic of ADS-B messages that makes the estimation problem nontrivial is that aircraft do not necessarily follow linear dynamics. Small UAS, particularly multirotors, are very maneuverable and can fly in highly nonlinear ways. With perfect knowledge of the command inputs to the aircraft and well established models of aircraft dynamics, it would be possible to model the motion of the intruder aircraft exactly.

ADS-B, however, does not provide such information. Thus it is necessary to use approximate models of the aircraft motion to estimate the states of the aircraft such as the four filters listed above. Another aspect of ADS-B messages that makes estimation difficult is that the measurements are transmitted in limited-resolution bins. Thus the measurement error is not continuously distributed over a probability density function, but rather the measurement values are rounded into discrete values as shown in Chapter 2. This discretization and the possibility of high maneuverability complicates the estimation task. The goal of this section is to determine which estimator addresses the needs for ADS-B estimation while providing accurate estimates.

3.2.1 Key Estimator Characteristics

Several key estimator characteristics form a basis upon which to evaluate the estimators. In accordance with the need for ADS-B estimation, one of foremost key characteristics of an ADS-B estimator is the ability to overcome missed measurements. Thus a suitable estimator must be able to provided accurate estimates even when measurements are missed in one or more successive time steps. Two other important characteristics are the ability to reject gross errors and the degree to which the filter can smooth the measurements. Although unlikely, the SIL and SDA probabilities allow grossly erroneous ADS-B measurements to be transmitted. If the estimator is not robust to such gross errors the estimate will be compromised, and the filter may diverge. Due to the fact that the estimates will be used for conflict/collision prediction, the estimates need to be as smooth as possible. Noisy estimates will lead to false alarms and missed detections in the conflict/collision prediction algorithm. Due to the fact that the estimator will run on a computationally-limited small UAS, the computational run time of the estimator is significant.

To measure these key characteristics, we examine the root mean square (RMS) error in the estimate, the 95th percentile error in the estimate, the estimate error standard deviation, and the estimator run time. The RMS error and 95th percentile error indicate the accuracy of the estimate and its robustness to gross errors. The standard deviation of the error is a good indicator of the smoothness of the estimate, and the run time indicates the computational speed of the estimator. Additionally we plot the estimate, measurements, and truth data for each estimator to examine the estimates visually. These five metrics and the visual verification provide a basis for comparing the filters' ability to estimate ADS-B signals on small UAS.

3.2.2 Filter Implementations

Each filter was implemented in MATLAB. The process covariance for each filter was hand-tuned for the best aggregate performance over several data sets. The measurement covariance was taken from the error derivation presented in Chapter 2.

Kalman Filter Implementation

A Kalman filter is a linear, dynamic state estimator [16]. Given a linear state-space model of a system, knowledge of the accuracy of the model, and knowledge of the accuracy of incoming measurements, a Kalman filter can estimate the true states of the system. Using an initial estimate and estimate covariance, the Kalman filter first propagates the estimate into the future using the linear state-space model. It also updates the estimate covariance to reflect uncertainty in the predicted estimate. To do this it takes into account both the uncertainty of the previous estimate and the uncertainty in the state-space model representation of the true dynamics of the system. Once a measurement is received, the Kalman gain for that measurement is calculated taking into account to the uncertainty of the predicted estimate and the uncertainty in the measurement. With the Kalman gain and the measurement, the estimate and estimate covariance can be updated to create the state estimate for that time step. If no measurement is available for a given time step, the measurement update step can be omitted. If no measurement is available for an extended number of time steps, however, the estimate covariance grows larger and larger, and the estimate becomes less and less meaningful. Algorithm 1 outlines the Kalman filter equations and method for a one second cycle [16].

In Algorithm 1, $\hat{x}_k$ represents the state estimate at time step k, and the superscript $^-$ indicates that the estimate has not been updated with a measurement at the given time step. P_k represents the estimate covariance at time step k. Q is the uncertainty in the state-space model of the system represented by A and C. R is the measurement covariance, and z_k is the measurement at time step k.

In our comparison we implement a Kalman filter with a nearly-constant-velocity model and a Kalman filter with a constant-jerk model. The nearly-constant-velocity model (KF-NCV) is a six-state model that models the dynamics of a system that has constant velocity. For aircraft the

Algorithm 1 Kalman filter method for one second.

Initialize: $\hat{x}_{k-1} = x_0$
Initialize: $P_{k-1} = R$
Select estimate rate T_{out} that is less than or equal to the 1 Hz measurement rate
for $k = 1$ to $\frac{1}{T_{out}}$ **do**
    [Predict Step]
    $\hat{x}_k^- = A\hat{x}_{k-1}$
    $P_k^- = AP_{k-1}A^T + Q$
    if A valid measurement has been received **then**
        [Update Step]
        $K_k = P_k^- C^T (CP_k^- C^T + R)^{-1}$
        $\hat{x}_k = \hat{x}_k^- + K_k(z_k - C\hat{x}_k^-)$
        $P_k = (I - K_k C)P_k^-$
    end if
end for

assumption of constant velocity is not true. By adding a relatively large process covariance, the requirement of constant-velocity dynamics is relaxed, and the result is a nearly-constant-velocity model. The states in the KF-NCV are position north, position east, altitude, velocity north, velocity east, and climb rate.

The constant-jerk model Kalman filter (KF-CJ) is a twelve-state filter that models the dynamics of a system with constant jerk. Due to the fact that only the jerk is assumed to be constant, both the velocity and acceleration can vary. This allows the KF-CJ filter to model the dynamics of maneuvering targets without the need for a large process covariance [39]. The states of the filter are position north, position east, altitude, velocity north, velocity east, climb rate, acceleration north, acceleration east, vertical acceleration, jerk north, jerk east, and vertical jerk.

Interacting Multiple Models Filter Implementation

The interacting multiple models (IMM) filter is an estimator that is capable of modeling movement that is characterized by different dynamics at different times. It is essentially a bank of estimators running in parallel. Each estimator creates a state estimate of the target. Using the received measurement, the likelihood of each estimate is calculated. These likelihoods are then normalized into a weighting factor with which the estimates and covariances from all the filters are combined. At the next time step, each filter is initialized with the previous combined estimate and

covariance, and the process is repeated. Throughout a maneuver or change of dynamics, different estimates from the bank of filters can be weighted more or less heavily. In this way an IMM filter can account for many different sets of dynamics. Algorithm 2 shows the equations for a one second cycle of an IMM filter [40].

Algorithm 2 IMM filter method for one second.

Initialize: $\hat{x}_{k-1} = x_0$
Initialize: $P_{k-1} = R$
Initialize: $\mu_{k-1} = [.5, .25, .25]$
Select estimate rate T_{out} that is less than or equal to the 1 Hz measurement rate
Let $j = i =$ the number of models
[Model-Conditioned Reinitialization]
$\mu_k^{i-} = \sum_j \pi_{ji} \mu_{k-1}^j$
$\mu_{k-1}^{j|i} = \frac{\pi_{ji}\mu_{k-1}^j}{\mu_k^{i-}}$
$\bar{x}_{k-1}^{i-} = \sum_j \hat{x}_{k-1}^{j-} \mu_{k-1}^{j|i}$
$\bar{P}_{k-1}^{i-} = \sum_j [P_{k-1}^{j-} + (\bar{x}_{k-1}^{i-} - \hat{x}_{k-1}^{j-})(\bar{x}_{k-1}^{i-} - \hat{x}_{k-1}^{j-})^T] \mu_{k-1}^{j|i}$
[Model-Conditioned Filtering]
$\hat{x}_k^{i-} = A^i \hat{x}_{k-1}^{i-}$
$P_k^{i-} = A^i \bar{P}_{k-1}^{i-} (A^i)^T + Q^i$
if A valid measurement has been received **then**
    [Update Step]
    $\tilde{z}_k^i = z_k - C^i \hat{x}_k^{i-}$
    $S_k^i = C^i P_k^{i-} (C^i)^T + R$
    $K_k^i = P_k^{i-} (C^i)^T (S_k^i)^{-1}$
    $\hat{x}_k^i = \hat{x}_k^{i-} + K_k^i \tilde{z}_k^i$
    $P_k^i = P_k^{i-} - K_k^i S_k^i (K_k^i)^T$
    [Model Probability Update]
    $L_k^i = \mathcal{N}(\tilde{z}_k^i; 0, S_k^i)$
    $\mu_k^i = \frac{\mu_k^{i-} L_k^i}{\sum_j \mu_k^{j-} L_k^j}$
else
    $\mu_k^i = \mu_k^{i-}$
    $\hat{x}_k^i = \hat{x}_k^{i-}$
    $P_k^i = P_k^{i-}$
end if
[Estimate Fusion]
$\hat{x}_k = \sum_i \hat{x}_k^i \mu_k^i$
$P_k = \sum_i [P_k^i + (\hat{x}_k - \hat{x}_k^i)(\hat{x}_k - \hat{x}_k^i)^T] \mu_k^i$

In Algorithm 2, π_{ji} is the Markov transition likelihood between each of the models. μ_{k-1}^{j} is the probability of each model for the previous time step. The $^{-}$ superscript indicates that the variable has not been updated with the current measurement. The A, C, Q, R matrices are state space and error covariances, respectively, as indicated in the description of Algorithm 1.

Our implementation of an IMM filter contains a bank of three estimators. A nearly-constant-velocity Kalman filter accounts for straight and level flight. We also use two coordinated turn models, one with a turn rate of 45 $\frac{deg}{s}$ and one with a turn rate of -45 $\frac{deg}{s}$, to account for maneuvering targets [41]. The states in each of the filters are position north, position east, altitude, velocity north, velocity east, and climb rate. While this set of filters does not account for all possible types of maneuvers, a relatively large process covariance allows the IMM filter to adapt to track a wide array of intruder dynamics.

Particle Filter Implementation

A particle filter (PF) is a nonlinear filter that is capable of estimating highly nonlinear systems with nongaussian process and measurement convariances. The particle filter is fundamentally different from the Kalman filter in that it uses a set of particles to sample the estimate space and builds its estimate from the probability of each particle given the measurement [42]. With an initial state estimate and the probability density function of the error in the system model, the particle filter creates a set of particles that represent the estimate space. Each particle is then predicted into the future using state-space equations that model the system. It is important to note that this state-space model does not need to be linear. Using the received measurement and the probability density function of the measurements, the probability of each of the predicted particles given the measurement is calculated. This set of probabilities is normalized into a set of weights. The weighted particles are then resampled so as to concentrate the particles on the highest-probability estimates. The resampled particles then are combined to form the state estimate for that time step. These same resampled particles become the initial set of particles for the next time step. In this way the particle filter is capable of accounting for highly nonlinear motion with nongaussian process and measurement noise. A single iteration of the particle filter is given in Algorithm 3.

The notation used in Algorithm 3 is similar to that of Algorithms 1 and 2. $\bar{x}_k$ represents the set of m particles used in the filter.

Algorithm 3 Particle filter method for one second.

Initialize: $\hat{x}_{k-1} = x_0$
Initialize: $P_{k-1} = R$
Initialize: $\bar{x}_{k-1} = m$ samples of $\mathcal{N}(\hat{x}_{k-1}, P_{k-1})$
for $n = 1$ to m **do**
    [Predict Particles]
    $\bar{x}_k^{n-} = A\bar{x}_{k-1}^{n} + \mathcal{N}(0, Q)$
    $\tilde{z}_k^n = z_k - C\bar{x}_k^{n-}$
    $w^n = \mathcal{N}(\tilde{z}^n; 0, R)$
end for
if A valid measurement has been received **then**
    [Resample Particles]
    $w = \frac{w}{\sum_n w^n}$
    $\bar{x}_k = m$ samples of $\bar{x}^{n-}$ weighted by w
else
    $\bar{x}_k = \bar{x}_k^-$
end if
$\hat{x}_k = \frac{\sum_n \bar{x}_k}{m}$

In our implementation of the particle filter, we estimate position north, position east, altitude, velocity north, velocity east, and climb rate. To do this we use 250 particles. More particles would better sample the six-dimensional estimate space and significantly improve the estimates. A larger number of particles, however, results in a more computational demand. In predicting the particles forward in time, we used a constant-velocity state-space model. To create the state estimate for each time step, we use a simple average of all of the particles. When measurements are missed, we skip the resampling step and use the set of initial, predicted particles to create our state estimate. This set of initial, predicted particles is then used as the particles for the next time step.

3.2.3 Measurement Updates

The measurements used to update the estimator states are the position north, position east, altitude, and climb rate. In updating the states, the transmitted horizontal velocities are ignored as a result of transmission errors. Recorded ADS-B data sets from the NAS have revealed that on rare occasions the north and east velocities are transmitted in reverse order resulting in an apparent velocity that is perpendicular to the actual direction of travel of the transmitting aircraft. Updating the filters with only a subset of measurements mitigates this problem and results in equally accurate

estimates after a brief transient period of several measurements. To provide a better comparison of filters for the ultimate goal of estimating true ADS-B measurements, the filters described here are updated without horizontal velocities.

3.2.4 Measurement Gating

A set of measurement gates is necessary to account for message dropout and grossly erroneous measurements. If at a given time step there is no measurement, only the filter prediction occurs for each filter. The update step occurs only when there is a valid measurement. For the KF-CV, KF-CJ, and IMM filters a measurement is determined to be valid only if the innovation falls with in a 5 Mahalinobis distance bound [43]. Essentially the Mahalinobis distance bound ensures that the measurement is within 5 standard deviations from the estimate while taking into consideration the uncertainty of the measurement and estimate. Due to the fact that the PF does not compute an estimate covariance directly, the gating for gross errors is set to reject any measurement for which the associated particle likelihoods are all less than 10^{-200}. This effectually ignores measurements that are very far from the predicted particle locations. These gross-error-rejection methods are key in maintaining the integrity of the ADS-B estimates.

3.2.5 Comparison Results

To compare the KF-CV, KF-CJ, IMM, and PF estimators quantitatively and qualitatively, we used each one to estimate the same three data sets. From these data sets and the resulting sets of estimates, were were able to calculate the statistics for each of the key estimator characteristics. Additionally we plotted the estimates against the measurements and truth data for each estimator to provide a visual evaluation of the estimates.

The data sets used in the estimator comparison were derived from a twelve-state simulator of a fixed-wing UAS. To generate the truth data, the simulated UAS was set to fly a collision avoidance path through a city environment. This scenario was chosen so as to include a combination of straight and level flight and multiple maneuvers. During the course of this flight, we recorded the true states of the aircraft. Using the ADS-B simulator outlined in Chapter 2, the true states were transformed into a global coordinate frame and corrupted to simulate ADS-B measurements. We

then modified the simulated measurements to reflect the proper update rate of 1 Hz for ADS-B. This process was completed for all three of the data sets used in the comparison.

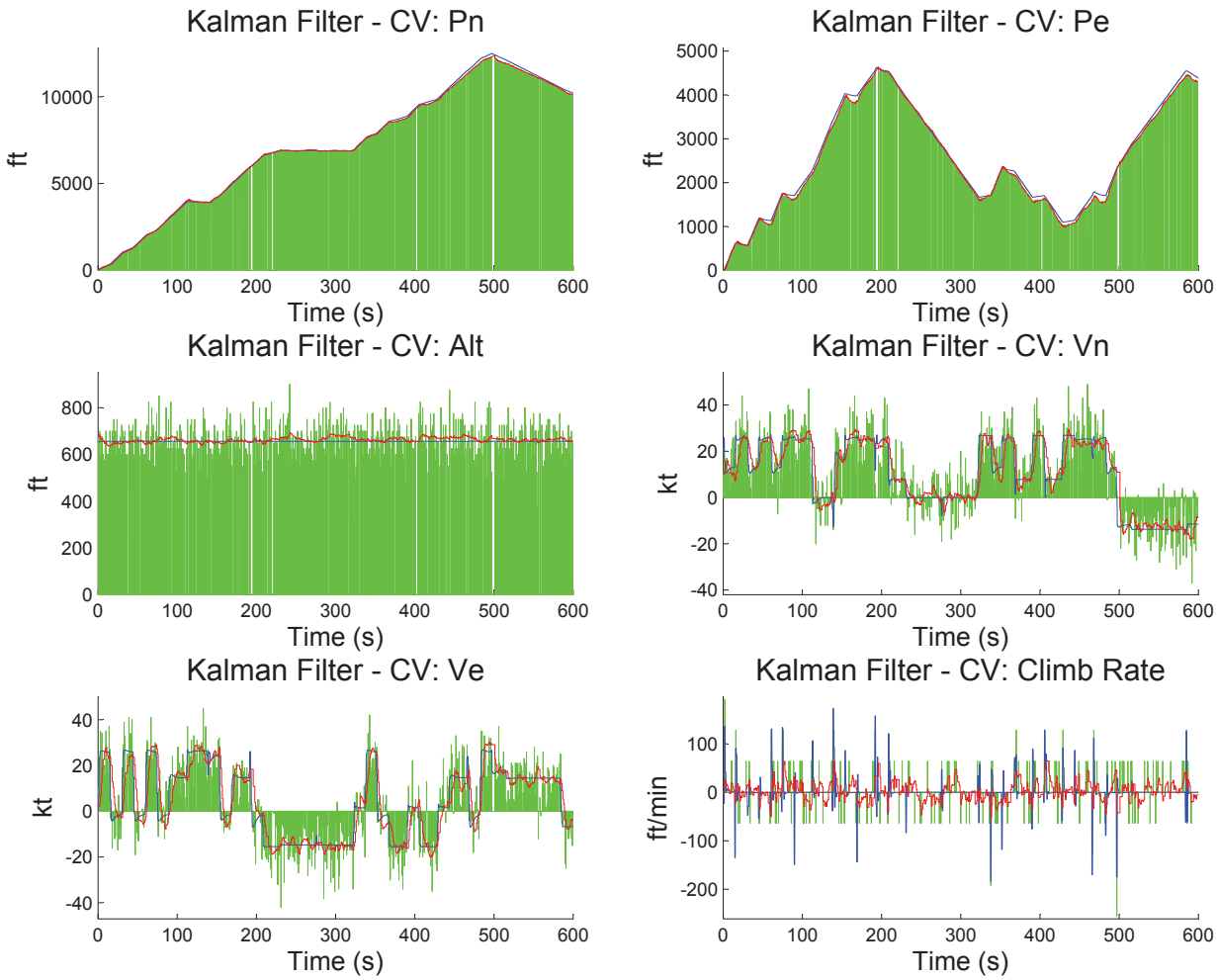

Figure 3.1: Performance of the nearly-constant-velocity Kalman filter for simulated ADS-B measurements.

Figure 3.1 shows the plotted estimate results from the nearly-constant-velocity Kalman filter. The red lines are the estimates. The blue lines are truth, and the green lines are the measurements. In all of the plots, the green lines fill in the area between the truth and the horizontal axis. This is indicative of two things. First it illustrates that fact that the estimator is running at 100 Hz and the measurements are only coming in at 1 Hz. Also it demonstrates that at some of the time steps the measurements are missed, and thus the measurement is all zeros.

From the plots in Figure 3.1, it is clear that the KF-NCV accurately estimates the truth data and significantly smooths the noise in all measurements. It is further significant to note, that even without velocity measurement updates, the velocity estimates are quite accurate especially considering the abrupt step changes seen in the both velocity north and velocity east.

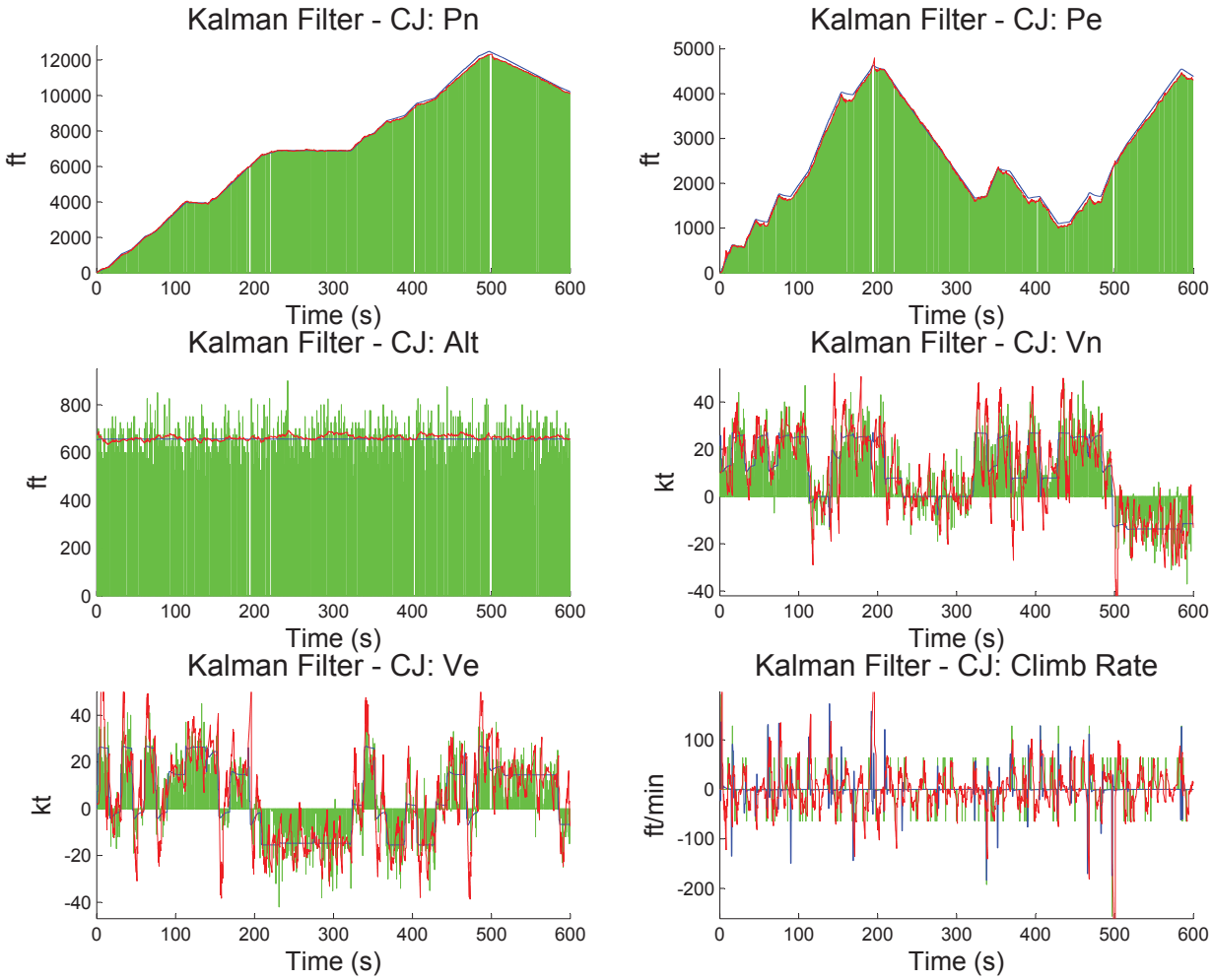

Figure 3.2: Performance of the constant-jerk Kalman filter for simulated ADS-B measurements.

Figure 3.2 demonstrates the performance of the constant-jerk Kalman filter for estimation of ADS-B measurements. The position north, position east, and altitude estimates in Figure 3.2 are very similar to those from the KF-NCV in Figure 3.1. Interestingly the velocity estimates from the KF-CJ are much noisier than those seen in Figure 3.1. This is a result of the constant-jerk model. Due to the fact that the model allows the velocity, acceleration, and, to some degree, the jerk to

change, the model is much less stable when there is no measurement. In the ADS-B scenario where measurements occur only at 1 Hz, there is approximately 1 second for the acceleration and jerk terms to alter the estimate. In terms of an estimator running at 100 Hz, this is a long time. Another important consideration in the noisiness of the velocity estimates is that since only the positions are used to estimate velocity, acceleration, and jerk, the position information is effectually differentiated three times. This will result in progressively noisier estimates for velocity, acceleration, and jerk. These two factors play a major role in the noisiness of the estimates for velocity north, velocity east, and climb rate.

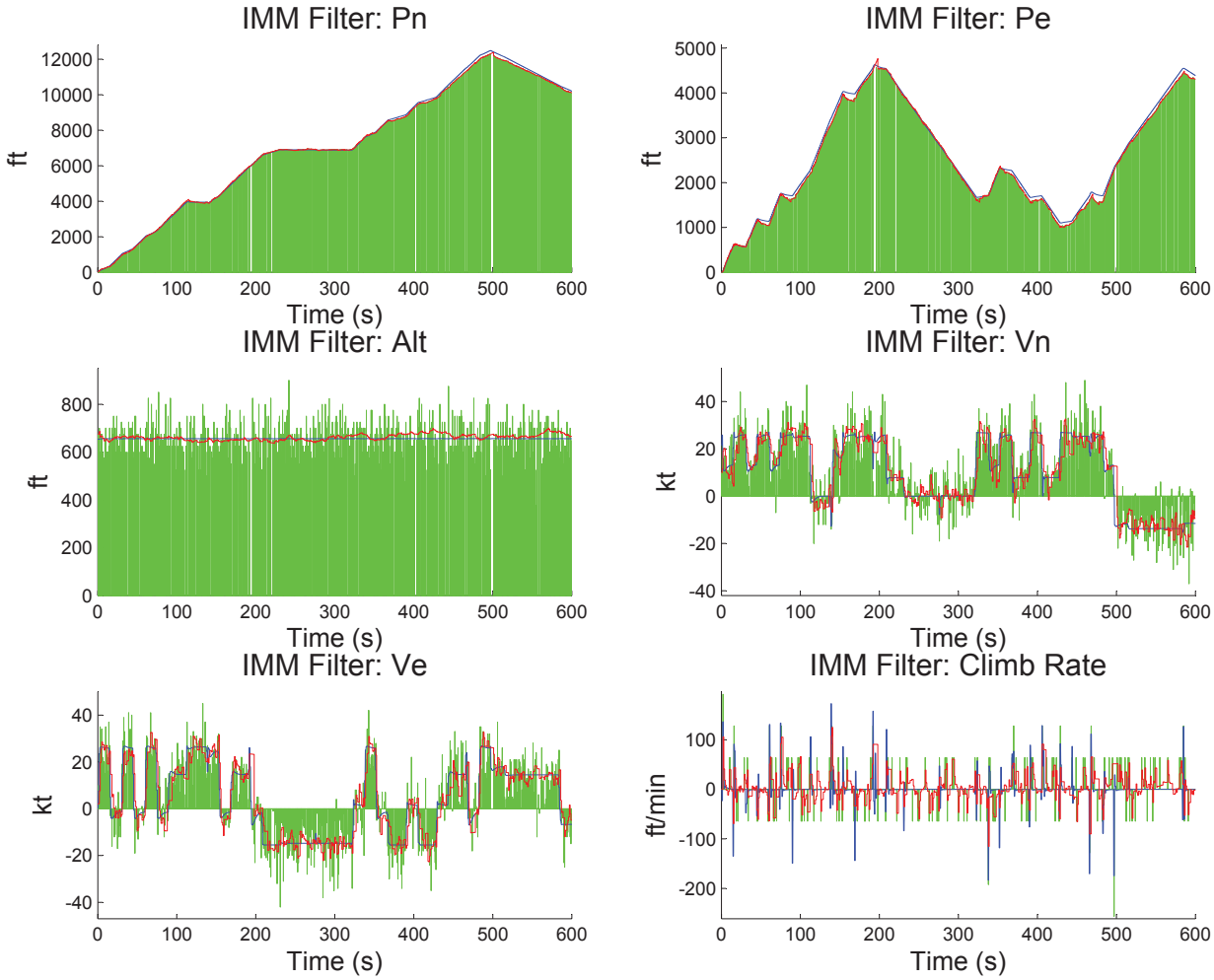

Figure 3.3: Performance of the interacting multiple models filter for simulated ADS-B measurements.

The estimation results for the IMM estimator are shown in Figure 3.3. From Figure 3.3 it is clear that the IMM estimates the ADS-B measurements well. Its performance is much less noisy than the KF-CJ and closely resembles that of the KF-NCV. Both the KF-NCV and IMM filters estimate the north and east velocity from the position with the same level of accuracy. Due to the fact that the one of the filters in the IMM is a nearly-constant-velocity Kalman filter, this similarity of results is expected.

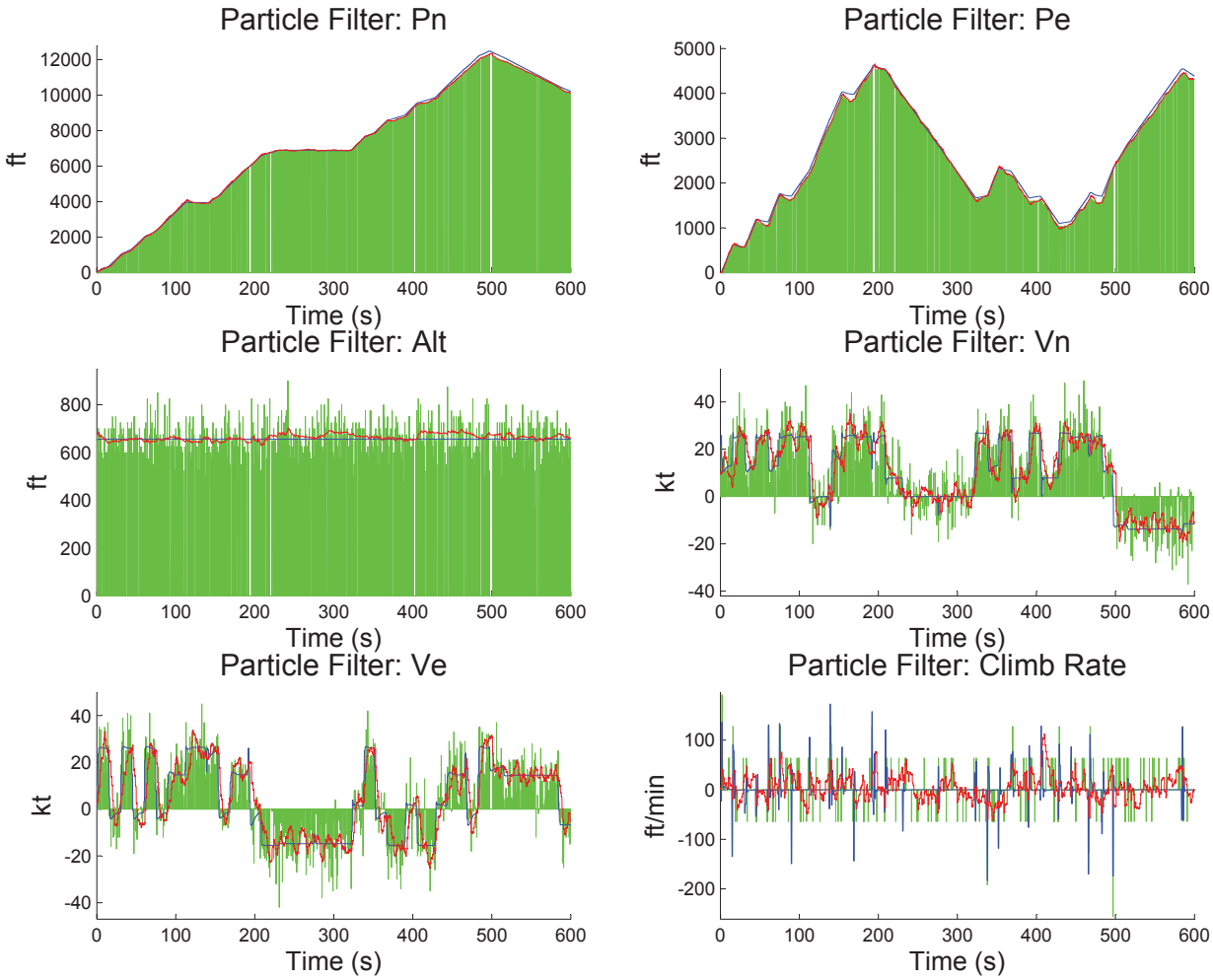

Figure 3.4: Performance of the particle filter for simulated ADS-B measurements.

The particle filter estimation results are shown in Figure 3.4. Even with using a relatively low number of particles, the PF is able to fairly accurately estimate the states of the UAS. The position north, position east, and altitude estimates are similar to the KF-NCV, KF-CJ, and IMM.

The velocity estimates much less noisy than the KF-CJ shown in Figure 3.2, but they are slightly noisier than the velocity estimates from the KF-NCV and IMM. As previously mentioned, a larger number of particles would result in a better estimate, but would also be much more computationally expensive. The number of particles in the particle filter was tuned to be the maximum number of particles possible for the estimator to run in real time at 100 Hz.

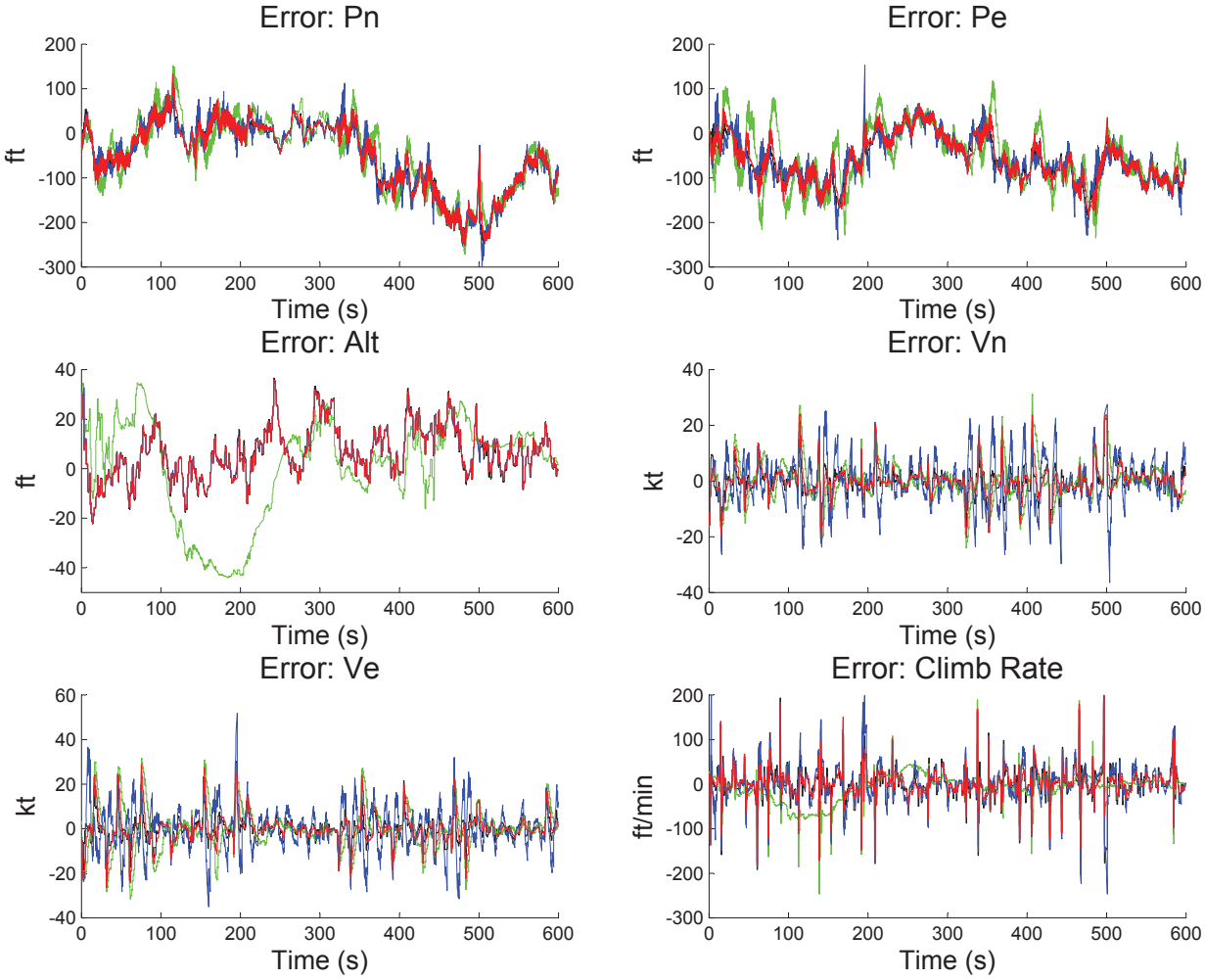

Figure 3.5: Error plots of the estimates from each of the four estimators.

A graphical assessment of the estimators is shown in Figure 3.5. In Figure 3.5 the red line is the KF-NCV error. The blue line is the KF-CJ error, and the green line is the PF error. The IMM error is shown in black. While the plots clearly show that there is error in all of the estimates,

it is clear that the some of the estimates are much smoother than others especially in the velocity estimates.

Table 3.1: Estimator comparison statistics.

State	Estimator	RMS Error	95th Percentile Error	Error Standard Deviation
Pn (ft)	KF-NCV	91.91	193.96	76.47
	KF-CJ	93.32	200.99	77.67
	IMM	92.97	198.21	77.28
	PF	92.03	198.84	76.38
Pe (ft)	KF-NCV	79.06	139.30	52.43
	KF-CJ	79.06	138.12	52.37
	IMM	78.87	140.46	52.66
	PF	79.33	140.96	54.02
Alt (ft)	KF-NCV	12.27	24.52	10.06
	KF-CJ	11.94	24.55	10.02
	IMM	14.04	28.99	12.72
	PF	15.58	29.80	13.46
Vn (kt)	KF-NCV	5.61	13.88	5.61
	KF-CJ	8.31	17.98	8.31
	IMM	5.68	11.95	5.68
	PF	6.18	14.54	6.18
Ve (kt)	KF-NCV	7.13	17.37	7.13
	KF-CJ	9.82	20.44	9.82
	IMM	6.43	13.36	6.43
	PF	7.60	17.82	7.60
Climb Rate (ft/min)	KF-NCV	34.43	70.88	34.41
	KF-CJ	45.27	99.33	45.25
	IMM	39.30	83.08	39.10
	PF	37.46	78.80	37.28

A quantitative assessment of the performance of each of the estimators is shown in Table 3.1. This table shows the RMS error, 95th percentile error, and error standard deviation for each of the states and each of the filters. The results in Table 3.1 support the observations from the plots in Figures 3.1 through 3.4. All of the filters perform similarly in estimating position north, position east, and altitude. In estimating the velocities, the KF-NCV and IMM consistently have

the most accurate and smoothest estimates. The KF-CJ has the worst velocity estimates of the group. At a first glance the position estimates from all the filters seem to have a very large RMS error. In terms of aircraft in the NAS, however, 92 ft is not an excessive amount of error. A Boeing 737 has a wingspan of 94 ft, and thus an RMS error of 92 ft results in an estimate that less than one wingspan of a large aircraft.

One important result of the statistics shown in Table 3.1 is that the filters smooth the measurements considerably. As derived in Chapter 2, the standard deviation of the north and east position measurements is 124 ft. The standard deviation of the barometric altitude measurements is 75.9 ft. The horizontal velocity measurements have a standard deviation of 8 kt, and the vertical velocity standard deviation is 27.96 ft/min. Each of the filters smooths the position measurements significantly, and all but the KF-CJ smooth the horizontal velocities. The error standard deviations of the climb rate estimates initially seem to be larger than the measurement standard deviation, but the climb rate measurements are discretized into 64 ft/min bins. This means that the 27.96 ft/min climb rate measurement standard deviation is deceiving. The smoothing of the estimates can be readily seen in comparing the red and green lines in Figures 3.1 through 3.4.

Table 3.2: Estimator run time comparison.

Estimator	Run Time (s)
KF-NCV	$3.57e^{-5}$
KF-CJ	$3.93e^{-5}$
IMM	$1.96e^{-4}$
PF	$9.16e^{-3}$

Table 3.2 shows the average run time for one iteration of each filter. The speed tests were executed in MATLAB on a CORE i5 processor. Each of the filters runs faster than real time at 100 Hz in MATLAB and, as such, would run much faster than real time in a compiled programming language such as C++. The KF-NCV was the most computationally efficient estimator. The IMM filter was three times slower than the KF-NCV. Due to the fact that the IMM filter is made up of three Kalman filters this is expected. While the particle filter does run in real time, it is three hundred times slower than the Kalman filters.

3.2.6 Comparison Conclusions

In testing and comparing the performance of the KF-NCV, KF-CJ, IMM, and PF, it is clear that all of the filters are capable of satisfactorily estimating ADS-B measurements. With regards to performance, the KF-NCV and IMM are the best estimators. In terms of computational efficiency, the KF-NCV and KF-CJ estimators achieved the best results. Overall the KF-NCV was the most suitable estimator for ADS-B measurements on a small UAS.

3.3 Notes on Estimating Recorded ADS-B Measurements

Due to the fact that truth information is not available for recorded ADS-B measurements, we use the results from the estimator comparison for simulated measurements to choose our estimator for recorded ADS-B data. Based on those results, we implement a nearly-constant-velocity Kalman filter to estimate recorded ADS-B measurements from the NAS. Estimation of multiple real ADS-B tracks adds a degree of complexity to the tracking task. Although no data association is necessary for multiple ADS-B measurements, track management is a challenge. Methods are necessary to determine how and when to initialize and terminate tracks. For our implementation a track is formed when two measurements are received within close enough succession that the Kalman filter Mahalinobis gate does not discard the more recent measurement as an outlier. A track is terminated when the estimate covariance grows so large that the track is unreliable. In our implementation this value is set to the maximum NIC value of 1215.2 ft. If an aircraft reappears after its track has been terminated, a new track is initialized from the new measurements.

3.3.1 Data Gathering Methods

To record ADS-B from the NAS, a Clarity dual-link ADS-B receiver is used. The Clarity unit is capable of receiving ADS-B on both 978 MHz and 1090 MHz frequencies. The received ADS-B messages are then passed to a laptop via a WiFi connection. A manufacturer-supplied SDK decodes the received ADS-B packets into a usable form. With some modifications to the SDK, we are able to record ADS-B measurements from the Clarity receiver in real time.

3.3.2 Processing Measurements for Estimation

After recording the ADS-B measurements, some post processing is necessary to prepare them for estimation. The primary modification is converting the latitude and longitude measurements into a position north and position east reference frame. This conversion from latitude and longitude can be done using a spherical earth model and an arbitrary reference latitude and longitude as the origin. Given ϕ_r as the latitude reference point and λ_r as the longitude reference point and ϕ and λ as the latitude and longitude measurements respectively,

$$P_n = R_e(\phi - \phi_r) \tag{3.1}$$

$$P_e = R_e(\lambda - \lambda_r)\cos(\phi). \tag{3.2}$$

R_e is the radius of the earth. This method transforms the latitude and longitude measurements into a position north and position east reference frame. In addition to transforming the latitude and longitude measurements, it is necessary to convert the other state measurements into a coherent set of units. Altitude measurements are reported in feet. Velocity measurements are in knots, and climb rate measurements are in feet per minute. For our post processing, we convert all measurements to be in meters and meters per second.

3.3.3 Recorded Data Incongruities

In estimating recorded ADS-B measurements, there are three data incongruities that must be mitigated. First, depending on the receiver proximity to an ADS-B ground station, ADS-B measurements can be recorded twice in close succession. This is a result of ground-based ADS-R transmissions that repeat ADS-B on the other frequency. To prevent the estimator from updating with the same measurement twice, we gate incoming measurements to ensure that they were not identical to the previous position measurement. Second, 1090 MHz ADS-B transmissions do not transmit all of the required information in a single broadcast. Several different broadcasts over the course of one second are necessary to transmit all of the required message elements. As a result it is necessary to update the estimates with whatever information is most current. For example, if the horizontal position information is received in the first half of the second, then the filter updates

with only the horizontal position information as soon as it receives it. When the altitude and climb rate information are received later on in that second, the estimate is updated with the altitude and climb rate information only. This creates a more complex, but ultimately more accurate estimator. Third, as previously mentioned, recorded ADS-B measurements occasionally have the horizontal velocities switched. Thus the north velocity is transmitted in the east velocity element field and vice versa. To mitigate this, the estimator is updated with the horizontal positions, altitude, and climb rate only. As can be seen in the previous sections, the horizontal velocity estimates are still accurate even without velocity measurement updates.

3.3.4 Recorded Data Estimation Results

Figure 3.6 shows the results of the estimation for one of the ADS-B tracks recorded from the NAS. The green lines show the measurements, and the red line shows the estimates. It is clear from Figure 3.6 that the KF-NCV estimates the position north, position east, altitude, and climb rate measurements very well. The velocity north and velocity east estimates are slightly noisier than the other estimates, but they are still accurate. It is important to note that there is a brief initialization period for each of the estimates. This occurs in the first seconds of the track as the estimator receives more and more measurements with which to refine the estimate. After the brief transient period, the filter is able to provide very accurate estimates.

Due to the fact that the recorded data was gathered using an ADS-B receiver on the ground, the measurements were not received as regularly as would be expected of an airborne receiver. Although an effort was made to find an obstruction-free area to gather data, there were still buildings and trees that obscured ADS-B measurements. In the data this is particularly evident in the first and last few measurements for a given track. Thus to efficiently initialize the track, it was necessary to increase the Mahalinobis gate considerably to be 15 standard deviations. This gate size allowed the track to initialize even while receiving only sporadic measurements as the aircraft came into view.

With regards to run time, the KF-NCV estimated 261 s of ADS-B messages in 25.78 s. Thus with the track initialization and termination additions, the KF-NCV is capable of running approximately ten times faster than real time in MATLAB. Such fast computational speed achieves

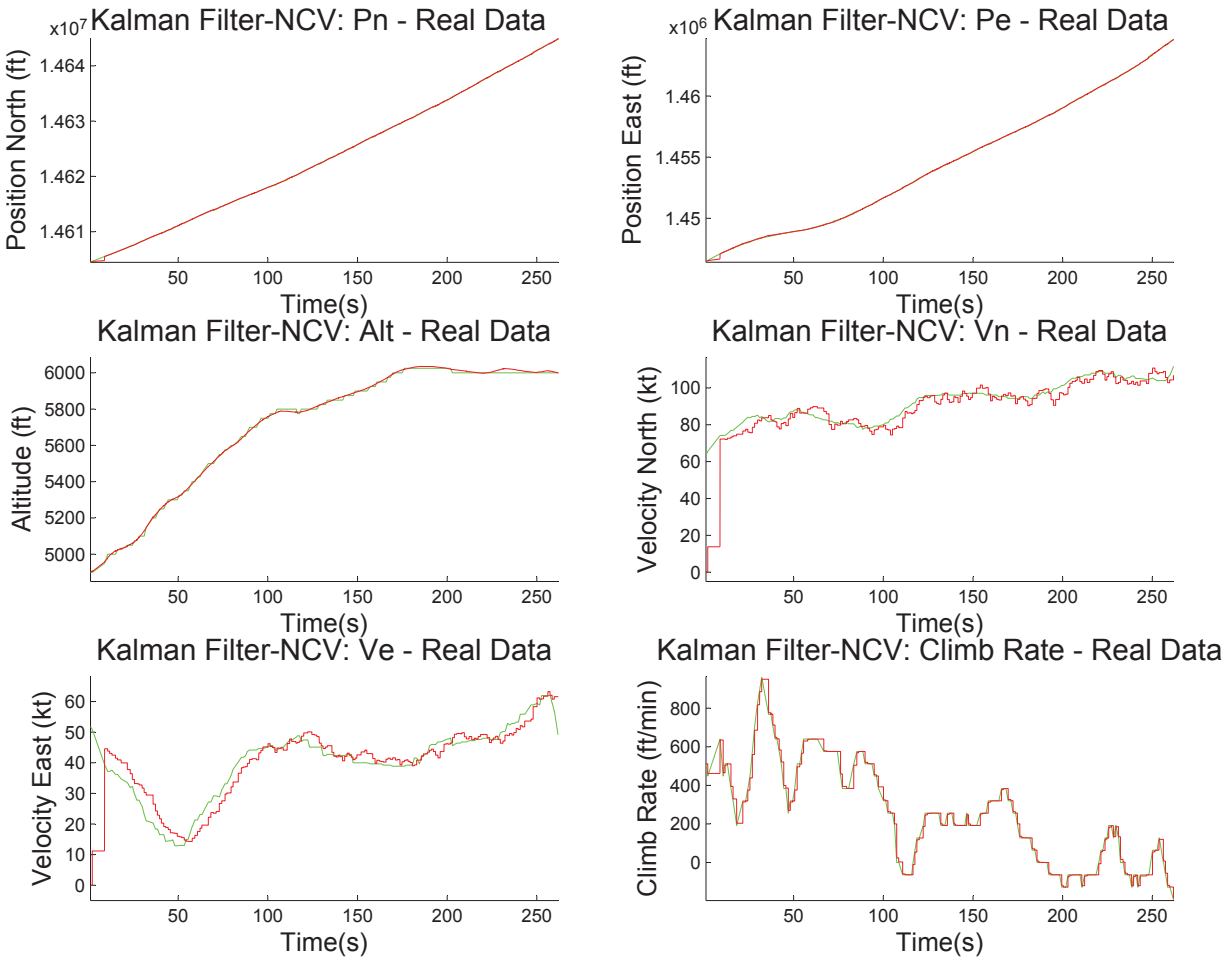

Figure 3.6: Performance of the nearly-constant-velocity Kalman filter for recorded ADS-B measurements.

the estimation goal and allows a significant amount of time for the computational demands of other algorithms such as conflict/collision detection and avoidance.

3.4 Estimation Conclusions

In conclusion, estimating the state information included in ADS-B messages overcomes much of the error in those messages. The results from the estimator comparison show that a nearly-constant-velocity Kalman filter is capable of mitigating ADS-B dropout and noise while providing accurate, real-time estimates. Furthermore, the results of the recorded ADS-B estimation demonstrate that with modifications to account for track initialization and termination a KF-NCV

is capable of providing real-time estimates of true ADS-B data at 100 Hz. Overall the KF-NCV presented in this chapter is an accurate and efficient estimator for both real and simulated ADS-B measurements. Furthermore, the accuracy of the estimates from the KF-NCV provides a good foundation on which to build DAA algorithms for conflict/collision detection and avoidance for small UAS.

CHAPTER 4. AN ADS-B-BASED SELF-SEPARATION PLANNER

One key strength of ADS-B that sets it apart from other currently available sensors is the long range over which ADS-B information is available. This information can be used to maintain self-separation rather than solely relying on close-range information from radar or cameras to achieve collision avoidance. Thus long-range, accurate measurements from filtered ADS-B measurements have the capacity to increase the level of safety for small UAS operations.

While this long-range intruder information is very valuable, much of the benefit is lost if there is no suitable method to utilize the information to inform the ownship path planning. As a result long-range path planning methods capable of avoiding dynamic obstacles are necessary. Some of the challenges that accompany long-range separation path planning are the computational expense of long-range path planning, uncertainty in intruder aircraft positions, and unpredictability of intruder aircraft future maneuvers. To develop a path planning method that offers the benefits of ADS-B-based separation assurance and to mitigate the associated challenges, this chapter presents a convex optimization-based path planner for self-separation assurance on UAS in a dynamic environment.

4.1 Problem Formulation

The approach for this research is to use convex, constrained optimization techniques to optimize the position of waypoints, or nodes, along a path so as to find the minimum length path. The problem formulation, robustness measures, and underlying assumptions are detailed in this section. The overall problem formulation uses a squared Euclidean distance as the objective function. The Cartesian coordinates of each node are the design variables, and the self-separation criterion serves as a linear constraint. This formulation is given formally as

$$\text{Minimize} : \sum_{i=1}^{n-1} (x_i - x_{i+1})^2 + (y_i - y_{i+1})^2 + (z_i - z_{i+1})^2 \tag{4.1}$$

$$\text{With respect to} : x_1, x_2, ..., x_n, z_1, z_2, ..., z_n \tag{4.2}$$

$$\text{Subject to} : ||[x_i, y_i, z_i] - [x_{i-1}, y_{i-1}, z_{i-1}]||_2 \leq \mathit{Threshold} \tag{4.3}$$

$$x_{min} \leq x_i \leq x_{max} \text{ or} \tag{4.4}$$

$$z_{min} \leq z_i \leq z_{max}.$$

4.1.1 Objective Function

The squared Euclidean distance formula shown in Equation (4.1) provides an intuitive choice for a path-length-minimization objective function. Excluding the square-root operation from the typical Euclidean distance formula simplifies the objective function and reduces it to a second-order function. While the output of the objective function no longer represents the length of the path, and consequently is less intuitive, the overall optimization is more efficient. More importantly the second-order formulation of the distance formula is convex, where as the standard Euclidean distance is not.

4.1.2 Design Variables

The design variables for the optimization are the x and z coordinates of each of the path nodes in the local frame where the x axis lies perpendicular to the nominal path in the horizontal plane and z axis points upward. The y coordinate for each node lies along the nominal path and is excluded to reduce the dimensionality of the problem. This exclusion does not significantly reduce the flexibility of the solution due to the fact that prior to optimization the positions of the start and end node can be linearly transformed to both lie on the y axis. In such an orientation, the most impactful coordinate variation will occur orthogonal to the y axis. Thus, the y coordinate is an unnecessary dimension. Figure 4.1 shows the orientation of the x-y-z local coordinate frame.

Another key consideration in selecting the design variables is the number of nodes between the start and end node. A greater number of nodes adds more degrees of freedom to the solution,

and increases the computational requirements of the optimizer. Fewer nodes requires less computational expense, but also reduces the conformability of the path. A brief analysis of the effect of the number of nodes is shown in Section 4.3 of this chapter.

4.1.3 Constraints

The constraints are designed to ensure that at every time step the ownship maintains self-separation from each intruder aircraft. Additionally the constraints are designed to be linear so as to ensure the convexity of the problem [44]. The constraint in Equation (4.3) is straightforward. It requires that two nodes not be separated by more than a given distance. This prevents the nodes from being so far apart that an intruder can be between two nodes without violating the bound constraint in Equation (4.4). Although the constraint in Equation (4.3) is not linear, it is a convex formulation of a sphere. The constraints in Equation (4.4) are formulated such that the nodes must be between an upper and lower bound constraint, *min* and *max* respectively. The value of these constraints is determined by the position of the intruders. Using the speed of the ownship, it is possible to calculate the time when the ownship will arrive at each node. With the position and velocity estimates of the intruder, it is also possible to linearly extrapolate the states of the intruders into the future to determine their positions when the ownship arrives at each node. The intruder positions at the appropriate time become the bound constraints for each path node. The constraint is offset from the nominal position of each intruder so as to provide the recommended buffer for self-separation. A set of heuristics is applied to determine whether each intruder should be considered an upper or lower bound. The heuristics are necessary to allow for a broader feasible region than would be available with only one set of linear constraints by systematically determining whether each constraint should be an upper or lower bound. A detailed description of the heuristics is included Section 4.2 of this chapter.

Figure 4.1 provides a graphical example of how the constraints are determined. The waypoint at time t_3 is constrained to be above the line created by the position of intruder A. This constraint is offset from the nominal position of the intruder by R_{buffer} and results in a lower-bound constraint. At the node for t_7, the position of intruder B creates an upper bound constraint which constrains the position of the corresponding path node. By combining the upper and lower bound constraints for each path node, the feasible optimization space becomes a channel or corridor be-

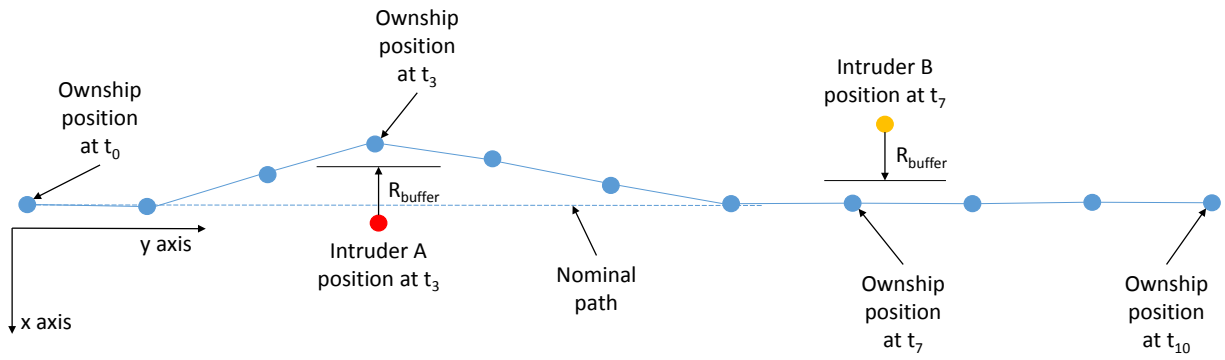

Figure 4.1: An example of how the upper and lower constraints are formed.

tween the two sets of constraints. While this method does require preprocessing of the intruder positions and velocities, it results in a set of convex, linear constraints.

4.1.4 Robustness

The nature of long-range, time-based path planning requires extrapolation of intruder positions over long time horizons. This necessity introduces two forms of error: state error and model error. State error results from the growing uncertainty as imperfect state information is propagated into the future. Model error also grows as it is predicted into the future, but it results from uncertainty in the model by which the information is propagated. To mitigate these two types of error, we use a successive replanning method. Successive replanning robustness is a method by which the path is re-planned at regular intervals. While this is not a new method, it does significantly contribute to the overall applicability of the path planner. Velocity uncertainty, unpredictable maneuvers, and environmental factors such as changes in wind can be addressed by regularly replanning the optimized path. This is a major reason that the computational expense of the optimization routine is of interest. With a more rapid path planning method, new plans can be generated more quickly and more often.

4.1.5 Assumptions

For this problem formulation several assumptions are necessary. The assumed sensor with which intruder information is gathered is ADS-B. This sensor provides latitude, longitude, altitude,

ground speed, heading, and climb rate. The intruder positions and velocities used to propagate intruder positions into the future are derived from this information. Furthermore the propagation method for intruder positions is a constant-velocity method. Thus, it is assumed that the intruders are not maneuvering. While this assumption may not be entirely correct, successive path replanning can alleviate much of the error in the assumption. The distances used in the intruder buffer, R_{buffer}, are proposed well clear definitions from the Sense and Avoid Science and Research Panel (SARP) [22,23]. In the horizontal plane $R_{buffer} = 4000$ ft, and in the vertical plane $R_{buffer} = 500$ ft.

4.2 Optimization Implementation

While the formulation of the optimization is rather straightforward, the implementation leverages several key aspects that lead to the success of the optimization. One of the primary goals of the implementation is to achieve and maintain a convex problem formulation. In Equation (4.4), only one set of upper and lower bound constraints must be satisfied, either the vertical or the horizontal. While each individual set of constraints is convex, the "either-or" formulation is not convex. An "and" formulation of the horizontal and vertical constraints would be convex, but such a formulation would result in avoidance paths that are not representative of true aircraft behavior which rarely combines vertical and horizontal maneuvers. To mitigate this we address each direction, vertical and horizontal, separately. Essentially we run separate optimizations in the same sequential planning iteration. In the first run, we allow the z coordinates to vary, and we impose the vertical set of constraints. For the second run, we allow the x coordinates to vary, and we impose the horizontal set of constraints.

As mentioned previously a set of heuristics is necessary to determine whether an intruder should be represented as an upper or lower bound constraint. In our implementation we use nine heuristics, four in the vertical direction and five in the horizontal direction. This results in nine separate optimization runs. While this does require multiple optimization runs, the efficiency of convex optimization allows for this sequential optimization without imposing too great a computational cost. It is important to note that while none of the heuristics is individually valid for all intruder scenarios, the collective set is designed to find at least one feasible path for a wide range of intruder configurations.

4.2.1 Constraint Heuristics

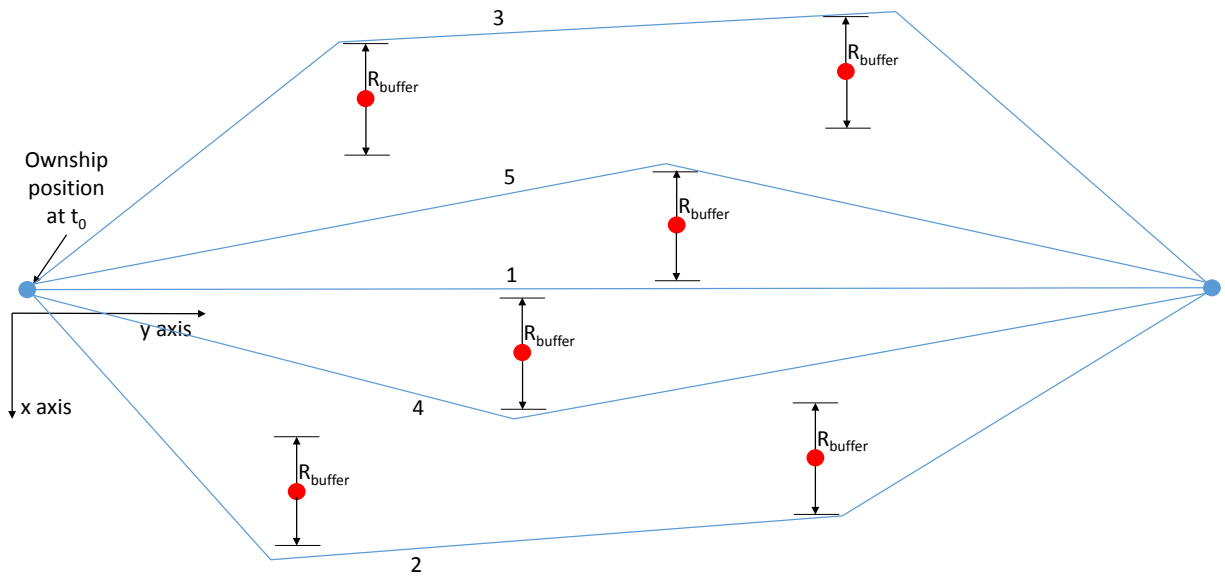

Figure 4.2: A diagram showing hypothetical path results from each of the first five heuristics.

Figure 4.2 shows the hypothetical resultant paths for each of the first five heuristics. The first heuristic is horizontal and categorizes the intruders based off of the straight-line path between the start and end node. Essentially if an intruder has a position on the positive x axis then the constraint will be an upper bound constraint. Alternatively, if the intruder's position is on the negative x axis then the constraint will be a lower bound constraint. This heuristic is intended to identify the straight-line path between the start and end node. The second heuristic is also horizontal. It seeks to find a path to the right of all intruders. Simply put this method identifies all intruders as lower bound constraints. If all intruders are moving on the left side of the ownship, then this method will find a feasible path. The third heuristic is an analog to the second in that it seeks to find a path to the left of all intruders. All intruders are viewed as an upper bound. Thus, if all of the intruders are to the right of the ownship, this heuristic will lead to a feasible path. The fourth heuristic also seeks a path to the right of the ownship, but is looks for a gap in the traffic. In other words, instead of trying to fly either along the straight-line path or to the right of all of the intruders, it looks for a gap between the intruders on the right hand side. This allows the ownship to find a path that is much shorter than going around all intruders. If there is not gap available, this

heuristic results in a path that is identical to the path around the right of all of the intruders. The fifth heuristic is identical to this method except that it looks for a gap to the left.

The sixth, seventh, eighth, and ninth heuristics are vertical heuristics. They are direct analogs to the second, third, fourth, and fifth heuristics shown in Figure 4.2 in that they look to fly above all the intruders, below all of the intruders, through a gap above the straight line path, and through a gap below the straight-line path respectively. After all of the optimization runs have been completed, the final path is selected based on the length of the path. Thus, the shortest overall path from all nine of the optimization runs is selected as the path. Overall, this set of nine heuristics significantly increases the feasible optimization space. It also allows for a convex "either-or" formulation for the horizontal and vertical formulation.

4.2.2 Convex Solver

To solve the convex optimization we used CVX, a package for representing and solving convex programs [45, 46]. Due to the fact that this tool was designed to run with MATLAB, it was very useful for our development. For implementation on a small UAS platform, however, we would use a solver that is compatible with C++ or some other compiled language. Implementation in a compiled language would result in much greater computational efficiency.

4.3 Results

Testing of the convex optimization-based path planner for self-separation included single iteration feasibility testing, an analysis of the number of nodes and run time, and a simulation-based test of the sequential path planning robustness.

4.3.1 Single Iteration Testing

The goal of the single iteration feasibility testing was to determine how the optimizer responds in scenarios with a high number of intruders. To test this, the optimizer had to find a feasible path between a start and end node in the presence of ten intruders. The start and end point of the path were placed at (0, 0, 8200) and (0, 91141, 8200) feet respectively. The path between the start and end nodes had 78 evenly spaced intermediate nodes.

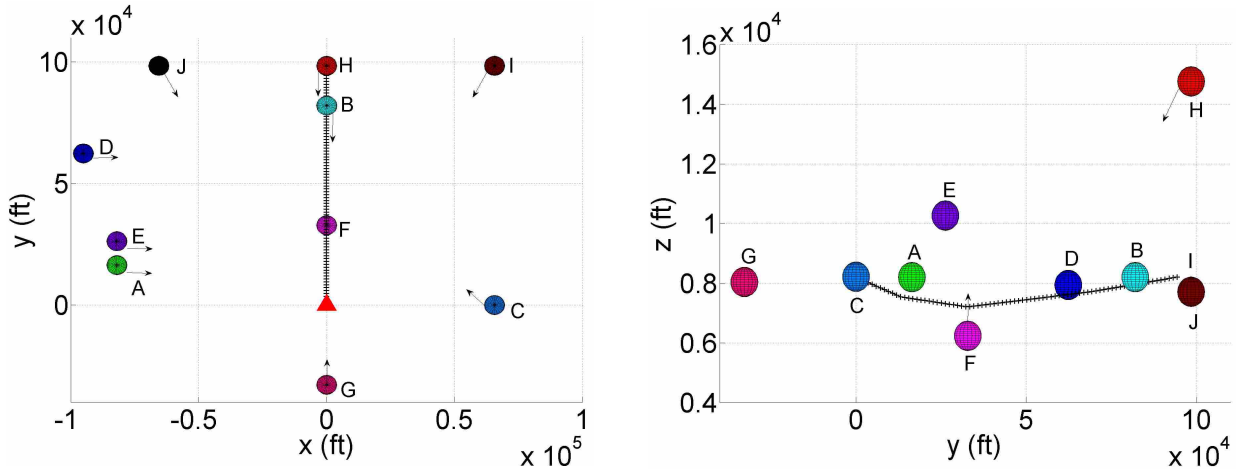

(a) Top View

(b) Side View

Figure 4.3: Initial positions and velocities of the intruders.

Table 4.1: Initial intruder positions and velocities.

Intruder	Px (ft)	Py (ft)	Pz (ft)	Vx (kt)	Vy (kt)	Vz (ft/min)
A	-82021	16404	8200	97.1	0	0
B	16	82021	8200	0	-19.4	0
C	65617	0	8215	-29.2	29.2	0
D	-95144	62336	7940	77.8	0	0
E	-82021	26247	10266	97.2	0	0
F	0	32808	6234	0	0	984.3
G	0	-32808	8038	0	97.2	0
H	0	98425	14764	0	-55.4	-787.4
I	65617	98425	7710	-58.3	-58.3	0
J	-65617	98425	7710	149.7	-233.3	0

Figure 4.3 shows the initial intruder states for the scenario. The circles in the figure represent the self-separation volume of the intruders. The red triangle is the ownship, and the nodes of the path are represented by the crosses along the black ownship path. The arrows in the figure show the direction of travel for each of the intruders. From the figure it is clear that there are crossing intruders from both sides, a head-on intruder, an overtaking intruder, a descending intruder, and a climbing intruder. Each of the intruders are positioned so as to interact with the ownship either by crossing the ownship's path or by flying near to the path so as to increase the complexity of the solution space. To provide a quantitative perspective, Table 4.1 lists all of the initial intruder

positions and velocities. The alphabetical labels in the table correspond to the labeled intruders in Figure 4.3. Ultimately this set of intruders represents a very complex self-separation scenario.

With the intruder configuration shown in Figure 4.3, we ran the convex optimization-based path planner for self-separation. The results of the optimization are shown in Figure 4.4. To provide a three dimensional, time-variant perspective of the results, Figure 4.4 includes subfigures that show the ownship progress along the optimized path. Figures 4.4(a)-4.4(c) show a top, end, and side view, respectively, of the optimized path while the intruder is at the initial node. The subsequent rows show a similar perspective when the ownship is at node #20, #50, and #80 respectively. A video of the path optimization result is available at `https://youtu.be/-xjgWVy27Q0`.

Figure 4.5 shows the closest point of approach by any intruder over the course of the simulation shown in Figure 4.4. The blue line is the the distance from the ownship to the closest intruder, and the red line is the vertical separation threshold. The key takeaway from the plot is that the vertical separation threshold is not violated at anytime through out the simulation.

From Figure 4.4 and 4.5 it is clear that the optimizer maintains self-separation from all of the intruders throughout the entire path. This is the primary goal of the optimization. It is interesting to note that the optimizer selected a vertical avoidance path. This results from the fact that the self-separation definition requires 4000 ft of separation in the horizontal plane, but only 500 ft of separation in the vertical plane. Thus, it is reasonable that the optimizer nearly always finds a vertical avoidance path [47]. Another reason that the optimizer typically finds a vertical avoidance path is that the ownship is moving slowly compared to the intruders. The ownship is designed to resemble a small UAS, and it is only moving at 29 kts. This is slower than all but one of the intruders. Thus, the ownship is unable to outrun the intruders. In finding a horizontal avoidance path with linear constraints, this means that it is very easy for intruders crossing from different directions to pinch off the channel through which the ownship might fly. Thus, there is a greater likelihood that a vertical path will be feasible than there is that a horizontal path will be feasible.

To determine the limitations of the planner, we identified and tested several conditions where the planner fails to find a feasible solution. If the self-separation volumes are excessively large, the optimizer is unable to find a viable solution. We tested the optimizer with collision volumes equivalent to the FAA ATC-separation volumes for manned aircraft. These volumes require

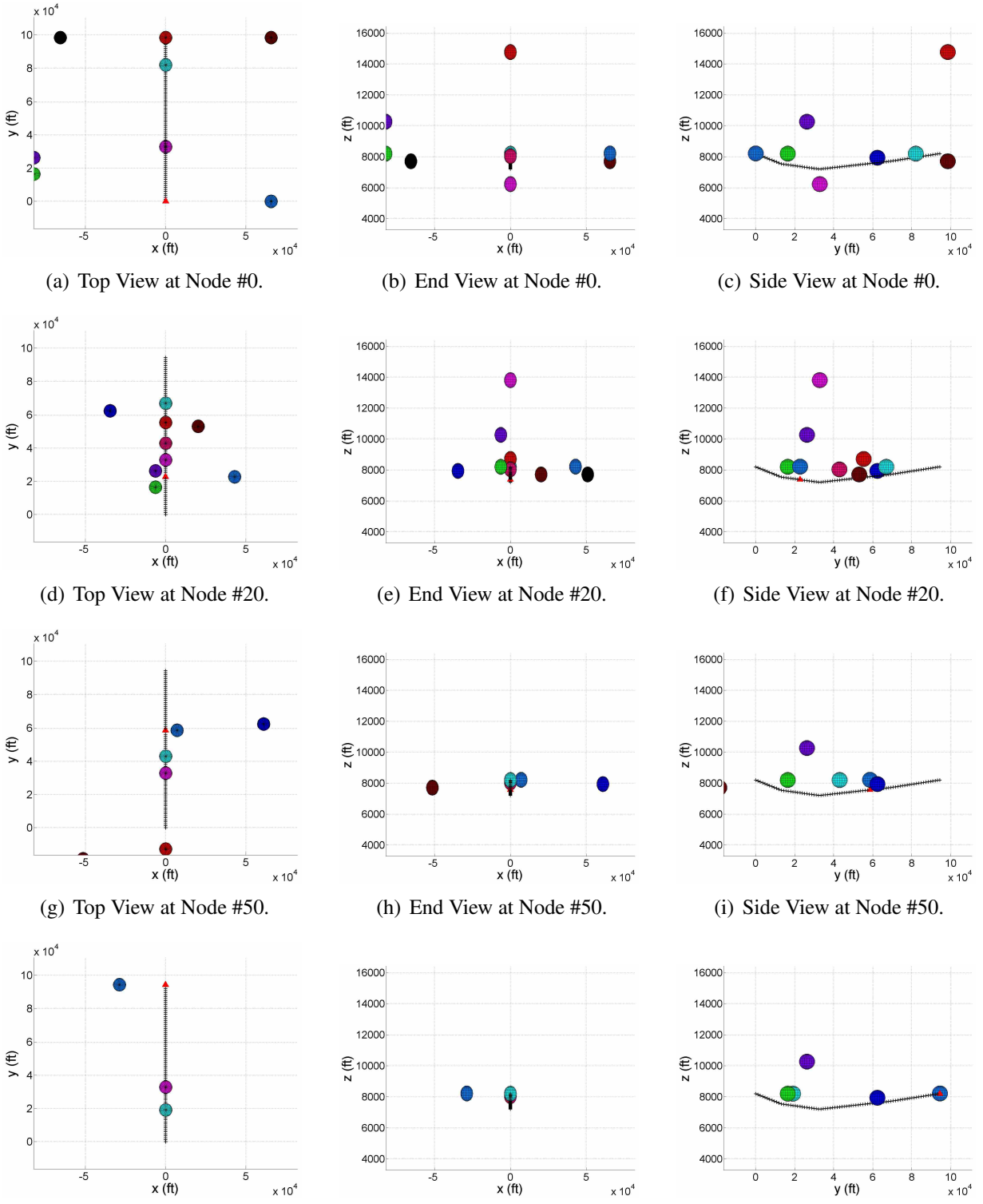

(a) Top View at Node #0. (b) End View at Node #0. (c) Side View at Node #0.

(d) Top View at Node #20. (e) End View at Node #20. (f) Side View at Node #20.

(g) Top View at Node #50. (h) End View at Node #50. (i) Side View at Node #50.

(j) Top View at Node #80. (k) End View at Node #80. (l) Side View at Node #80.

Figure 4.4: Self-separation path as time progresses.

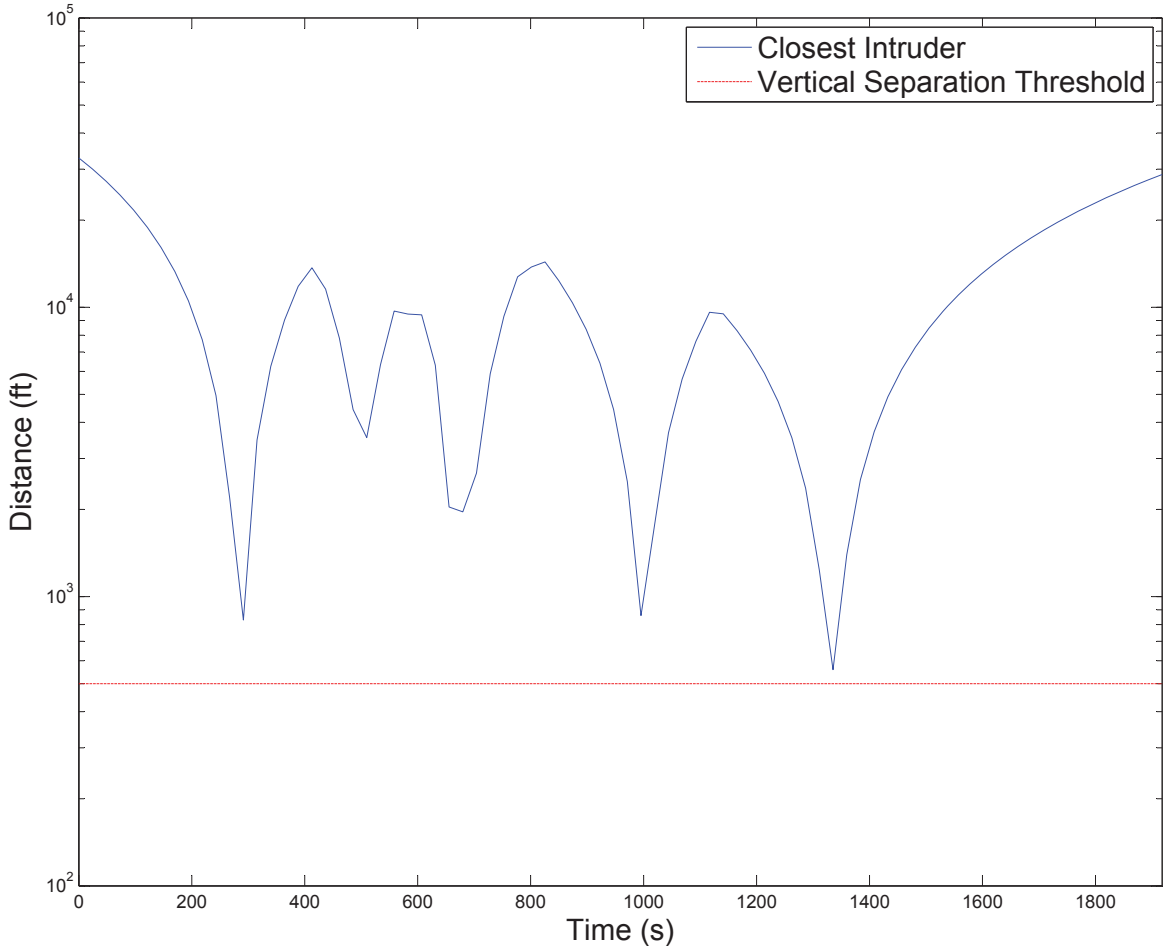

Figure 4.5: The closest point of approach amoung all intruders over the course of the simulation.

5 nmi of separation horizontally and 500 ft of separation vertically. While the optimizer is able to find a feasible path for some of these scenarios, it fails to find a feasible path for scenarios with more than approximately 5 intruders. This is a result of the solution space being overwhelmed by the large separation volumes. Another condition where the path optimizer fails is when there is an intruder on top of, or very near to, either the start or end node. This prevents the ownship from approaching the end node, to which it is constrained. Thus, a feasible path cannot be found.

In extended testing the optimizer successfully found a feasible self-separation path in the presence of up to 19 intruders on a collision path with the nominal path of ownship. This scenario included multiple crossing, climbing, and descending intruders from all directions. The ability of the optimizer to successfully plan a path in the presence of 19 intruders converging on the ownship is a testament to the viability of the planner and the robustness of the nine heuristics.

Table 4.2: Change in run time and path length as a function of the number of nodes.

# of Nodes	CPU Time (s)	Path Length (ft)
60	3.45	94411.90
80	3.82	94411.54
100	4.50	94412.61
120	4.74	94412.08

Table 4.2 shows an analysis of the CPU time verses the number of nodes along the path. The optimization runs for this table were executed in MATLAB on a 3.1 GHz CORE i5 processor. One very interesting correlation in the results is that as the number of nodes increases, the run time increases slightly and the path length remains essentially unchanged. This correlation indicates that when choosing the number of nodes it is reasonable to err on the side of fewer nodes.

Another important observation from Table 4.2 is that all of the CPU times shown are slower than the 1 Hz measurement rate of ADS-B. While this initially seems to be a serious downfall of the path planning method, it is not a significant drawback. Any implementation of this path planner on a UAS would require a conversion from MATLAB to C++ or a another compiled language. In converting from MATLAB to a compiled language, such as C++, the computational expense of the planner will significantly decrease. An additional factor that reduces the impact of slower-than-real-time computation is that since the resulting path of the planner is time-based, it does not lose validity over time in the same way that a non-time-based method does. A time-based path is computed using future positions of both the ownship and intruders. Thus, it is theoretically always valid. There is uncertainty in the propagated intruder positions and the timing associated with the path nodes, but this uncertainty is less impactful than the uncertainty associated with considering the intruders to be static. Thus, as a result of using an interpreted language for testing, and the increased validity period associated with a time-based path, the seemingly slow run times are not a significant concern.

4.3.2 Successive Path Planning Testing

The robustness testing was done using a full simulation to capture effects of the successive path planing robustness. The simulation executes the full dynamics of a 12-state ownship and

three 12-state intruders. In the simulation, the ownship is flying between two waypoints that are separated by 18.6 nautical miles. One intruder is overtaking the ownship from behind at a closing speed of 29.2 kts. Another intruder is approaching head-on at a closing speed of 77.8 kts, and a third intruder is crossing the path of the ownship from the right. All intruders are at the same altitude as the ownship. To generate ADS-B messages, the truth data from each of the intruders is corrupted using the error characterization based on FAA regulations for ADS-B error. Every 10 seconds the path optimizer plans a new path for separation assurance. The planner first checks the old path to determine whether it is still valid. If it is valid the optimizer outputs the previous path and no new optimization is performed. If the path is no longer valid, then the planner reoptimizes the waypoints. In light of the fact that the optimization occurs in the local frame of ownship as described in Section 4.1, it is necessary to linearly transform the global frame coordinates of the start waypoint, end waypoint, and intruder states into the ownship local coordinate frame. After the optimization the optimized path is transformed back into the global reference frame for the path following algorithm. Figure 4.6 shows the initial simulation scenario and the path flown by the ownship.

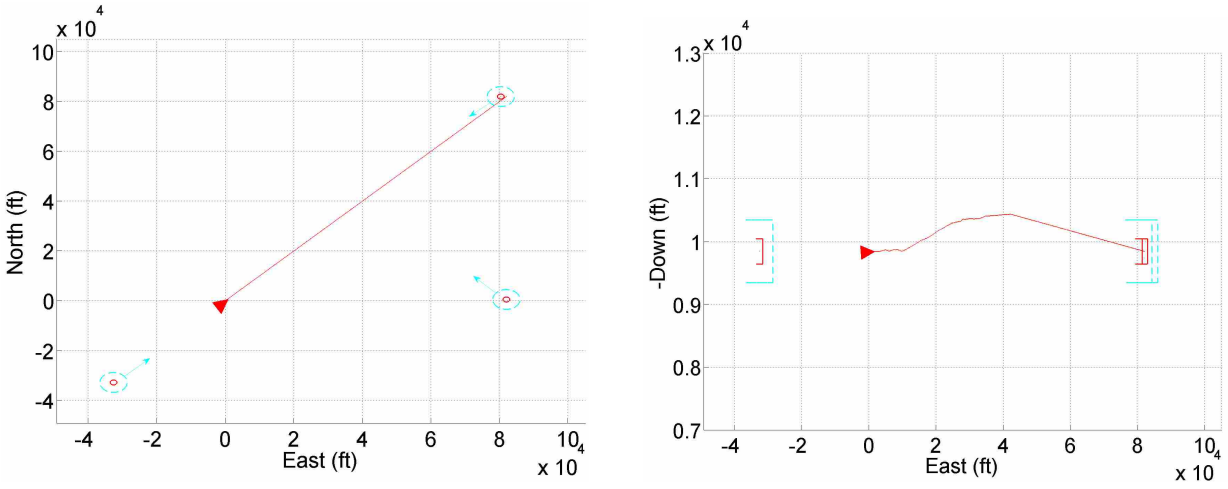

(a) Top View (b) Side View

Figure 4.6: Initial intruder configuration and the avoidance path flown by the ownship during the sequential planning simulation.

In Figure 4.6 a top view is shown in the left plot and a side view is shown in the right plot. The red triangle is the ownship. The red line shows the actual path flown by the ownship

over the course of the approximately 40 minute simulation with successive path replanning every 10 seconds. Each of the intruders is surrounded by both a blue circle indicating the separation volume and a red circle indicating the collision volume. Their positions in the figure show their initial positions and trajectories at the beginning of the simulation. Table 4.3 shows the maximum ownship elevation change, the maximum ownship climb angle, and the number of seconds in a loss of separation (LOS) state.

Table 4.3: Key metrics for the fully simulated path optimizer.

Metric	Value
Max Ownship Elevation Change	592.70 ft
Max Ownship Climb Angle	0.75 deg
Number of Seconds of LOS	7.06 s

The value of the optimization path planner is illustrated by Figure 4.6 and Table 4.3. The maximum elevation change and maximum climb rate listed in Table 4.3 demonstrate that the path planner can avoid a loss of separation with gradual maneuvers over a long time horizon. These gradual maneuvers are beneficial in that they support minimal deviations from peak efficiency operating conditions such as airspeed. They also present a relatively small variation from the original path and mission goals. Table 4.3 does indicate that there are short periods of time where the separation thresholds are not preserved. These violations are a result of the error in the intruder estimates. Due to the fact that each of the violations occurs at the top outer bound of the separation volume, the violation of the thresholds is of minimal concern. Additionally improved estimation of the intruder states would result in less error and thus the path planner could entirely prevent LOS. The small climb rate, reasonable maximum altitude change, loss of separation results, and robustness effectiveness combine to demonstrate the value of the optimization path planner presented.

4.4 Path Planning Conclusions

In conclusion, the convex, time-based path optimizer presented in this chapter is capable of long-distance path planning for separation assurance in an environment with dynamic obstacles. The convex optimization formulation allows for a large number of nodes which leads to high

resolution long-range planning without excessive computational cost. The incorporated robustness measures result in a path planner that is viable in the presence of uncertainty in intruder positions, velocities, and future maneuvers.

Additionally the ability to maintain separation assurance in the presence of head-on, overtaking, and crossing intruders illustrates the value of ADS-B information. In scenarios with intruders traveling much faster than the ownship, the combination of ADS-B information and the time-based path optimizer allows the ownship to maintain separation with gradual maneuvers. Ultimately the time-based path optimizer presented in this research is a capable, long-range path planner. As such it is a valuable path planner for separation assurance and a key step toward a DAA solution for UAS in the NAS.

CHAPTER 5. ADS-B BANDWIDTH LIMITATIONS

Given the vast number of applications for small UAS, future airspace conditions are likely to contain a large number of drones operating in close proximity to each other. In such a high-density environment, the need for small UAS to autonomously maintain self-separation from other aircraft, manned and unmanned, is particularly urgent and difficult. ADS-B is an off the shelf sensor that provides all the information necessary for small UAS to detect and avoid other aircraft. Due to the capability and accessibility of ADS-B, it is rapidly becoming one of the leading sensors for DAA. While ADS-B has many characteristics that make it excellent for DAA applications, it is susceptible to interference. If too many aircraft are transmitting on ADS-B in too small of an area, the individual messages will interfere with each other and become unintelligible to ADS-B receivers. Such a condition would severely inhibit the ability of small UAS to detect and avoid other aircraft. This chapter will provide an analysis of ADS-B bandwidth limitations and their effect on the ability of ADS-B to detect other aircraft.

5.1 ADS-B Bandwidth Limitations

The analysis of ADS-B bandwidth limitations presented here will focus on the 978 MHz frequency. As specified in Chapter 2, this frequency is intended for aircraft operating under 10000 ft. As such it is reasonable that the vast majority, if not all, small UAS will equip with the 978 MHz frequency.

5.1.1 ADS-B Multiple Access Scheme

To support ADS-B messages from multiple transmitters in the same second, the 978 MHz ADS-B frequency uses a time-division multiple access (TDMA) scheme. In other words, each ADS-B message is intended to be transmitted in its own time slot. The UAT message is divided up into two major time sections: the ground uplink message portion and the traffic transmission

portion. The combination of these two sections is referred to as a UAT frame. Each frame has a 6 ms buffer at the beginning, a 176 ms ground uplink message portion, another 12 second buffer, an 800 ms traffic transmission portion, and a final 6 ms buffer. This consumes one second [28].

The ground uplink portion of the UAT frame is intended for broadcasts of weather information, airspace notices (such as NOTAMS), and limited general traffic information. Due to the fact that these messages have a time slot separate from the traffic slot they neither contribute to nor detract significantly detract from the overall congestion of the air-to-air ADS-B transmissions.

The aircraft message portion is intended for traffic transmissions such as air-to-air ADS-B, ADS-R, and TIS-B. This portion of the UAT frame is 800 milliseconds long and is divided into 3200 message start opportunities (MSO) spaced every 250 μs. Each transmitting aircraft transmits exactly one message each second. The MSO at which each aircraft transmits its message is determined based on a pseudo-random selection of one of the 3200 MSOs. The pseudo-random selection is made without receiving or sharing any information as to when other transmitters are transmitting their messages. While this does permit some interference, the goal of the method is to prevent two aircraft from systematically interfering with each other. For a large number of aircraft, however, it is possible that ADS-B messages will interfere with each other much more than was intended.

5.1.2 Probability of Interference at a Single Time Step

For the TDMA structure of the 978 MHz frequency, it is possible to calculate a probability of interference. Given a uniform distribution of the selection of the MSO, the probability that a given transmitter selects a given MSO can be simply determined. For two transmitters, the probability that the two transmitters select the same frequency can also be determined. Since each transmitter selects an MSO without any knowledge of other transmitter's selection, the two selections are independent. Thus the probability that they both select a given frequency is the product of the two probabilities that they individually select that frequency. Given 3200 MSOs the

probability that transmitters A and B simultaneously select MSO_i is

$$\begin{aligned}
\text{P}(\text{A} = \text{MSO}_i) &= \frac{1}{3200} \\
\text{P}(\text{B} = \text{MSO}_i) &= \frac{1}{3200} \\
\text{P}(\text{A} = \text{B} = \text{MSO}_i) &= \left(\frac{1}{3200}\right) \times \left(\frac{1}{3200}\right) \\
&= \frac{1}{3200^2}.
\end{aligned} \tag{5.1}$$

Thus the probability that two transmitters simultaneously transmit on a given frequency is one over the number of MSOs squared. This, however, is only for a given MSO_i. For the probability of interference at any MSO for a given second, we need $\text{P}(\text{A} = \text{B} = \text{MSO}_1 \bigcup \text{A} = \text{B} = \text{MSO}_2 \bigcup ... \bigcup \text{A} = \text{B} = \text{MSO}_{3200})$. This can be calculated by using the equation for a union [33]. Due to the fact that the events $\text{P}(\text{A} = \text{B} = \text{MSO}_i)$ and $\text{P}(\text{A} = \text{B} = \text{MSO}_j)$ are mutually exclusive for all i and j, the intersection of any and all of these events is equal to zero. Thus we are left with the summation

$$\begin{aligned}
&\text{P}(\text{A} = \text{B} = \text{MSO}_1 \bigcup \text{A} = \text{B} = \text{MSO}_2 \bigcup ... \bigcup \text{A} = \text{B} = \text{MSO}_{3200}) \\
&\quad = \text{P}(\text{A} = \text{B} = \text{MSO}_1) + \text{P}(\text{A} = \text{B} = \text{MSO}_2) + ... \\
&\qquad + \text{P}(\text{A} = \text{B} = \text{MSO}_{3200}) \\
&\quad = 3200 \times \frac{1}{3200^2} \\
&\quad = \frac{1}{3200}
\end{aligned} \tag{5.2}$$

This is then the probability that two transmitters transmit on the same MSO at a given second, $\text{P}(\text{A} = \text{B})$. This is the probability that one transmitter interferes with another transmitter.

Now consider a third and fourth transmitter, C and D, where $\text{P}(\text{A} = \text{B}) = \frac{1}{3200}$ and $\text{P}(\text{A} = \text{C}) = \frac{1}{3200}$ and $\text{P}(\text{A} = \text{D}) = \frac{1}{3200}$. To find the probability that A interferes with either B or C or D, we need the union of all the individual probabilities, $\text{P}(\text{A} = \text{B} \bigcup \text{A} = \text{C} \bigcup \text{A} = \text{D})$. This is also

given by

$$\begin{aligned}
&\mathrm{P}(\mathrm{A}=\mathrm{B}\bigcup\mathrm{A}=\mathrm{C}\bigcup A=D)\\
&\quad=\mathrm{P}(\mathrm{A}=\mathrm{B})+\mathrm{P}(\mathrm{A}=\mathrm{C})+\mathrm{P}(\mathrm{A}=\mathrm{D})\\
&\qquad-\mathrm{P}(\mathrm{A}=\mathrm{B})\mathrm{P}(\mathrm{A}=\mathrm{C})-\mathrm{P}(\mathrm{A}=\mathrm{B})\mathrm{P}(\mathrm{A}=\mathrm{D})-\mathrm{P}(\mathrm{A}=\mathrm{C})\mathrm{P}(\mathrm{A}=\mathrm{D})\\
&\qquad+\mathrm{P}(\mathrm{A}=\mathrm{B})\mathrm{P}(\mathrm{A}=\mathrm{C})\mathrm{P}(\mathrm{A}=\mathrm{D}) \qquad (5.3)
\end{aligned}$$

Since each of these probabilities is equal, we let $x=\mathrm{P}(\mathrm{A}=\mathrm{B})=\mathrm{P}(\mathrm{A}=\mathrm{C})=\mathrm{P}(\mathrm{A}=\mathrm{D})=\frac{1}{3200}$. Then Equation (5.3) can be given by $3x-3x^2+x^3$. This is then the expression for the probability that transmitter A is interfered with at one time-step for an environment with four transmitters.

Extending this result to more transmitters, it becomes apparent that the pattern continues. For n transmitters, T, given that the event $\mathrm{T}_0=\mathrm{T}_i$ is stated as E_i

$$\begin{aligned}
\mathrm{P}(I)=&\mathrm{P}(E_1\bigcup E_2\bigcup\ldots\bigcup E_{n-1})\\
=&\binom{n-1}{1}x-\binom{n-1}{2}x^2+\ldots+(-1)^{n-1}\binom{n-1}{n-2}x^{n-2}+(-1)^n\binom{n-1}{n-1}x^{n-1} \qquad (5.4)
\end{aligned}$$

where $\binom{n-1}{i}$ is a combination. This is then the probability that a transmitter T_0 will be interfered with for an environment with n transmitters for a given second, $\mathrm{P}(I_{t_i})$.

Using this formula, however, poses a computational challenge. The combination formula $\binom{n}{k}$ reaches a maximum when $k=\frac{n}{2}$. Thus for a large number of transmitters, $\binom{n-1}{\frac{n-1}{2}}$ is a very large number. For numbers near to this value, computers are unable to represent the value accurately. Additionally it is also possible that the numbers cannot be represented at all. For example $\binom{56}{28}$ is one of the largest combinations that MATLAB can represent accurately, and $\binom{1029}{515}$ is one of the largest combinations that MATLAB can represent at all. Any combination larger than this value is recognized as infinity. Thus if the number of transmitters is greater than 1030 MATLAB cannot compute the probability.

We developed a method to mitigate this using Sterling's approximation for factorials to calculate the combination of large values. Given the combination formula as $\binom{n}{r}=\frac{n!}{r!(n-r)!}$, Sterling's

approximation can be applied to rewrite it as

$$\binom{n}{r} \approx \frac{\sqrt{2\pi n}(\frac{n}{e})^n}{(\sqrt{2\pi r}(\frac{r}{e})^r)(\sqrt{2\pi(n-r)}(\frac{n-r}{e})^(n-r))} \tag{5.5}$$

Taking the $\log_n$ reduces the formula to be

$$\begin{aligned}\log_n \binom{n}{k} \approx & \frac{1}{2} + n - n\log_n(e) - \frac{1}{2}\log_n(r) - r\log_n(\frac{r}{e}) \\ & - \frac{1}{2}\log_n(2\pi(n-r)) - (n-r)\log_n(\frac{n-r}{e})\end{aligned} \tag{5.6}$$

Using this formula the computation of very large combinations is possible. Due to the fact that Sterling's approximation is most accurate for large factorials, smaller factorials are best calculated by traditional methods. Also, at very large factorials, there is still some numerical instability in the method. Thus, it should be used with caution. That being said, the numerical instability is notably less than that of traditional combination methods. As a result it is sufficient for our calculations.

With Equations (5.4) and (5.6) it is possible to calculate the probability that a given transmitter is interfered with at single time step for a given number of transmitting aircraft.

5.1.3 Probability of Trackability

Using the probability of interference for a given transmitter at a single time step and several key characteristics of tracking/estimating methods, it is possible to determine the probability of starting and maintaining a track for any given aircraft. We refer to this probability as the probability of trackability.

Prior to presenting the method to calculate the probability of trackability, it is necessary to identify several terms. To initialize a track with any estimator, it is necessary to receive a set number of measurements in a set amount of time. Since ADS-B messages do not require data association, a track can be formed from just two measurements. The maximum set size is the maximum number of measurements that can be missed between two received measurements and allow them to still form a track. In other words, if four measurements can be missed between two good measurements and the two good measurements can still be used to form a track, then the maximum set size is six. Thus two out of six messages must be received to form a track. For the

KF-NCV described in Chapter 3, this value can be determined using the initial value of the process covariance, the measurement covariance, the Mahalinobis gate size, and the maximum expected speed of an intruder.

Another key term is the number of missed measurements to terminate a track. This is the maximum number of measurements, after a track already exists, that can be missed before the track is declared as invalid. This value is dependent upon the covariance of the track, but a nominal value can be determined by taking the initial track covariance and propagating it forward without measurement updates until the covariance becomes so large that the track is terminated. The number of times that the track was propagated into the future is the number of missed measurements to kill a track.

Due to the fact that the MSO for a given transmitter is selected on a psuedo-random basis each second, the probability of interference for a given second is independent from the probability of interference for a different second. Using this fact, the probability that consecutive measurements are interfered with is $\mathrm{P}(I_{t_1} \cap I_{t_2}) = \mathrm{P}(I_{t_1})\mathrm{P}(I_{t_2})$. Assuming that the number of transmitting aircraft remains the same between the two consecutive seconds, the probability remains the same, and thus the probability simplifies to $\mathrm{P}(I_{t_1} \cap I_{t_2}) = \mathrm{P}(I_{t_1})^2$. This can be extended to more than just two consecutive seconds. In the case of tracking/estimation of intruders, the maximum set size and the number of missed measurements to terminate a track dictate how many measurements can be missed before tracking becomes unreliable. For the case of the maximum set size, if two measurements are not received in that set then the track cannot be formed. Thus the probability of forming a track is $\mathrm{P}(T_{\mathrm{form}}) = 1 - \mathrm{P}(I_{t_1})^{MaxSetSize-1}$. For the number of missed measurements to kill a track, at least one measurement must be received in the set. Thus the probability of maintaining a track is $\mathrm{P}(T_{\mathrm{maintain}}) = 1 - \mathrm{P}(I_{t_1})^{NumMissMeastoKillTrack}$.

These two probabilities, the probability to form a track and the probability to maintain a track, determine the robustness to missed measurements of a given tracker for a given number of transmitting aircraft. The overall probability of trackability is the lesser of these two probabilities. If either a track cannot be formed reliably or a track cannot be maintained reliably then the tracker is unable to track reliably. Thus $\mathrm{P}(T) = \min(\mathrm{P}(T_{\mathrm{form}}), P(T_{\mathrm{maintain}}))$. The metric that leads to the minimum probability is referred to as the limiting tracking variable (LTV).

5.1.4 Key Parameters

As previously shown the probability of trackability is a function of many variables, but it can be reduced to a function of two variables. The full list of fundamental variables for the probability of trackability are as follows:

- Range
- Density
- Intruder speed
- Mahalinobis gate size
- Track covariance gate size
- Time between measurements
- Filter matrices (A,C,P,Q,R)

Varying any of these parameters results in a change in the probability of trackabaility. These variables, however, can be formulated into two variables that fully describe the probability of trackability. The range and density combine to determine the total number of aircraft with in the visible region. The speed of the intruder, time between measurements, filter matrices, the Mahalanobis gate size, and track covariance gate size are necessary only to determine the maximum set size and the number of measurements necessary to kill a track. As previously stated, the smaller value between maximum set size and the number missed measurements to kill a track is the LTV. Thus the probability of trackability is actually a function of only the number of aircraft and the probability of trackability.

5.1.5 Simulations

To test and demonstrate the probability of interference and the probability of trackability, we created several key plots and simulations. The first three plots show the relationships between key variables and the probability of interference and the probability of tracking. The fourth plot

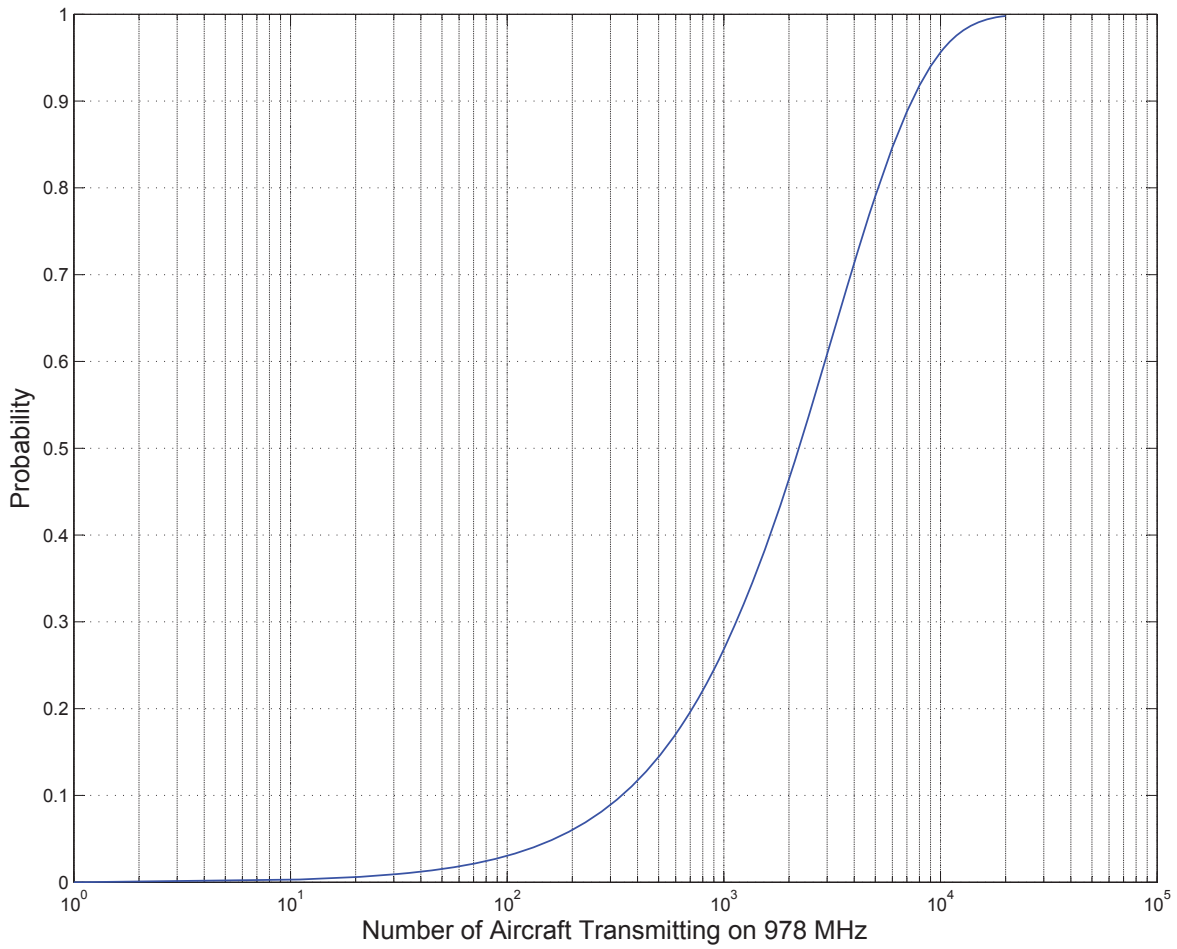

Figure 5.1: Probability of interference as a function of the number of transmitting aircraft.

shows the results of a simulation in which we simulate the interference of individual intruders as we gradually increase the ADS-B transmit range of the intruders.

The first plot, shown in Figure 5.1, shows the probability of interference as a function of the number of transmitting aircraft. This plot provides important perspective on the number of ADS-B-equipped aircraft that would lead to significant levels of interference. While the values represented on the horizontal axis of Figure 5.1 are large, it is not impossible that future airspace conditions would have several thousand aircraft operating at the same time in the same region.

Figure 5.2 provides a different perspective on the probability of interference. Each of the lines on the plot corresponds to a transmit range. The horizontal axis represents increasing density. With the density and transmit range, the number of transmitting aircraft can be calculated. It is important to note that in calculating the number of aircraft from the density and transmit range we

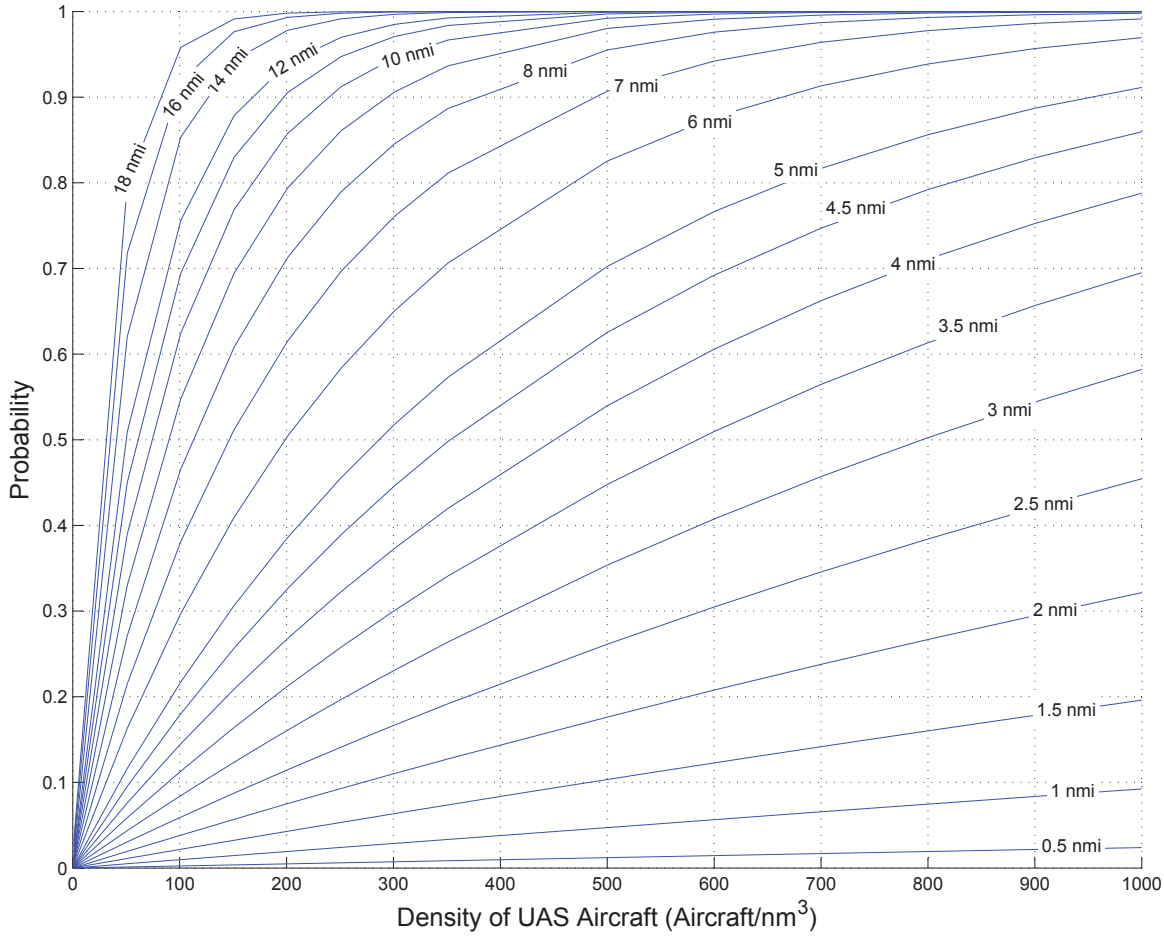

Figure 5.2: Probability of interference for different transmit ranges as a function of the density of aircraft.

use the cube of the the transmit range. Thus an increase in transmit range impacts the number of transmitting aircraft much more than an increase in the density does. This fact alludes to an important trade off between ADS-B transmit range and the level of interference that will be explored more thoroughly in subsequent plots.

Figure 5.3 demonstrates the relationship between the number of transmitting aircraft, the limiting tracking variable, and the probability of trackability. The black line shown in Figure 5.3 is the point on the graph where the probability of trackability dips below 0.999999. This line is a threshold at which any intruder can be tracked with great reliability. It is important to note in the figure the relationship between the number of transmitting aircraft and the LTV. For a small LTV, the estimator can only tolerate a low level of interference. For a larger LTV, the estimator can tolerate a much higher level of interference. Thus an important takeaway from Figure 5.3 is that

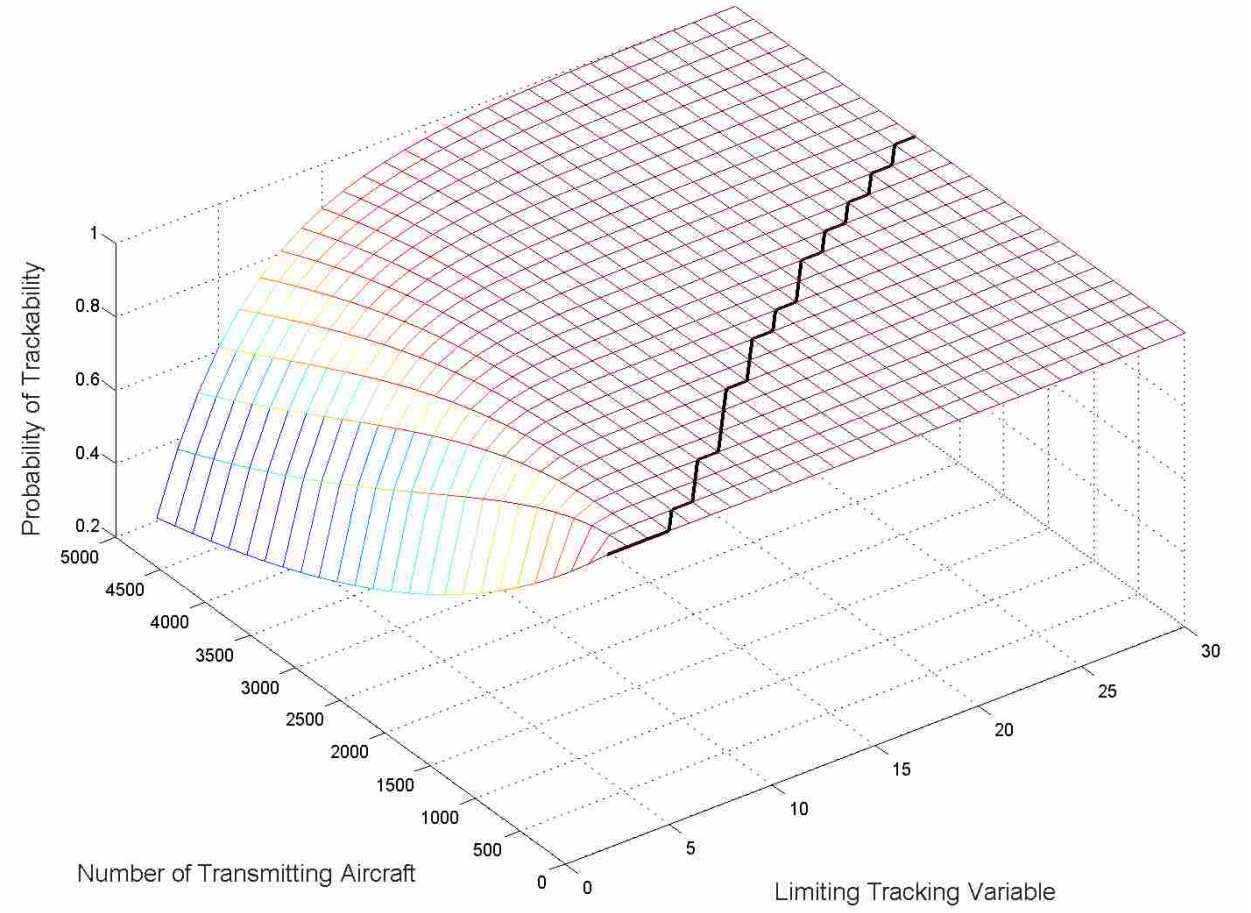

Figure 5.3: Probability of trackability as a function of the number of intruders and the limiting tracking variable.

a robust estimation scheme significantly increases the amount of ADS-B interference that can be tolerated while still maintaining effective intruder tracking.

Figure 5.4 presents the results of a simulation that highlights the importance of estimating intruder states and the limitations that increased transmit range imposes on intruder visibility. To create Figure 5.4, we generate a large set of intruders uniformly distributed over a cube with a set density. Then we vary the ADS-B transmit range linearly. For each transmit range, we determine the number of intruders that are within range and calculate the probability of interference. With the probability of interference we sample a uniform distribution to determine which intruders have been interfered with and are thus invisible at that time step. We also calculate which intruders we are tracking. With the list of total intruders, intruders in range, visible intruders, and the tracked intruders, we calculate key statistics to determine the visibility and trackability of the intruders.

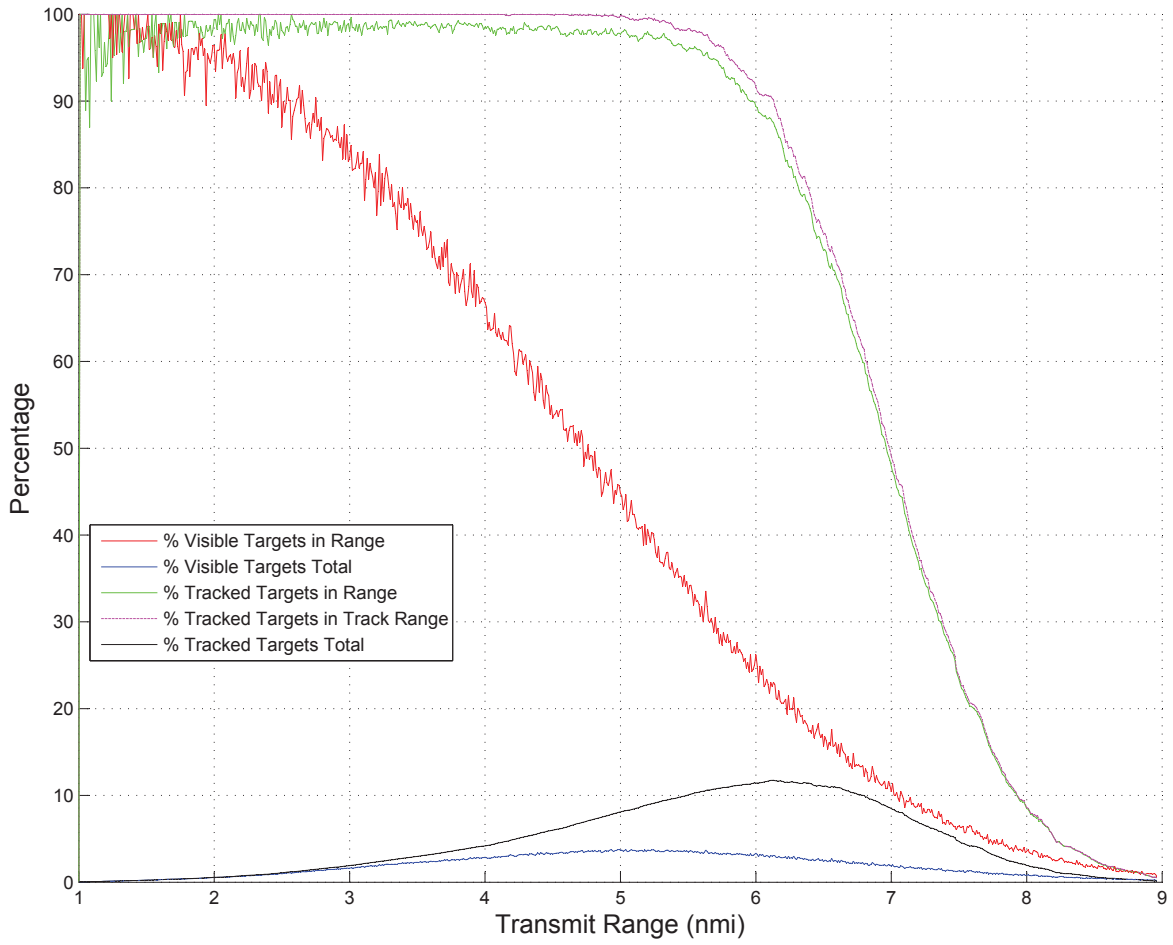

Figure 5.4: How the probability of interference and the probability of trackability change with increasing range. It also demonstrates the impact of those metrics on the overall detectability of intruders.

In Figure 5.4 there are five lines. The red line shows the percentage of targets that are within range that are also visible at a given transmit range. The green line shows the percentage of targets that are in range and trackable for a given transmit range. It is interesting to note that the green line is always less than one, even for very short transmit ranges. This is a result of intruders moving into and out of the visible region. As an intruder enters the visible region, it takes several time steps to initialize a track. During that initialization period the aircraft is in range, but it is not trackable. To determine a range at which all intruders should be trackable, we define a region slightly smaller than the visible region by which point all tracks should have been able to initialize. The pink line shows the percentage of intruders within the smaller region that are trackable. As would be expected the pink line remains a 100% until the interference becomes very high. The

blue and black lines show the percentage of total intruders that are in the simulation, within range and outside the range, that are visible and trackable respectively.

Figure 5.3 illustrates several important principles of ADS-B interference. As previously mentioned tracking of intruders significantly increases the amount of interference that an ADS-B-based DAA system can tolerate. This can be seen in the disparity between the red and green lines. The red line drops below 90% visibility at approximately 2.5 nmi. The green line, however, is able to maintain 90% trackability until 6 nmi. This is a significant increase in the ability of an ownship to detect intruders. Essentially at a transmit range of 2.5 nmi, a DAA system without intruder tracking is only capable of knowing the position and velocity of 90% of intruders with in the 2.5 nmi range. A DAA system with intruder tracking, on the other hand, is capable of knowing the position and velocity of 90% of the intruders upto a transmit range of 6 nmi.

Another key takeaway is that once an intruder enters the visible range, there is an initialization period before that intruder can be accurately tracked. This fact is seen in the difference between the pink and green lines. While the initialization distance for new tracks is very small compared to the transmit range, the difference between the transmit range and the tracking range has important implications for analyses of the necessary transmit range to allow for conflict/collision avoidance. These implications will be explored later on in this chapter.

One of the most important takeaways from Figure 5.4 is the distinctive peak in both the blue and black lines. Initially, it seems that as the transmit range increases the number of visible/trackable targets should also increase. Stated otherwise, the farther that the ownship can see the more intruders it can see. The peak in the blue and black lines indicate that this is not the case. As the transmit range increases, the number of transmitting aircraft in range also increases. Thus there is in reality a point at which the number of aircraft in range becomes so large that the interference rises to a level that actually reduces the visibility/trackability of the targets in range. Thus if all aircraft are transmitting ADS-B too far, then the overall visibility/trackability is reduced to levels below that of shorter transmit ranges. This is a very significant result, and it shows that too much ADS-B transmit power can reduce the capability of a DAA system.

5.2 ADS-B Congestion Conclusions

In summary of the presented analyses and results, the probability of interference is a function of the number on transmitting aircraft. It can also be expressed as a function of transmit range and aircraft density. In such a formulation, the probability of interference is significantly more sensitive to changes in the transmit range than the density. The probability of trackability is the probability that a track for an intruder can be maintained, and it can be expressed as a function of the number of transmitting aircraft and the limiting tracking variable. A larger limiting tracking variable allows a DAA to accommodate a much higher level of interference and thus improve the probability of trackability. In the probability of interference and probability of trackability simulation, we illustrated three key takeaways. The importance of tracking intruders rather than simply relying on the regularity of ADS-B measurements was demonstrated. Also it was clear that there is a track initialization range for intruders wherein they are in the visible range but are invisible to the DAA system. Finally we demonstrated that there is a point of diminishing returns with regards to transmit range. It is possible to transmit so far that the visible range includes enough transmitting aircraft that the DAA has less visibility of the surrounding intruders than it would if the transmit range was smaller. The results are important conclusions and represent a basis for evaluating the viability of proposed self-separation threshold and well clear definitions.

CHAPTER 6. DEFINING MAXIMUM SELF-SEPARATION THRESHOLD AND WELL CLEAR DEFINITIONS

For high-density airspace with a large number of small UAS, the possibility of ADS-B interference presents a unique challenge to maintaining well clear. As explained in Chapter 1, maintaining WC requires detection of intruders at long-ranges. In Chapter 5 we demonstrated that long-range ADS-B transmissions can cause an excessively high level of message interference that limits the capability of ADS-B to detect intruders. Thus it is necessary to examine the the proposed self-separation threshold and well clear definitions from a system-design perspective to determine whether such definitions are suitable and achievable for current airspace regulations and anticipated small UAS densities.

The objective of this chapter is to provide a maximum achievable SST and WC definition for high-density airspace with ADS-B-equipped small UAS. The methodology presented here also represents a tool with which proposed SST and WC definitions can be evaluated. Additionally, this chapter couples the proposed tool with equations that specify the minimum necessary detection range to avoid NMAC for small UAS. These two tools result in an upper and lower bound for WC definitions. Thus the chapter concludes with a recommendation for WC for small UAS.

6.1 Upper WC Bound Analysis Method

Figure 6.1 shows the method and variables to evaluate the viability of SST and WC definitions in high-volume airspace. In the figure the green blocks are the design variables. The tan blocks are intermediate calculations, and the blue blocks are key results. Given a desired probability of trackability and the number of measurements necessary to maintain a track, the LTV, the probability of interference at any time step can be calculated. From the probability of interference, the number of transmitting aircraft can be determined. Since the formula for the probability of interference shown in Equation (5.4) does not have an explicit solution for the number of aircraft,

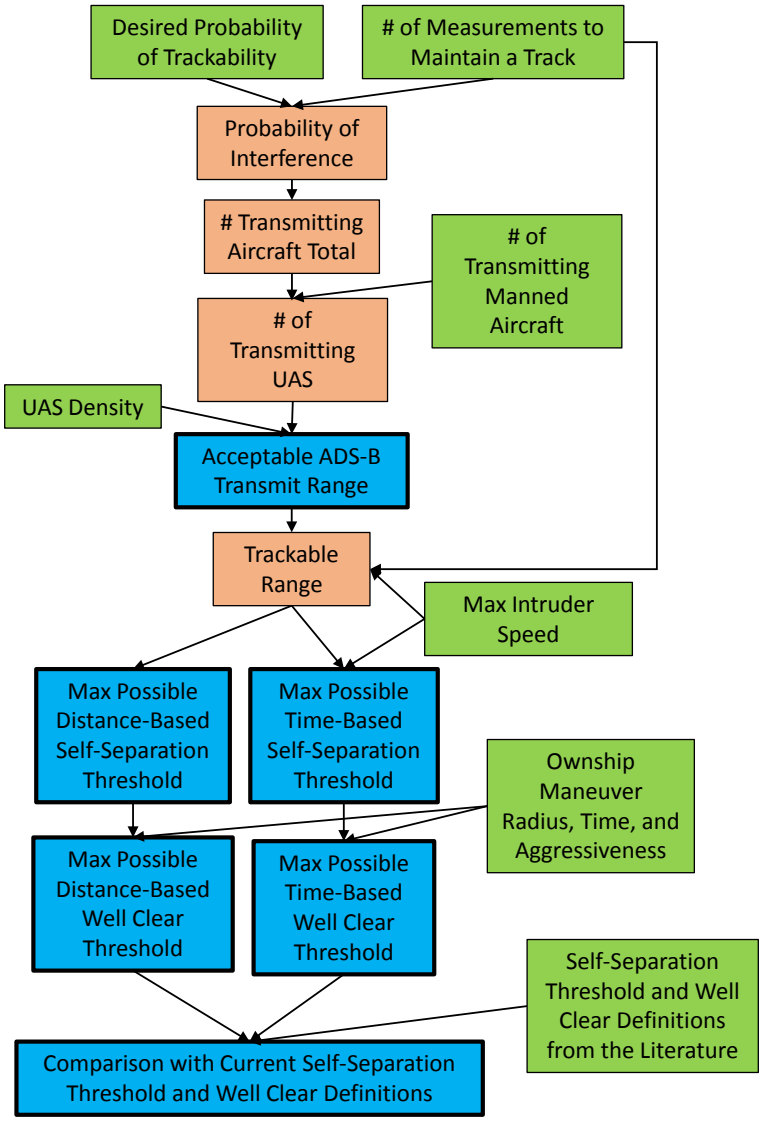

Figure 6.1: Variables and method by which SST and WC definitions can be evaluated.

we use a root-finding method to determine this value. The total number of aircraft, the number of manned aircraft, and the maximum expected UAS density can be used to determine a maximum acceptable ADS-B transmit range. By identifying the maximum expected intruder speed and the amount of time needed to initialize a track, the trackable range can be determined. The trackable range is the maximum distance at which all intruders can be tracked with the desired probability of trackability, and thus it is the maximum possible distance-based SST definition. This definition can be mapped into a time-based definition using the maximum expected intruder speed and a time metric. We then assume that the ownship maneuvers as soon as the intruder is detected. With

the minimum turn radius of the ownship, the ownship speed, and the intruder maximum speed, it is possible to determine the closest distance and time that the ownship and intruder will ever come. This distance and time are then the maximum achievable well clear distance and time respectively. The SST and WC definitions determined in this model are the maximum achievable definitions. Definitions larger than these are unreasonable in that the ownship cannot detect intruders at distances greater than the calculated SST and that the ownship cannot maneuver sufficiently to maintain larger distance or time WC definitions.

Airspace conditions for high-density small UAS operations are unknown. To build the model in Figure 6.1, it is necessary to make several assumptions about future airspace conditions. The methods and reasoning for key model details and assumptions are laid out in the following sections.

6.1.1 Estimating Future UAS Density

One of the first estimates necessary for the maximum SST/WC model is the density of future airspace. To determine this density, we estimated the number of small UAS that will be employed in a given region for each of the various small UAS applications. For this estimate, we selected Chicago, Illinois as our region based on the high volume of manned aircraft operations and the high population density. According to `yellowpages.com`, there are approximately 1000 pizza shops in Chicago. We assume that at any one time 10% of them will use UAS for deliveries. Additionally there are approximately 500 take-out Chinese restaurants, and 300 other sandwich or food delivery restaurants in Chicago. We assume that at any one time $\frac{1}{8}^{th}$ of them will use UAS for deliveries. To account for anticipated package delivery operations, we assume that there are approximately 200 UAS operations for package delivery at one time. This includes Amazon, Google, USPS, FedEx, UPS, DHL, and other courier type activities. Aerial photography applications will also contribute to the density of small UAS. We assume that during peak times 200 small UAS will be employed for aerial photography applications such as real estate advertising, sporting events, follow-me applications, and news agencies. Finally, we project that there will be 200 UAS operations for law enforcement, traffic monitoring, and infrastructure monitoring applications. The sum of these estimates results in 800 small UAS operating over Chicago at peak times.

It is also necessary to estimate the number of manned aircraft operations due to the fact that these aircraft will contribute to the ADS-B congestion. Between O'Hare International Airport (ORD) and Midway Airport (MDW), there were approximately 1,131,185 aircraft operations in 2014 [48, 49]. Even though many of the aircraft operating out of ORD and MDW will be transmitting on the 1090 MHz ADS-B frequency, they will require bandwidth on 978 MHz frequency due to TIS-B and ADS-R. Thus all aircraft operations from both O'Hare and Midway airports will be reflected on 978 MHz ADS-B. The average rate of departure and arrival of aircraft between the two airports is 128 per hour. Assuming a 100 nmi transmit range for each manned aircraft and a 250 knot average speed, at any one time there are approximately 45 aircraft in range of the city. The combination of UAS and manned aircraft results in 845 transmitting aircraft in Chicago. Of those 845 aircraft, 45 are manned aircraft and 800 are UAS.

To complete the air traffic density calculations, several additional facts and assumptions are necessary. First we assume that the UAS are flying below 400 ft. This is an altitude that will meet or exceed the needs for almost all small UAS applications, and it is the current focus range for the UAS Traffic Management (UTM) System [50]. We further assume that the operating UAS are spread out uniformly over the city and that the UAS operate within the limits of the city. It is necessary to note that the area of Chicago is 176.6 nmi^2. With this information, we can calculate a UAS density. Given the area of the city and the operational altitude, the volume of operation is 58.1 nmi^3. With that volume and the number of transmitting aircraft, the anticipated density of transmitting aircraft becomes 14.5 aircraft/nmi^3, and the density of small UAS is 13 aircraft/nmi^3.

6.1.2 Determining an Appropriate Transmit Range

Another important aspect of the model in Figure 6.1 is the method used to determine an appropriate ADS-B transmit range for small UAS. In this method we first look to the probability of trackability and the limiting tracking variable. The probability of interference for a given probability of trackability can be calculated with the relationship given in Section 5.1.3 by

$$P(Interference) = \sqrt[LTV]{(1 - P(Trackability))}$$

where LTV is the limiting tracking variable. With the probability of interference, it is necessary to determine the number of transmitting aircraft that lead to this probability of interference. Due to the lack of an explicit equation for the number of aircraft from the probability of interference, we determine the number of transmitting aircraft with a bisection root-finding method. With the number of aircraft and the previously determined density, the transmit range can be identified. Since the number of manned aircraft is assumed to be constant regardless of UAS transmit range, we subtract the number of manned aircraft from the total number of transmitting aircraft. This results in the number of UAS that can be transmitting within range of the ownship. Due to the fact that the UAS are assumed to operate below 400 ft, the transmit range is determined by calculating the radius of a disk that is 400 ft thick. This transmit range is then the maximum acceptable range for ADS-B transmissions that will result in the desired probability of trackability.

It is important to note that this transmit range is only intended to apply to small UAS. Current FAA regulations dictate the transmit power, and consequently nominal range, of manned aircraft. Furthermore, the transmit range of small UAS will not significantly affect the ability of manned aircraft to track intruders. Provided that manned aircraft also have an efficient tracking method with parameters similar to those assumed for small UAS, the probability with which manned aircraft can track intruders will be very similar to the probability of trackability specified for small UAS.

6.1.3 Calculating a Maximum Self-Separation Threshold

The maximum self-separation threshold can be determined from the maximum tracking range. The maximum tracking range can be determined by taking the maximum acceptable transmit range and reducing it by the distance, and implicitly the time, required to initialize a track of the fastest expected target. Furthermore, the maximum tracking range is the maximum range at which tracking of all intruders can be guaranteed to the desired probability of trackability. Since this is the range at which essentially all targets can be tracked, it is reasonable to make this range the maximum self-separation threshold distance. Larger definitions of the SST are superfluous in that the ownship cannot reliably detect intruder small UAS at that range. In detailing the value for the maximum self-separation threshold, a time-based definition must also be considered. Using the ownship speed, the maximum speed of an intruder, the maximum tracking range, and an ap-

propriate time metric, a time-based SST definition can be calculated from the distance-based SST definition.

6.1.4 Calculating a Maximum Well Clear Definition

With a maximum possible distance and time-based SST definition, it is possible to define a maximum possible WC definition. The maximum WC definition can be determined by calculating the minimum distance and time between the ownship and intruder over the course of an evasive maneuver by the ownship. If the WC definition is smaller that this minimum distance or time, then the ownship will not be able to maintain WC.

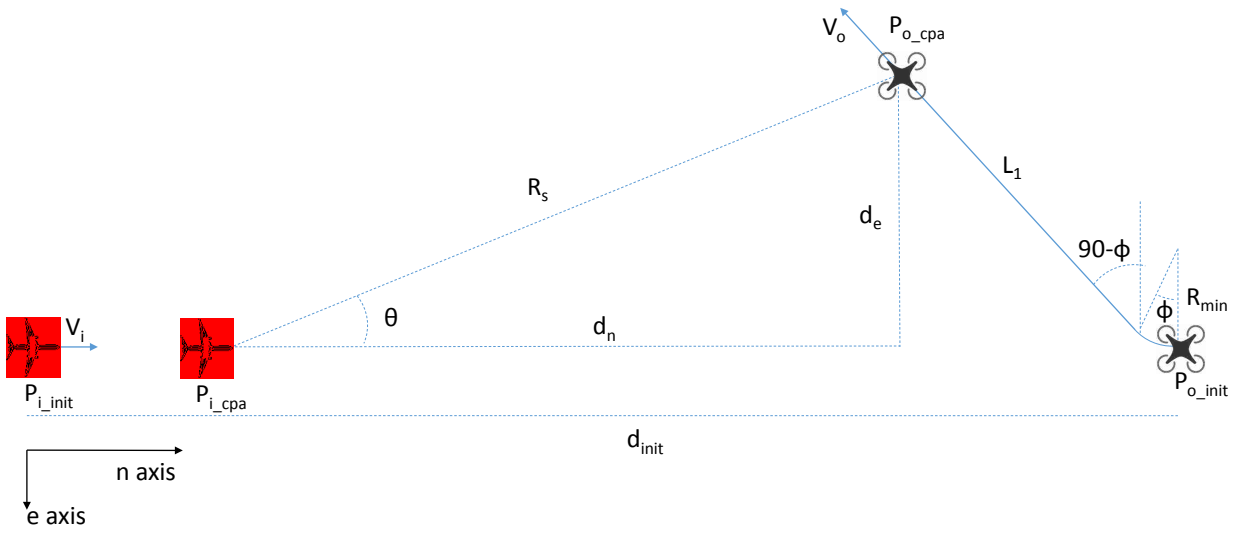

Figure 6.2: A parameterized maneuver by an ownship to maintain self-separation from a head-on intruder.

Figure 6.2 shows the geometry of an evasive maneuver in a head-on collision scenario. The ownship, represented by a multirotor, turns as tightly as possible and then continues on in a straight line. The intruder maintains a straight path as though it were oblivious to the multirotor. In Figure 6.2, d_{init} is the distance between the two aircraft at the time of the maneuver. ϕ is the degree by which the ownship changes course, and R_{min} is the minimum turn radius achievable by the ownship. d_n and d_e are the distance between the intruder and ownship at the closest point of

approach in the n and e directions respectively. P_i and P_o are the positions of the intruder and ownship. Finally, R_s and θ are the closest point of approach and the angle as shown in the figure.

Determining the Minimum Distance Between an Intruder and Maneuvering Ownship

In identifying the minimun distance between the ownship and the intruder, the starting distance between the two aircraft, d_{init}, is the maximum SST from the previous section. The initial positions and velocities of the ownship and intruder are also known by virtue of using ADS-B as the sensor. As a result of these known values,the first step in determining the minimum distance between the ownship and the intruder is to identify the minimum turn radius of the ownship. To do this we assume that the multirotor has an intial forward velocity going into the turn. The velocity is maintained while also ensuring that the north axis of the body frame of the multirotor is pointing in the direction of travel of the multirotor throughout the turn. We further assume that the multirotor does not change altitude over the course of the turn thus the flight path angle is zero.

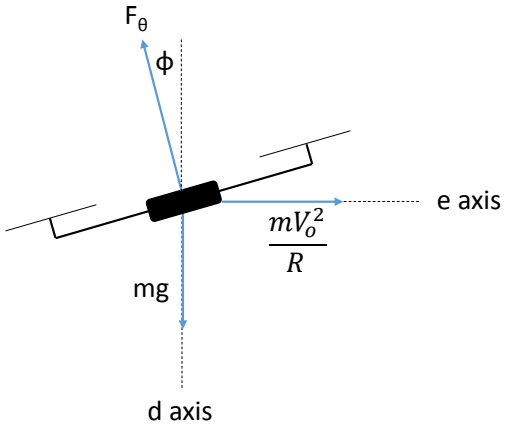

Figure 6.3: A free body diagram of a turning multirotor. The multirotor is pitched forward θ for level flight such that $F_\theta = F_{thrust}\cos\theta$.

Following the same methodology given by Beard and McLain [16] to derive the minimum turn radius, the force balance for Figure 6.3 is

$$\begin{aligned} F_\theta \sin\phi &= m\frac{V_o^2}{R} \\ F_{thrust}\cos\theta\sin\phi &= m\frac{V_o^2}{R} \\ &= mV_o\dot{\chi} \end{aligned} \tag{6.1}$$

for the east axis and

$$\begin{aligned} F_\theta \cos\phi &= mg \\ F_{thrust}\cos\theta\cos\phi &= mg \end{aligned} \tag{6.2}$$

in the negative down axis. Dividing Equation (6.1) by Equation (6.2) and solving for $\dot{\chi}$ yields

$$\begin{aligned} \frac{F_{thrust}\cos\theta\sin\phi}{F_{thrust}\cos\theta\cos\phi} &= \frac{mV_o\dot{\chi}}{mg} \\ \dot{\chi} &= \frac{g}{V_o}\tan\phi. \end{aligned} \tag{6.3}$$

Since

$$R = \frac{V_o\cos\gamma}{\dot{\chi}} \tag{6.4}$$

and $\gamma = 0$,

$$\frac{g\tan\phi}{V_o} = \frac{V_o}{R}. \tag{6.5}$$

Solving Equation (6.5) for R results in

$$R_{min} = \frac{V_o^2}{g \tan \phi}. \tag{6.6}$$

Thus Equation (6.6) shows that the minimum turn radius for a multirotor is identical to the coordinated turn equation for fixed-wing aircraft where V_o is the initial velocity of the ownship. The rest of the analytic solution to the minimum closest point of approach is an extension of work done to determine the necessary sensing range for a small UAS.

Taking P_{i_cpa} as the origin, the closest point of approach between the two aircraft shown in Figure 6.2 is

$$0 = \frac{(R_s \cos\theta, R_s \sin\theta) - (0,0)}{||(R_s \cos\theta, R_s \sin\theta) - (0,0)||} - [(-V_o \sin\left(\frac{\pi}{2} - \phi\right), V_o \cos\left(\frac{\pi}{2} - \phi\right)) - (V_i, 0)]. \tag{6.7}$$

Solving for $\tan\theta$ results in

$$\tan\theta = \frac{V_o \cos\phi + V_i}{V_o \sin\phi} \tag{6.8}$$

$$= \cot\phi + \frac{V_i}{V_o \sin\phi}. \tag{6.9}$$

Using the relationships shown in Figure 6.2,

$$t_{arc} = \frac{\phi R_{min}}{V_o} \tag{6.10}$$

$$t_l = \frac{L_1}{V_o} \tag{6.11}$$

$$\tan\theta = \frac{d_e}{d_n} \tag{6.12}$$

$$d_n = d_{init} - (t_{arc} + t_l)V_i - R_{min} \sin\phi - L_1 \cos\phi \tag{6.13}$$

$$d_e = R_{min}(1 - \cos\phi) + L_1 \sin\phi. \tag{6.14}$$

Using these equations and Equation (6.8),

$$\frac{V_o\cos\phi+V_i}{V_o\sin\phi}=\frac{R_{min}(1-\cos\phi)+L_1\sin\phi}{d_{init}-(\phi R_{min}+L_1)\frac{V_i}{V_o}-R_{min}\sin\phi-L_1\cos\phi}. \tag{6.15}$$

Solving for L_1 yields

$$L_1=\frac{\left(\frac{V_o\cos\phi+V_i}{V_o\sin\phi}\right)(d_{init}-\phi R_{min}\left(\frac{V_i}{V_o}\right)-R_{min}\sin\phi)-R_{min}(1-\cos\phi)}{\left(\frac{V_o\cos\phi+V_i}{V_o\sin\phi}\right)\left(\frac{V_i}{V_o}\right)+\left(\frac{V_o\cos\phi+V_i}{V_o\sin\phi}\right)\cos\phi+\sin\phi}. \tag{6.16}$$

By using in the value for L_1 to solve for d_n and d_e using Equations (6.13) and (6.14), the closest point of approach between the two aircraft can be calculated with the Euclidean distance formula,

$$R_s=\sqrt{d_n^2+d_e^2}. \tag{6.17}$$

This result, R_s, is then the minimum distance between a straight-line intruder and a maneuvering ownship that maintains its speed and changes is course by ϕ.

Determining the Minimum Time Between an Intruder and Maneuvering Ownship

With the minimum distance between an intruder and maneuvering ownship, it is necessary to determine how close the intruder will come to the ownship in terms of time. The time metric that we use is τ_{DMOD}. This is the metric used in TCAS and it is a robust time metric. As the formula for calculating τ_{DMOD} is non-differentiable there is no analytical solution to the minimum time metric. We assume that the ownship maneuvers as shown in Figure 6.2. As previously stated, this is a function of the intruder speed V_i, the ownship speed V_o, the maximum detection distance R_{init}, the course change ϕ, and the ownship minimum turn radius R_{min}. To calculate the minimum time between the ownship and intruder, we use a simulation-based method to model the motion of both aircraft over the course of the encounter. Figure 6.2 illustrates the worst-case, head-on scenario

considered in this simulation. The intruder position, (p_{i_n}, p_{i_e}), is modeled by

$$\dot{p}_{i\_n} = v_{i\_n}$$
$$\dot{p}_{i\_e} = v_{i\_e}.$$

The ownship position, (p_{o_n}, p_{o_e}), can be modeled by

$$\dot{p}_{o\_n} = v_{o\_n}$$
$$\dot{p}_{o\_e} = v_{o\_e}$$

where

$$v_{i\_n} = -V_i$$
$$v_{i\_e} = 0$$
$$v_{o\_n} = \begin{cases} V_o \sin(\theta) & 0 \leq \theta \leq \frac{\pi}{2} \\ V_o & \frac{\pi}{2} < \theta \end{cases}$$
$$v_{o\_e} = \begin{cases} V_o \cos(\theta) & 0 \leq \theta \leq \frac{\pi}{2} \\ 0 & \frac{\pi}{2} < \theta \end{cases}$$
$$\dot{\theta} = \frac{V_o}{R_{min}}.$$

From the intruder and ownship positions and velocities, it is possible to calculate a relative position and velocity at a given time step. These are given by

$$p_r = (p_{i\_n}, p_{i\_e}) - (p_{o\_n}, p_{o\_e})$$
$$v_r = (v_{i\_n}, v_{i\_e}) - (v_{o\_n}, v_{o\_e}).$$

The minimum time between the two aircraft over the course of the maneuver is the minimum value of time metric from the set of time metrics calculated over the course of the simulation. This value is then the maximum possible well clear time definition. The maximum possible well clear

distance is the minimum distance between the intruder and ownship in this worst-case scenario. Thus the maximum achievable well clear distance is the distance calculated in Equation (6.17).

6.2 Lower WC Bound Analysis Method

The minimum WC boundary for small UAS is key to determining a WC boundary for small UAS. The methodology to determine the minimum WC boundary is similar to that used to determine the maximum boundary.

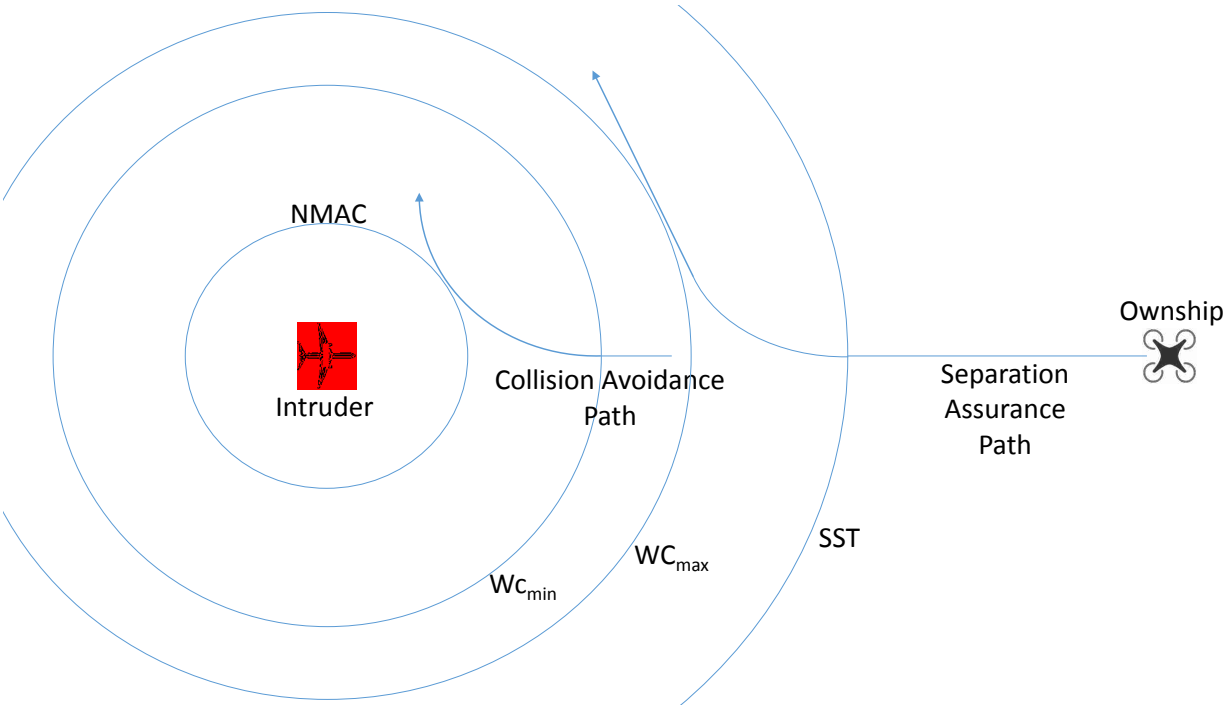

Figure 6.4: The methodology used to determine both the upper and lower WC bounds.

Figure 6.4 shows the methodology used to determine both the upper and lower WC bounds. As previously explained the upper bound is determined by the maximum distance that a maneuvering ownship can maintain from an intruder in the presence of ADS-B frequency congestion. The lower WC bound is determined by assuming that the ownship does not manuever when it first detects the intruder. Rather the ownship waits to manuever until it is just barely able to avoid the intruder NMAC volume through its maneuver. In other words the minimum WC boundary is clos-

est that two aircraft can get before an NMAC is guaranteed. This section focuses on calculating the lower WC boundary.

In calculating the lower WC boundary there are two cases to consider. The first case occurs when $R_{min} < R_{NMAC}$, and the second case occurs when $R_{min} > R_{NMAC}$. These two cases each yield different equations. The minimum WC for case one is

$$d_{minWC} = \frac{1}{V_o}\left(\frac{V_o^2(V_o + (\pi/2-1)V_i}{g\tan\phi} + R_{NMAC}\sqrt{V_o^2+V_i^2}\right). \tag{6.18}$$

The equation for case two is

$$\begin{aligned} d_{minWC} = &\sqrt{R_{NMAC}\sin\theta(2R_{min} - R_{NMAC}\sin\theta)} \\ &+ \frac{V_i}{V_o}\left(R_{min}\cos^{-1}\left(\frac{R_{min} - R_{NMAC}\sin\theta}{R_{min}}\right)\right) + R_{NMAC}\cos\theta \end{aligned} \tag{6.19}$$

where θ is calculated using a bisection method on

$$0 = \frac{V_o\sin\theta\sqrt{R_{NMAC}\sin\theta(2R_{min} - R_{NMAC}\sin\theta)}}{R_{min}} - \left(\frac{V_o(R_{min} - R_{NMAC}\sin\theta)}{R_{min}} + V_i\right)\cos\theta. \tag{6.20}$$

Equations (6.18) and (6.19) calculate the distance necessary to ensure that an ownship can maneuver sufficiently to avoid the NMAC volume of an intruder. Thus, d_{minWC} is the minimum WC distance for small UAS. The time-based minimum WC definition is determined in the same way as the maximum WC definition, but R_{NMAC} is used in the τ_{DMOD} equation rather than the maximum WC definition.

6.3 Simulation Results

This section shows the results of a series of calculations/simulations wherein we determine the maximum and minimum acceptable SST and WC definitions for a given set of parameters. We start by demonstrating and exercising the model presented in Figure 6.1. Then we couple the

minimum WC definitions from Section 6.2 to create a well clear recommendation for small UAS. In both the maximum and minimum WC analysis we use τ_{DMOD} as the time metric. This is the metric used by both TCAS and other leading WC recommendations for larger aircraft [23]. τ_{DMOD} is a modified time to collision and is given by

$$\tau_{DMOD} = \begin{cases} -\frac{(r^2 - HMD^2)}{r\dot{r}} & CPA \leq HMD \\ \infty & CPA > HMD \end{cases}. \tag{6.21}$$

In Equation 6.21 r and $\dot{r}$ are the range and range rate between the intruder and ownship respectively. Additionally both the maximum and minimum WC definitions rely on a set of several parameters. These parameters are given in Table 6.1.

Table 6.1: Key parameters for SST and WC definition evaluation.

Parameter	Value
Intruder Speed	250 kt
Probability of Trackability	0.999999
Message Start Opportunities	3200
UAS Density	13.77 UAS/nmi^3
UAS Type	Multirotor
Ownship Bank Angle	40 deg
Ownship Course Change	90 deg
Lift-to-Weight Ratio	1.5
HMD Value	0.65 nmi
Max UAS Altitude	0.0658 nmi (400 ft)
Limiting Tracking Variable	11

The initial values of the parameters in Table 6.1 are designed to closely match the operational characteristics of current airspace. This scenario serves as a baseline with which all other calculations can be compared. Table 6.1 shows the baseline values of the key parameters. The upper group of parameters in Table 6.1 are those parameters that will be varied in the subsequent analysis, and the lower group of parameters are those parameters that are not expected to change.

6.3.1 Maximum WC Model

To demonstrate the maximum SST and WC method in Figure 6.1, we analyzed a WC definition proposed by the Sense and Avoid Science Research Panel (SARP) based on a rigorous set of simulations and testing [23]. The method defines the distance threshold and HMD to be 0.6583 nmi (4000 ft) and the time-based threshold to be $\tau_{DMOD} = 35$ s. The SST that we examine in our analysis was proposed by NASA Ames Research Center and is $\tau_{DMOD} = 90$ s and distance and HMD of 0.6583 nmi (4000 ft) [22].

To provide perspective on the ability of all types of UAS to maintain the proposed SST and WC definitions, we sequentially the compute the model for several different ownship speeds. Additionally we explore the sensitivity of key parameters by varying them individually and observing the effect on the maximum SST and WC definitions. The initial scenario uses the parameter values shown in Table 6.1 which are designed to closely match the operational characteristics of current airspace.

Figure 6.5 shows the minimum achievable SST and WC definitions. The red line in each plot represents the nominal value of the definition [22, 23]. The top left plot shows the maximum SST distance definition. As is clear from the figure, the ownship is able to detect intruders far before they cross the distance-based SST. As the speed of the ownship increases, the detection range decreases slightly due to the increased distance necessary to initialize a track. The top right plot shows the value of τ_{DMOD} when the intruders are detected. From this plot it is very clear that the 90 s time-based SST is much too large. For all ownship speeds greater than approximately 35 kts, the maximum achievable time-based SST is less than the nominal SST definition. Thus when the intruders are detected they will already have crossed the time-based SST. The bottom left plot shows the maximum achievable distance-based WC definition. From the plot it is clear that nearly all ownship speeds are able to maintain the nominal WC distance, but ownships moving at 20 kts are unable to maneuver in time. The bottom right plot reinforces this. Ownships moving at 20 kts are unable to maneuver sufficiently to achieve the required horizontal miss distance. Thus the aircraft comes too close in terms of both time and distance.

Overall Figure 6.5 indicates that the current airspace regulations are not suitable for high-density small UAS operations. Small, relatively slow-moving UAS, such as the DJI Phantom 1, are unable to maneuver fast enough to maintain the proposed SST and WC definitions. Furthermore,

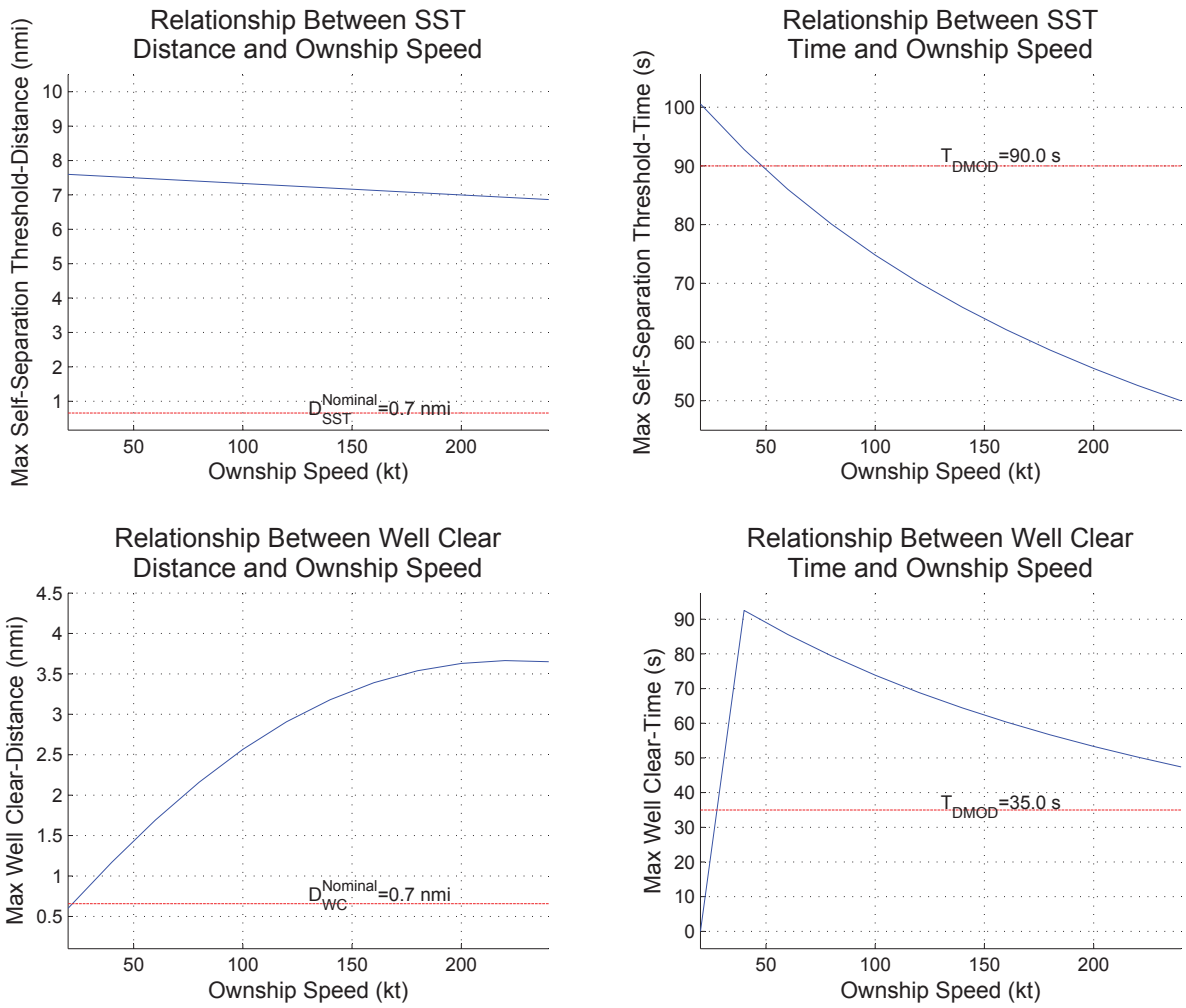

Figure 6.5: Minimum achievable SST and WC definitions for current airspace conditions.

from the top right plot it is clear that the maximum time-based SST that is viable for all ownship speeds is τ_{DMOD} =46 s. For a WC time-based definition that is τ_{DMOD} =35 s, this is very little maneuver time. Interestingly the same high-speed ownships for whom the time-based SST must be lowered to τ_{DMOD} =46 s are able to maintain the τ_{DMOD} =35 s time-based WC definition. Thus the time-based SST definition is too small for the slow UAS and too large for the fast UAS. Changing it would result is an equally unacceptable solution regardless of the direction of change. This shows that the time-based SST definition is not to blame. It is reasonable to deduce that the underlying problem is not the SST and WC definitions, but rather that the airspace regulations and conditions are unsuitable to high-density small UAS operations.

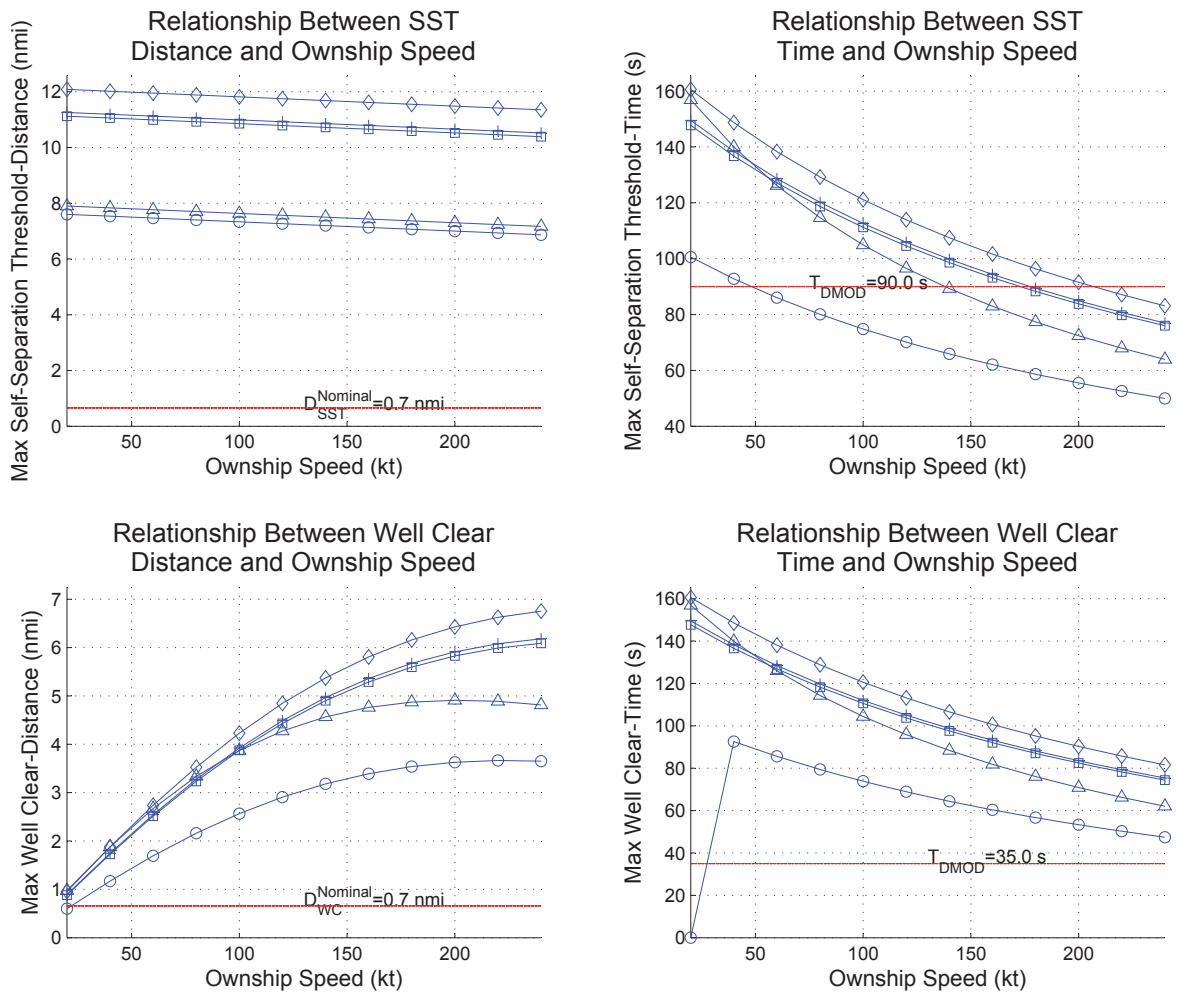

Figure 6.6: Achievable SST and WC definitions as a result of alterations to several airspace conditions and regulations.

Figure 6.6 shows the maximum achievable SST and WC definitions as a result of alterations to airspace conditions and regulations. The track marked by circles shows the base line values from Figure 6.5. All of the other lines indicate that the achievable SST and WC definitions increase significantly. The triangle track shows the results from conditions where the maximum intruder speed is 160 kts rather than the currently regulated 250 kts. The box track explores the possibility of having only 400 aircraft operating at one time rather than the anticipated 800. Thus the UAS density would only be half of what is shown in the base line scenario. The plus sign track illustrates the maximum achievable SST and WC definitions if the bandwidth is doubled by increasing the number of MSOs from 3200 to 6400. Finally, the diamond track shows the results

if the probability of trackability were reduced to be 0.999 rather than 0.999999. While this change would significantly reduce the ability of the DAA system to reliably detect intruders, the maximum achievable SST and WC definitions would also increase significantly.

Ultimately the reduction in the probability of trackability results in the largest increase in the maximum achievable SST and WC definitions, and the reduction of the intruder speed changes the definitions the least. Interestingly, none of the regulations or airspace condition changes results in a maximum time-based SST that is greater than the nominal definition, but all of the changes satisfy the distance-based SST, distance-based WC, and time-based WC definitions.

It is important to note that the results shown in Figure 6.6 are for an ownship that maneuvers as aggressively as possible as soon as the intruder comes into view. Such a demand on the ownship undermines much of the intent behind self-separation. Maintaining well clear is typically understood to imply a gradual change in flight path to ensure a safe distance between aircraft. Demanding that a small UAS turn as sharply as physics will allow from its original path and fly perpendicular to that path as fast as it can is much more indicative of a collision avoidance maneuver. Such maneuvers would seriously interfere with the intended mission of a small UAS, and may, frankly, be intolerable. Additionally it is very unlikely that small, slow-moving UAS will be operating in the same vicinity as manned aircraft that are traveling at 250 kts. In accordance with Google's[1] and Amazon's (`amazon.com/primeair`) published vision for small UAS operation, it is reasonable to expect that small UAS will only encounter relatively slow manned aircraft such as police and medical helicopters. In Amazon's plan they envision a "High-Speed Transit" region that is between 200 ft and 400 ft above ground level. It is in this region where small UAS would encounter manned aircraft. In such a region, very slow moving aircraft such as the DJI Phantom 1, which has a max speed of 20 kts, would not be permitted.

As a result of these expectations, the maximum WC model is adjusted to have a maximum intruder speed of 140 kts and an ownship course change of 40 degrees. Figure 6.7 shows the maximum achievable SST and WC definitions for this scenario. From the figure it is clear that while the slowest UAS are not able to maintain WC, almost all UAS are able to maintain WC from intruders traveling at 140 kts. Furthermore both the distance and time-based SST definitions are achievable. As a result of Figure 6.7, the maximum SST definition for small UAS in congested airspace should

[1] Google Inc., 2015. Google UAS Airspace System Overview.

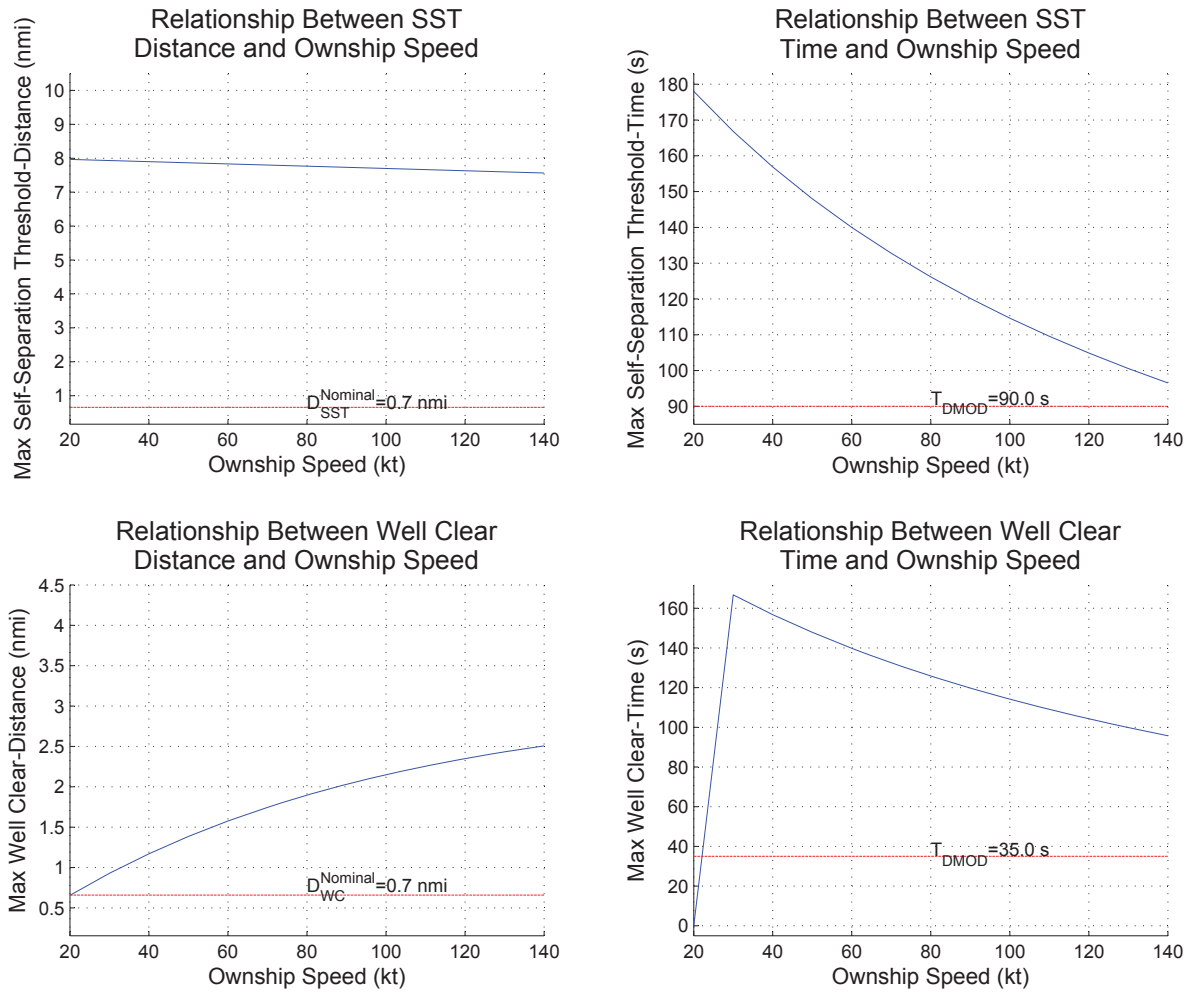

Figure 6.7: Achievable SST and WC definitions as a result of alterations to several airspace conditions and regulations in accordance with Amazon and Google UAS integration vision.

be 7.56 nmi in distance or τ_{DMOD}=96.5 s. The maximum WC definition under the same conditions should be 0.658 nmi of distance and τ_{DMOD}=95.7 s. Thus the definition recommended by SARP is achievable under the proposed low-speed, low-altitude airspace.

6.3.2 Minimum WC Model

The maximum SST and WC definitions provide valuable insight on what is achievable for small UAS. To make a recommendation for WC for small UAS, however, a minimum WC criterion is also necessary. The modified equations for the minimum detection range discussed in

Section 6.2 provide that lower bound. As before the minimum WC definition was calculated for multiple ownship speeds to show the WC definition for a range of ownship types.

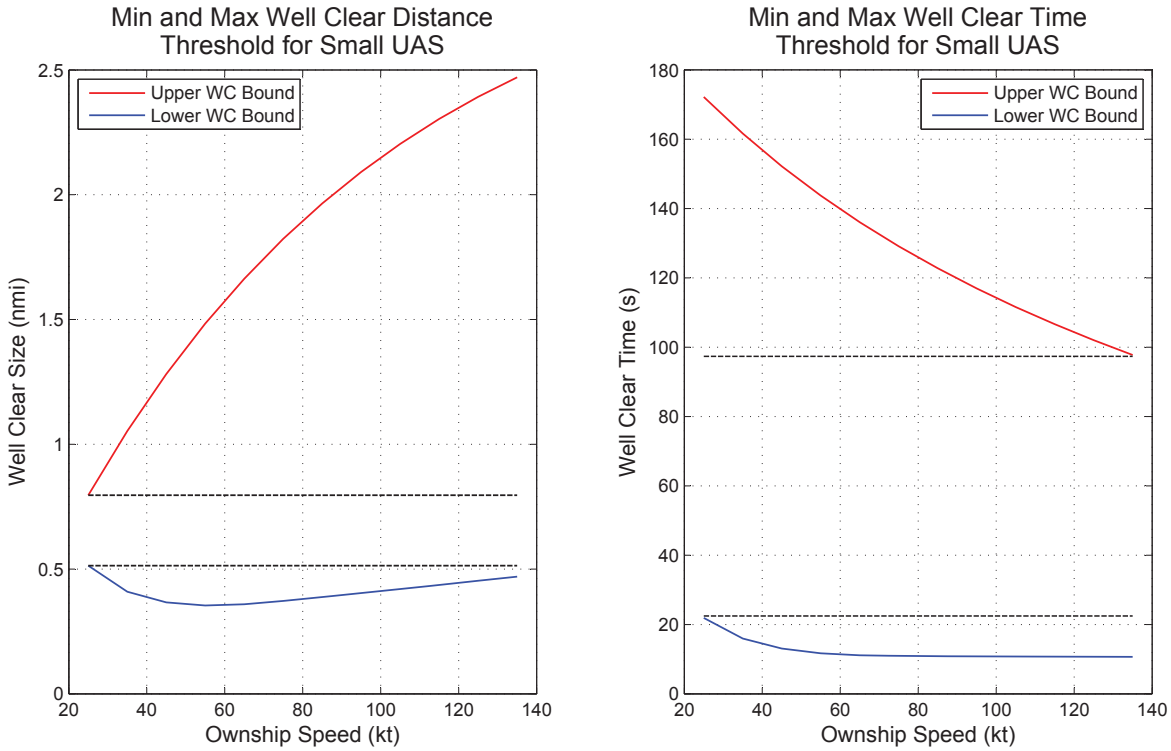

Figure 6.8: Minimum and maximum WC definitions.

Figure 6.8 shows both the upper and lower WC bound as the ownship speed varies. The red lines are the upper bound. Although the upper bound varies at different ownship speeds, the true upper bound is the minimum point on the red line. This ensures that the maximum WC bound is viable for all ownships across the range of speeds. The blue line is the lower bound. In terms of distance the maximum point on the blue line is the true lower bound for all ownship speeds. For time, however, the minimum point on the blue line is the lower WC time bound. The true bounds are shown by the black dotted line.

The figure provides several key insights. First, low speed ownships require the most distance to maneuver. This is because they are moving sufficiently slowly that they are unable to clear the path of the intruder before an NMAC or loss of WC occurs. Secondly, the figure indicates that appropriate WC distance definitions for small UAS in the presence of slow-moving manned

aircraft are on the order of 0.5 nmi (3038 ft). This is larger than anticipated, and it is a valuable anchor point to inform the discussion of WC for small UAS. Third, and most importantly, the combination of an upper and lower WC bound is a basis for recommending a WC definition for small UAS.

On that basis we recommend that the WC definition for small UAS be 0.527 nmi (3200 ft) or τ_{DMOD}=25 s. This definition falls between the boundaries shown in Figure 6.8. As additional data, such as small UAS flight patterns, become available, these bounds and consequently the recommendation can be refined. In the current absence such data, this recommendation is a key step to understanding operationally feasible SST and WC definitions for small UAS.

6.4 ADS-B SST and WC Definition Conclusions

In conclusion, the analysis presented in this chapter determines the maximum and minimum achievable SST and WC definitions in both a distance and time-based context. Furthermore it provides a tool with which SST and WC definitions can be evaluated with respect to their feasibility for future high-density, ADS-B-equipped airspace. Most importantly the recommendation for well clear for small UAS is a key step to integrating small UAS into the national airspace. Overall the approach, methods, and recommendations here are a key contribution to defining well clear and self-separation thresholds for future small UAS-dense airspace.

CHAPTER 7. CONCLUSIONS AND RECOMMENDATIONS

In conclusion, the demand for small UAS is increasing almost daily. First-responders and governmental agencies are turning to small UAS to accomplish tasks faster and more efficiently than ever before. Private companies are planning to deploy small UAS to open new markets and offer services that were previously unavailable. Individual citizens are using UAS to explore and document their surroundings in previously unimaginable ways. Ultimately small UAS are a driving force in revolutionizing all that we formerly knew about aviation, aircraft, and the world around us.

At the heart of this rapid development is a need to maintain the high level of safety that the aviation community has achieved for so many years in the past. Detect-and-avoid systems for UAS are a fundamental piece of such a level of safety. As the FAA 2020 mandate draws nearer, Automatic Dependent Surveillance-Broadcast is gaining more and more attention as a key sensor in DAA systems on both small UAS and manned aircraft. In the excitement surrounding UAS applications, it is important that ADS-B is vetted and understood as a DAA sensor. High-density small UAS operations may stress a DAA systems to its limits. In such an environment, ADS-B transmissions may interfere with each other at an unacceptable level.

7.1 Conclusions

To anticipate the possibility of high-density small UAS operations in the NAS, this thesis provides several key contributions to the understanding of ADS-B as a DAA sensor on small UAS. Chapter 2 provides an error characterization for ADS-B messages. This error characterization can be used to simulate ADS-B messages for testing of DAA systems. It also provides a basis for the development of probabilistic intruder tracking, detection, and conflict/collision avoidance path planning. Chapter 2 also contains a review of ADS-B strengths and weaknesses in the context of DAA on small UAS. Chapter 3 presents a comparison of four different dynamic filters for the

estimation of ADS-B-transmitted measurements. In evaluating a nearly-constant-velocity Kalman filter, constant-jerk Kalman filter, interacting multiple models filter, and particle filter, the results demonstrate that the KF-NCV is the most accurate and efficient filter. Furthermore, the KF-NCV was used to accurately estimate the position of an intruder from recorded ADS-B measurements in the NAS. The estimator comparison and tracking demonstration, show that a KF-NCV is fully capable of overcoming much of the error inherent in ADS-B measurements. Chapter 4 presents a novel long-range, convex optimization-based path planner for a small UAS. This path planner is capable of planning a 15 nmi path in the presence of 10 intruders in 5.5 s in MATLAB. The combination of long-range self-separation assurance planning and computational speed is a significant contribution the the ability of small UAS to maintain well clear. Chapter 5 presents an analysis of the interference limitations of ADS-B. This analysis shows the importance of ADS-B estimation as a method to increase the feasible range of the transmissions. It furthermore demonstrates that transmitting ADS-B messages too far has a negative impact on the overall ability of individual UAS to detect intruder aircraft. The derivation of the probability of interference and the probability of trackability is a novel and significant contribution to ADS-B-based DAA research efforts. Finally, Chapter 6 provides a recommendation for well clear for small UAS in ADS-B congested airspace. It also presents an analysis of the leading self-separation threshold and well clear definitions with respect to ADS-B interference. The methods presented in Chapter 6 also represent a tool with which all SST and WC definitions may be evaluated. The results of the analysis show that changes must be made to NAS regulations before high-density small UAS operations are feasible. Overall these results and contributions are valuable additions toward DAA on small UAS.

7.2 Recommendations

Based on the results presented in this thesis, several key actions can be taken to implement the presented work. First, ADS-B should continue to be pursued as a valuable sensor for DAA on small UAS. That being said, the susceptibility of ADS-B to interference should not be forgotten. ADS-B is a promising sensor based on its long range, low power, omni-directional transmission of a wealth of information. If other sensors become available the offer that same set of characteristics and are less vulnerable to interference, then they should be seriously considered as a replacement to ADS-B. Second, an intruder tracking method, such as the KF-NCV described in this thesis, should

be implemented as a standard, integral part of any ADS-B-based DAA system for either manned or unmanned aircraft. Although at first glance, ADS-B seems to not need estimation methods, the KF-NCV is capable of reducing measurement noise, overcoming measurement dropout, and providing state estimates much faster than the 1 Hz measurement rate. Thus it is an important part of any ADS-B-based DAA system. Third, the convex optimization path planner presented in Chapter 4 is a valuable self-separation algorithm for ADS-B equipped small UAS. It fills a need for computationally efficient, long-range conflict avoidance path planning. It should be tested in a compiled programming language to demonstrate real time operation. Once FAA regulations allow, it should be implemented on an small UAS to test it in a true conflict scenario. Fourth, the work on ADS-B interference should be taken into careful consideration in defining a transmit power regulation for ADS-B on small UAS. Current regulations lead to transmit ranges that are unsustainable for high-density small UAS operations. Thus to properly ensure that small UAS can detect intruders, the presented probability of interference and probability of trackability must be considered. Although not as applicable to small UAS, the work on ADS-B interference should be extended to 1090 MHz and 4G-LTE technology. Both of these protocols have intricate multiple access schemes, and both have likely application to intruder detection for UAS. Fifth, as a result of the presented analysis and well clear recommendation for small UAS, a ”High-Speed Transit” zone should be implemented below 400 ft and above 200 ft. Such a zone would ensure that small UAS would only encounter slow-moving manned aircraft. This would open the door to allow a wide array of UAS applications that are currently not permitted. Additionally the well clear recommendation should be tested in simulation and human-in-the-loop scenarios to verify it. As additional information becomes available the recommendation should be refined. As it stands, however, the proposed well clear recommendation for small UAS fills the pressing need for such a definition. Overall, extending the results achieved through the research presented in this thesis can significantly expand the state of the art. Ultimately, the combination of analyses and developments included in this thesis represent a significant and timely contribution to ADS-B research and larger DAA research efforts to integrate small UAS into the National Airspace System.

REFERENCES

[1] Federal Aviation Administration, 2012. Advisory Circular 90-114: Automatic Dependent Surveillance-Broadcast (ADS-B) Operations. viii, 15

[2] U.S. Department of Transportation, 2013. Unmanned Aircraft System (UAS) Service Demand 2015-2035 Tech. rep., U.S. Air Force. 1

[3] 112th Congress, 2012. FAA Modernization and Reform Act of 2012. 1, 11

[4] Hottman, S., Hansen, K., and Berry, M., 2009. Literature Review on Detect, Sense, and Avoid Technology for Unmanned Aircraft Systems Tech. Rep. September. 1

[5] Federal Aviation Administration, 2015. Subchapter F - Air Traffic and General Operating Rules. 1, 2, 13, 14, 15, 16, 18

[6] George, S., 2009. Concepts of use for UAS Sense and Avoid Equipment Tech. rep. 2

[7] Goshi, D. S., Liu, Y., Mai, K., Bui, L., and Shih, Y., 2009. "Recent advances in 94 GHz FMCW imaging radar development." *IEEE MTT-S International Microwave Symposium Digest*, pp. 77–80. 4

[8] Mackie, J., Spencer, J., and Warnick, K., 2014. "Compact FMCW Radar for GPS-Denied Navigation and Sense and Avoid." In *IEEE Antennas and Propagation Society, AP-S International Symposium*, pp. 989–990. 5

[9] Zaugg, E. C., Hudson, D. L., and Long, D. G., 2006. "The BYU SAR: A Small, Student-Built SAR for UAV Operation." In *International Geoscience and Remote Sensing Symposium (IGARSS)*, pp. 411–414. 5

[10] Moses, A., Rutherford, M. J., and Valavanis, K. P., 2011. "Radar-Based Detection and Identification for Miniature Air Vehicles." In *Proceedings of the IEEE International Conference on Control Applications*, pp. 933–940. 5

[11] Lai, J., Ford, J. J., Mejias, L., Shea, P. O., and Walker, R., 2012. "See and Avoid Using Onboard Computer Vision." In *Sense and Avoid in UAS: Research and Applications*. ch. 10. See an, pp. 265–294. 5

[12] Dey, D., Geyer, C., Singh, S., and Digioia, M., 2009. "Passive , long-range detection of Aircraft : Towards a field deployable Sense and Avoid System." In *Field & Service Robotics*, pp. 1–10. 5

[13] Moody, C., and Strain, R., 2009. "Implementation Consideration for Automatic Dependent Surveillance - Broadcast on Unmanned Aircraft Systems." In *AIAA Infotech@Aerospace Conference*, American Institute of Aeronautics and Astronautics, pp. 1–8. 5, 19

[14] Federal Aviation Administration, 2010. Automatic Dependent Surveillance Broadcast (ADSB) Out Performance Requirements To Support Air Traffic Control (ATC) Service. 6, 11

[15] Klaus, R. A., Mclain, T. W., Beard, R. W., and Colton, M. B., 2013. "Development of a Sense and Avoid System for Small Unmanned Aircraft Systems." PhD thesis, Brigham Young University. 6

[16] Beard, R., and Mclain, T. W., 2012. *Small Unmanned Aircraft: Theory and Practice*. Princeton University Press. 6, 18, 25, 78

[17] Chen, W.-Z., Wong, L., Kay, J., and Raska, V. M., 2009. Autonomous Sense and Avoid (SAA) for Unmanned Air Systems (UAS) Tech. rep. 6

[18] Kochenderfer, M. J., Holland, J. E., and Chryssanthacopoulos, J. P., 2013. "Next-generation airborne collision avoidance system." *Lincoln Laboratory Journal,* **19**(1), pp. 17–33. 6

[19] Foo, J. L., Knutzon, J. S., Oliver, J. H., and Winer, E. H., 2006. "Three-dimensional path planning of unmanned aerial vehicles using particle swarm optimization." In *Mechanical Engineering Conference Presentations, Papers, and Proceedings*, no. September, pp. 1–10. 7

[20] Chen, Y., Han, J., and Zhao, X., 2012. "Three-dimensional path planning for unmanned aerial vehicle based on linear programming." *Robotica,* **30**(05), pp. 773–781. 7

[21] Munoz, C., Narkawicz, A., Chamberlain, J., Consiglio, M., and Upchurch, J., 2014. "A Family of Well-Clear Boundary Models for the Integration of UAS in the NAS." In *14th AIAA Aviation Technology, Integration, and Operations Conference*, pp. 1–16. 8

[22] Johnson, M., Mueller, E. R., and Santiago, C., 2015. "Characteristics of a Well Clear Definition and Alerting Criteria for Encounters between UAS and Manned Aircraft in Class E Airspace." In *11th USA/Europe Air Traffic Management Research and Development Seminar*. 8, 9, 47, 85

[23] Cook, S. P., Brooks, D., Cole, R., Hackenburg, D., and Raska, V., 2015. "Defining Well Clear for Unmanned Aircraft Systems." In *AIAA Infotech@Aerospace*, no. January, pp. 1–20. 8, 20, 47, 84, 85

[24] Upchurch, J., Munoz, C., Narkawicz, A., Chamberlain, J., and Consiglio, M., 2014. Analysis of Well-Clear Boundary Models for the Integration of UAS in the NAS Tech. Rep. June, NASA Langley Research Center, Hampton, VA. 8

[25] Mullins, M., Holman, M., Foerster, K., Kaabouch, N., and Semke, W., 2013. "Dynamic Separation Thresholds for a Small Airborne Sense." In *Guidance, Navigation, and Control*, pp. 1–6. 8

[26] Weibel, R. E., Edwards, M. W. M., and Fernandes, C. S., 2011. "Establishing a Risk-Based Separation Standard for Unmanned Aircraft Self Separation." In *USA/Europe Air Traffic Management Research & Development Seminar*, no. June, pp. 14–17. 8

[27] Cirillo, M., 2005. Air Traffic Bulletin: New Technology - ADS-B, TIS-B, and FIS-B. 11, 16

[28] RTCA, 2009. Minimum Operational Performance Standards for Universal Access Transceiver (UAT) Automatic Dependent Surveillance - Broadcast (ADS-B) DRAFT Final Review and Comment. 13, 14, 15, 16, 18, 59

[29] RTCA, 2011. Minimum Operational Performance Standards for 1090 MHz Extended Squitter Automatic Dependent Surveillance Broadcast (ADS-B) and Traffic Information Services Broadcast (TIS-B). 15, 18

[30] Federal Aviation Administration, 2014. *Aeronautical Information Manual*. 16

[31] Federal Aviation Administration, 2011. Surveillance and Broadcast Services Description Document. 16

[32] Mohleji, S. C., and Wang, G., 2010. Modeling ADS-B Position and Velocity Errors for Airborne Merging and Spacing in Interval Management Application Tech. rep., Center for Advanced Aviation System Development, McLean, VA. 17, 18

[33] Papoulis, A., and Pillai, S. U., 2002. *Probability, Random Variables, and Stochastic Processes*., fourth ed. McGraw-Hill New York. 17, 60

[34] Federal Aviation Administration, 2010. Advisory Circular 20-165: Airworthiness Approval of Automatic Dependent Surveillance - Broadcast (ADS-B) Out Systems. 18

[35] SAE International, 1996. Air Data Computer - Minimum Performance Standard Forward. 18

[36] RTCA, 2003. Minimum Aviation System Performance Standards for Aircraft Surveillance Applications. 18

[37] Lai, C.-p., Ren, Y.-j., and Lin, C., 2009. "ADS-B Based Collision Avoidance Radar for Unmanned Aerial Vehicles." pp. 85–88. 21

[38] Krozel, J., Andrisani, D., Ayoubi, M. A., Hoshizaki, T., Schwalm, C., Conformance, G., Factor, C., Mile, N., Performance, R. N., Radar, S. S., Alert, T., Change, T., Point, T. C., Introduction, I., Scientist, C., Division, D., Researcher, P.-d., and Analyst, S., 2004. "Aircraft ADS-B Data Integrity Check." pp. 1–11. 23

[39] Mehrotra, K., and Mahapatra, P. R., 1997. "A jerk model for tracking highly maneuvering targets." *IEEE Transactions on Aerospace and Electronic Systems,* **33**(4), pp. 1094–1105. 26

[40] Bastos, J., 2008. "An Overview on Target Tracking Using Multiple Model Methods." PhD thesis, Instituto Superior Tecnico. 27

[41] Li, X., and Bar-Shalom, Y., 1993. "Design of an interacting multiple model algorithm for air traffic control tracking." *IEEE Transactions on Control Systems Technology,* **1**(3), pp. 186–194. 28

[42] Arulampalam, M., Maskell, S., Gordon, N., and Clapp, T., 2002. "A tutorial on particle filters for online nonlinear/non-Gaussian\nBayesian tracking." *IEEE Transactions on Signal Processing,* **50**(2), pp. 174–188. 28

[43] Bar-shalom, Y., Daum, F., and Huang, J., 2009. "The Probabilistic Data Association Filter." *IEEE Control Systems Magazine*(December). 30

[44] Boyd, S., and Vandenberghe, L., 2004. *Convex Optimization*. Cambridge University Press, Cambridge, UK. 45

[45] CVX Research, I., 2012. CVX: Matlab software for disciplined convex programming, version 2.0 `http://cvxr.com/cvx`, Aug. 49

[46] Grant, M., and Boyd, S., 2008. "Graph implementations for nonsmooth convex programs." In *Recent Advances in Learning and Control*, V. Blondel, S. Boyd, and H. Kimura, eds., Lecture Notes in Control and Information Sciences. Springer-Verlag Limited, pp. 95–110 `http://stanford.edu/~boyd/graph_dcp.html`. 49

[47] Krozel, J., and Peters, M., 1997. "Strategic conflict detection and resolution for free flight." *Proceedings of the 36th IEEE Conference on Decision and Control,* **2**(December), pp. 1822–1828. 51

[48] Department of Aviation, 2014. Monthly Operations, Passengers, Cargo Summary By Class For December 2014: O'Hare International Airport Tech. Rep. December 2014. 74

[49] Department of Aviation, 2014. Monthly Operations, Passengers, Cargo Summary By Class For December 2014: Midway Airport Tech. Rep. December 2014. 74

[50] Kopardekar, P., 2014. Unmanned Aerial System (UAS) Traffic Management (UTM): Enabling Low-Altitude Airspace and UAS Operations Tech. Rep. April, Ames Research Center, Moffett Field, California. 74